Electromagnetic Transmission Through Resonant Structures

by

Steven M. Young

A dissertation submitted in partial fulfillment
of the requirements for the degree of
Doctor of Philosophy
(Applied Physics)
in the University of Michigan
2016

Doctoral Committee:

Professor Roberto D. Merlin, Chair
Associate Professor Anthony Grbic
Professor L. Jay Guo
Assistant Professor Lu Li
Professor Theodore B. Norris
Associate Professor Kevin Pipe

Byzantine Mosaic Fragment, 5th century A.D. Art Institute of Chicago.

"It is easier for a camel to go through the eye of a needle than for a rich man to enter the kingdom of God."

—Mark 10:25

©Steven M. Young

2016

For Rachel

ACKNOWLEDGMENTS

I could not have finished this work without the help and encouragement of countless others. The acknowledgment and thanks I offer here can only begin to repay my debt to them:

My advisor, Roberto Merlin, is widely admired for his imagination in choosing research problems and his creativity and resoucefulness in solving them. And while these are the traits that drew me to his group, it's his mentorship that I value the most. Roberto pushed me just enough to keep me productive, but also stepped back and gave me room to pursue my own collaborations and research lines (even the dead ends). He shielded me from day to day distractions of administration and funding, but also invited me to help write grants and respond to referees. In short, he let me slowly grow into an independent researcher.

The microwave frequency experiments could not have happened without Professor Tony Grbic, along with his students Carl Pfeiffer, Brian Tierney, and Jason Heebl. They opened their lab, equipment, and engineering expertise to me. Although all of them were busy and productive working on their own research, they never hesitated to help me design experiments, order parts, calibrate equipment, or simply move heavy sheet metal up the stairs. Moreover, their "engineer's" impedance-matching approach to transmission problems proved a useful complement to Roberto's "physicist" perspective, and came to pervade my understanding of resonant transmission.

For their helpful criticism and suggestions, and their willingness to make themselves available despite their unfathomably busy schedules, I thank the other members of my committee: Jay Guo, Lu Li, Ted Norris, and Kevin Pipe.

I owe a significant part of this dissertation to my collaborator and friend Justin Foley, along with his advisor Jamie Phillips. The grating-based filter of Chapter 3 was Justin's project from beginning to end. I was extraordinarily lucky that he invited me to help explain the interesting spectral features in his samples, which led to a fruitful multi-year collaboration. The framework we came up with together, based on the coupling strength and symmetry of resonant guided modes, introduced me to a large part of the literature and influenced my understanding of all my other projects.

I will always value the experiences I shared with with current and past students in the Merlin lab: Meredith Henstridge, Prashant Padmanabhan, Ibrahim Boulares, Alexis

Toulouse, Ben Isaacoff, Jingjing Li, Andrea Bianchini, Ilya Vugmeyster, and Jessica Ames, along with undergraduates Elliot Countess, Greg Affeldt, and Kyle Gordon. Whether actively collaborating, teaching me a lab procedure, kibitzing on our various research problems, arguing about papers, troubleshooting lasers and chillers, or standing ankle-deep in flood water, this group managed to stay positive, friendly, and professional. Meredith in particular collaborated with me on several projects, including the two-slit resonant structure of Chapter 2, which she later extended to THz frequencies; her input and advice have been invaluable.

My experiments required a steady stream of jigs, fixtures, mounts, and gizmos from the LSA student machine shop. Special thanks to the LSA machinists, particularly Julian Broad, Michael Folts, Scott Webster, and Jim Tice, who taught me everything I know about mills and lathes.

For their friendly encouragement and enthusiastic administrative support, I thank the Applied Physics and Physics staff: particularly Cynthia McNabb, Lauren Seagall, Charles Sutton, and Christina Zigulis.

My parents Sharon and Terry provided unwavering and loving support to me and my growing family.

Above all, my wife Rachel was the driving force behind our decision to quit our jobs and head north for our Ph.D. adventure. Even if it didn't always seem so at the time, she was right. I'll always cherish the highs we enjoyed and lows that we weathered together over the past seven years.

My children, Ike and Jay, were absolutely no help at all.

TABLE OF CONTENTS

LIST OF FIGURES

LIST OF TABLES

LIST OF APPENDICES

ABSTRACT

Electromagnetic Transmission Through Resonant Structures

by

Steven M. Young

Chair: Roberto Merlin

Electromagnetic resonators store energy in the form of oscillatory electric and magnetic fields and gradually exchange that energy by coupling with their environment. This coupling process can have profound effects on the transmission and reflection properties of nearby interfaces, with rapid transitions from high transmittance to high reflectance over narrow frequency ranges, and has been exploited to design useful optical components such as spectral filters and dielectric mirrors. Identifying new forms of resonators, and understanding how to engineer the coupling of resonators to their environment, can help make such optical components more compact, simpler to manufacture, more amenable to integration in systems, and feasible in a greater range of frequencies.

This dissertation includes analytic, numeric, and experimental investigations of three different electromagnetic resonators, each based on a different method of confining electromagnetic fields near the region of interest.

First, we show that a structure with two parallel conducting plates, each containing a subwavelength slit, supports a localized resonant mode bound to the slits and therefore exhibits (in the absence of nonradiative losses), perfect resonant transmission over a narrow frequency range. In practice, the transmission is limited by conduction losses in the sidewalls; nevertheless, experimental results at 10 GHz show a narrowband transmission enhancement by a factor of 10^4 compared to the non-resonant transmission, with quality factor (ratio of frequency to peak width) $Q = \omega/\Delta\omega \sim 3000$.

Second, we describe a narrowband transmission filter based on a single-layer dielectric grating. We use a group theory analysis to show that, due to their symmetry, several of

the grating modes cannot couple to light at normal incidence, while several others have extremely large coupling. We then show how selectively breaking the system symmetry using off-normal light incidence can produce transmission peaks by enabling weak coupling to some of the previously protected modes. The narrowband filtering capabilities are validated by an experimental demonstration in the long wavelength infrared, showing transmission peaks of quality factor $Q \sim 100$ within a free-spectral range of 8-15 μm.

Third, we demonstrate that defect-free periodic structures of finite extent can support extended, surface-avoiding, high-quality factor resonant modes, even without mirror-like structures at the boundaries to confine electromagnetic energy. After discussing the necessary conditions for mode confinement to occur, several numerical examples are given. Finally, an experiment at microwave frequencies (2-9 GHz) demonstrates mode confinement, with quality factors $Q \sim 150$, in a 12-period array of short dielectric rods.

CHAPTER 1

Introduction and Background

Harmonic oscillators, or resonators, are well-known to store tremendous oscillatory energy near their natural frequency, a phenomenon familiar to any physics student who has seen footage of the famous Tacoma Narrows Bridge collapse. This dissertation pertains to *electromagnetic* resonators, in which the stored energy takes the form of electric and magnetic fields that are confined near the resonant structure [1]. By definition, resonators gradually exchange energy by coupling with the surrounding environment, and even a very small coupling strength can produce drastic changes in the transmission, reflection, and scattering properties of nearby structures. For instance, a resonator placed across an opaque interface can absorb incident electromagnetic energy from one side and emit it into the other, producing very efficient transmission at a particular frequency (this is the basis for efficient wireless power transfer [2–4]). More generally, the resonant coupling process introduces phase shifts and interference effects that make the transmission and reflection properties of an interface wildly frequency dependent, with implications for the design of useful devices such as spectral filters and dielectric mirrors.

Electrical engineers have long been familiar with the engineering possibilities of resonators. Besides frequency filters based on circuits with lumped capacitors and inductors, resonators have been used to engineer the transmission and reflection spectra of devices at microwave frequencies. To give just two examples, a series of successive cavities in a metal waveguide can form an inductive iris bandpass filter [5], while a periodic metallic mesh can form a frequency selective surface [6].

More recently, advances in microfabrication techniques and computational power have extended such capabilities throughout the electromagnetic spectrum. A striking example was the report by Ebbesen *et al.* [7] of optical transmission through a metallic film perforated by an array of very small holes. Ordinarily, light would be expected to transmit very poorly through such subwavelength holes, but the array's periodicity allowed the incident light to couple resonantly to traveling surface plasmon polaritons, producing extraordinary transmission efficiency greater than unity (when normalized to the area of the holes) near

the plasmon frequency. Ebbesen's report sparked a flurry of renewed attention on tiny holes [8–10] and their interactions with resonances–including both traveling surface waves and localized Fabry-Pérot–type resonances [11]–which has given rise to intriguing optical devices such as structural color filters [12, 13].

Similar recent work has occurred for micro- and nano-scale dielectric structures, with periodic dielectric structures known as photonic crystals [14] attracting increased interest for their potential to engineer a desired electromagnetic response. One example is patterned dielectric surfaces, which can support resonant modes analogous to the plasmonic modes of metallic surfaces and have been used as compact single-layer optical devices ranging from narrowband spectral filters [15] to broadband reflectors [16].

Finally, naturally occurring materials owe their frequency-dependent permittivity and permeability (in the Lorentz model) to microscopic resonances such as lattice vibrations and electronic transitions. Analogously, the ability to fabricate resonant structures much smaller than the wavelength of light has enabled engineering the effective permittivity and permeability of artificial materials [17]. Metamaterials have now been produced with several unique properties, such as negative refractive indices.

The recent work in small metallic holes, patterned dielectric structures, and metamaterials has proceeded somewhat independently, but it is clear by now that all three share the common thread of resonance engineering. Progress will depend, in part, on understanding the effect of resonators on transmission and reflection spectra, on identifying new and potentially useful forms of resonators, and on understanding how to engineer the coupling of resonators to their environment.

1.1 Thesis organization

This dissertation describes analytic, numerical, and experimental studies of three deceptively simple resonant structures: a system of two parallel subwavelength slits, a one-dimensional dielectric grating, and periodic structures of finite extent. In addition to illustrating general resonant transmission and reflection behavior, these structures lend themselves to various potential applications including spectroscopy, *in-situ* material characterization, surveillance, and energy conversion. The dissertation is organized into the following five chapters:

The remainder of Chapter 1 contains a basic review of light transmission through some common optical elements, which can serve as a baseline for comparing the transmission after adding a resonant structure. The effect of adding a resonator to one of these basic interfaces is discussed using a simple intuitive model based on coupled mode theory.

Chapter 2 describes a resonant structure based on two parallel plates, each containing a subwavelength slit [18, 19]. Using approximate analytic calculations, we show that the slits support a localized resonant mode. This allows the structure to exhibit (in the absence of material losses) perfect resonant transmission over a narrow frequency range, an improvement on the order $(\Delta/\lambda)^4$ compared to a single plate with a single slit, where Δ is the slit width and λ is the wavelength. The transmission enhancement occurs for one of the two possible incident polarizations, but not the other. We discuss the effects of material losses using numeric finite-element calculations, and describe an experimental demonstration performed at microwave frequencies (~ 10 GHz).

Chapter 3 describes a narrowband transmission filter with a broad free spectral range based on a single-layer dielectric grating [20, 21]. We numerically calculate the guided modes supported by the grating, then use a group theory analysis to show that, due to their symmetry, several of these modes cannot couple to light at normal incidence, while several others have extremely large coupling. We then show how selectively breaking the system symmetry using off-normal light incidence can enable weak coupling to some of the previously protected modes. The narrowband filtering capabilities are validated using finite element calculations and an experimental demonstration in the long wavelength infrared ($8 - 15$ μm).

Chapter 4 gives demonstrations showing that defect-free periodic structures of finite extent can support extended, surface-avoiding, high-quality factor resonant modes, even without mirror-like structures at the boundaries to confine electromagnetic energy. After discussing the results of a proof given in [22] that this is true regardless of the boundary shape, several numerical examples are given. Finally, the chapter describes an experiment at microwave frequencies (2-9 GHz) demonstrating mode confinement in an array of short dielectric rods. The in-plane confinement is due to the surface-avoiding mode effect, while out-of-plane radiation also appears to be suppressed due to symmetry mismatch with radiative modes.

Finally, Chapter 5 summarizes the results of the previous chapters and discusses potential applications for the various resonators.

1.2 Transmission through common optical elements

When light is incident upon an interface, a portion T of the electromagnetic energy is transmitted across the interface and a portion R is reflected. Conservation of energy requires $T + R + L = 1$, where L represents energy that is neither reflected nor transmitted, whether due to scattering, absorption, or other losses. In this section, we will review the

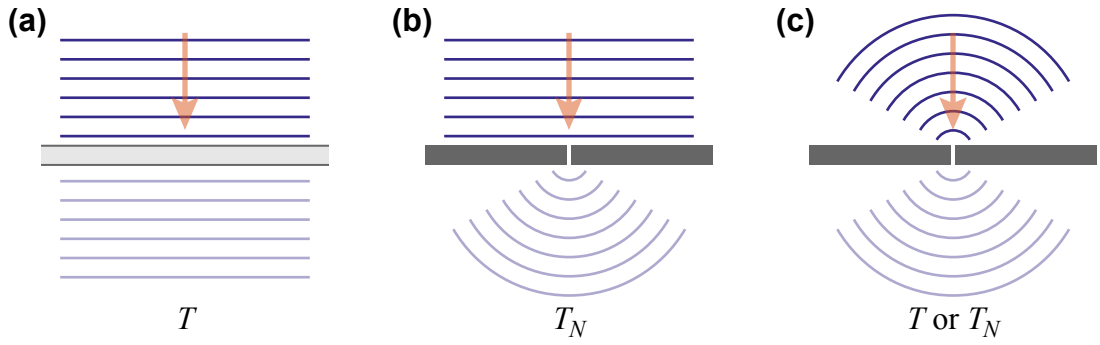

Figure 1.1: Schematics of some transmission scenarios, illustrating when to use the absolute transmission T or area-normalized transmission T_N. (a) Extended incident and transmitted waves, (b) Extended incident wave with localized transmission through an aperture, (c) Focused or confined incident wave with localized transmission through an aperture.

transmission properties of some common and well-studied optical elements, all of which are included in standard texts [1, 23, 24]. This will give a baseline for the following section and subsequent chapters, in which we will discuss the effects of adding resonances. For simplicity, we will consider only lossless, isotropic, linear, non-dispersive materials in these introductory examples, unless noted otherwise.

The transmission T is roughly defined as the power carried by an outgoing transmitted wave (as measured by the time-average Poynting vector), divided by the power carried in the incident wave. However, the precise definition depends on the details of the transmission process, as illustrated by the examples in figure 1.1. In figure 1.1a, both the incident and transmitted waves are plane waves with infinite extent. In this case, comparing the time-averaged power (or power density) on both sides of the slab will give a useful measure of T. Figure 1.1b, on the other hand, shows an incident plane wave diffracting through a small aperture; the total transmitted power is finite, whereas the total incident power is infinite. For such transmission through apertures, previous work (*e.g.*, [7, 9, 25–30]) has commonly used an *area-normalized transmittance* T_N, in which the total transmitted power is compared to the incident power over just the area of the aperture. Note that while T is always less than 1, T_N could be greater than 1 if incident energy is somehow funneled toward the aperture entrance (the term "extraordinary optical transmission" [7] refers to the situation $T_N > 1$). Figure 1.1c shows a case with a focused beam incident upon an small aperture, where either T or T_N could be used. Because the focal size of a beam is limited by the diffraction limit [31] to the order of the wavelength λ, T and T_N are related for a hole of radius a by $T \sim T_N(a/\lambda)^2$. Similarly, for a slit of width Δ, they are related by $T \sim T_N\Delta/\lambda$.

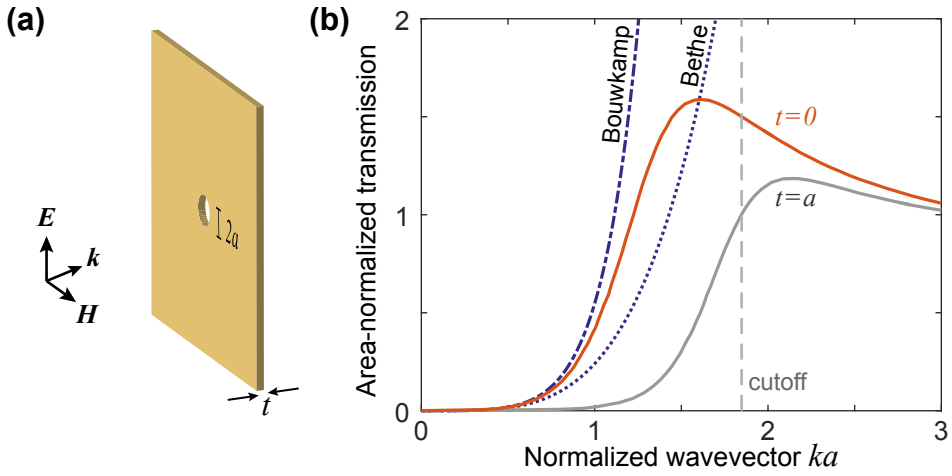

Figure 1.2: (a) Schematic diagram of a circular hole of radius a in a perfectly conducting screen of thickness t and infinite extent, with a normally incident plane wave. (b) Area-normalized transmission T_N through the hole for two different various screen thicknesses, from Roberts. Blue dotted and dashed lines show the small wavenumber predictions of Bethe (eq. 1.1) and Bouwkamp (eq. 1.2), respectively. The cutoff frequency of the circular waveguide, $k_c a = 1.85$, is shown as a vertical dashed line.

1.2.1 Transmission through a subwavelength aperture

The first case we will discuss is the transmission through a small aperture in a conducting screen, figure 1.2a. It has been recognized for nearly two hundred years that electromagnetic fields couple poorly through holes that are small compared to the wavelength (this is after all the basis for Faraday cages). The first accurate transmission calculation, taking into account the vector nature of the electromagnetic fields, was due to Bethe [25], who considered the ideal case of a small circular hole of radius a in an infinitesimally thin, perfectly conducting screen, in the extreme small wavevector limit ($ka \ll 1$) where retardation effects can be ignored. In this limit, the hole can be replaced by electric and magnetic dipoles, yielding a simple expression for the area-normalized transmittance T_N of a normally incident plane wave:

$$T_N = \frac{64}{27\pi^2}(ka)^4 \tag{1.1}$$

Bouwkamp [26, 32], "by a systematic use of complicated integrals," was later able to extend Bethe's result as a series expansion in ka:

$$T_N = \frac{64}{27\pi^2}(ka)^4 \left[1 + \frac{22}{25}(ka)^2 + \frac{7312}{18375}(ka)^4 + \dots\right] \tag{1.2}$$

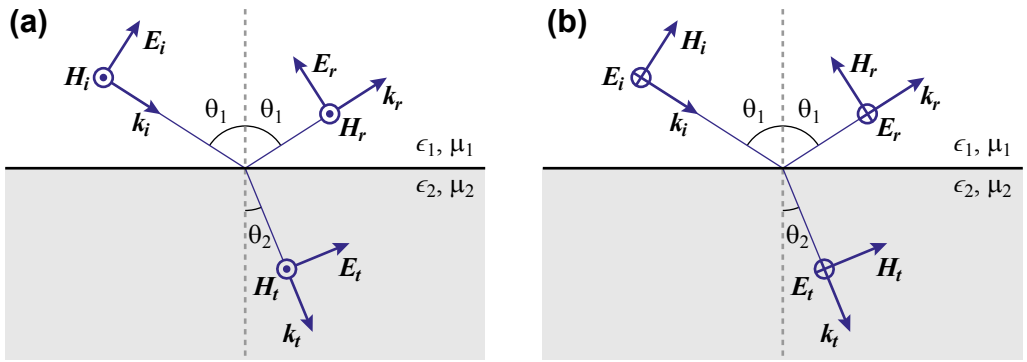

Figure 1.3: Wave and field vectors for incident, reflected, and transmitted plane waves at an interface between two media with two orthogonal polarizations: (a) p polarization, and (b) s polarization. Circles with dots (crosses) indicate vectors pointing out of (into) the plane of the diagram.

While useful for holes much smaller than the wavelength, this expansion evidently fails for smaller wavelengths (it diverges when $ka > 1$). Roberts [33] made a rigorous calculation that could accommodate smaller wavelengths, as well as a possibly thick screen and off-normal incidence, by expanding the fields in the hole as sums over circular waveguide modes. Figure 1.2b shows T_N from ref. [33] for normally incident plane waves with screens of thickness $t = 0$ and $t = a$, as well as the large wavelength predictions from Bethe and Bouwkamp.

In this dissertation, we will only consider a structure with very small apertures relative to the wavelength, $ka < 0.1$, where small wavevector approximations such as Bethe's are perfectly acceptable. For more discussion of the vast body of work on small holes, including the connection to recent work on extraordinary optical transmission, Garcia-Vidal *et al.* [9] give a thorough review.

1.2.2 Transmission across a dielectric interface

Light incident on a smooth interface between two dielectric materials, as depicted in figure 1.3, is both partially reflected and partially refracted into the second material. The incident and reflected angles are related by Snell's law:

$$n_1 \sin\theta_1 = n_2 \sin\theta_2 \tag{1.3}$$

where $n_j = \sqrt{\mu_j \epsilon_j}$ is the refractive index in each region. The field amplitudes are related by the Fresnel coefficients, which depend on the polarization:

$$\text{p polarization} \begin{cases} r_{12} = \left(\dfrac{E_r}{E_i}\right)_p = \dfrac{\eta_1 \cos\theta_1 - \eta_2 \cos\theta_2}{\eta_1 \cos\theta_1 + \eta_2 \cos\theta_2} \\ t_{12} = \left(\dfrac{E_t}{E_i}\right)_p = \dfrac{2\eta_2 \cos\theta_1}{\eta_1 \cos\theta_1 + \eta_2 \cos\theta_2} \end{cases} \tag{1.4a}$$

$$\text{s polarization} \begin{cases} r_{12} = \left(\dfrac{E_r}{E_i}\right)_s = \dfrac{\eta_2 \cos\theta_1 - \eta_1 \cos\theta_2}{\eta_2 \cos\theta_1 + \eta_2 \cos\theta_2} \\ t_{12} = \left(\dfrac{E_t}{E_i}\right)_s = \dfrac{2\eta_2 \cos\theta_1}{\eta_2 \cos\theta_1 + \eta_1 \cos\theta_2} \end{cases} \tag{1.4b}$$

In equation 1.4, η_j is the wave impedance in each region, $\eta = \sqrt{\mu/\epsilon}$. At normal incidence with $\mu_1 = \mu_2$, eq. 1.4 reduces to:

$$r_{12} = \frac{n_1 - n_2}{n_1 + n_2} \qquad \text{and} \qquad t_{12} = \frac{2n_1}{n_1 + n_2} \tag{1.5}$$

The reflectivity R and transmissivity T can then be calculated from the Fresnel coefficients:

$$R = \left|\frac{E_r}{E_i}\right|^2 = |r_{12}|^2 \tag{1.6a}$$

$$T = \frac{\eta_1 \cos\theta_1}{\eta_2 \cos\theta_2}\left|\frac{E_t}{E_i}\right|^2 = \frac{\eta_1 \cos\theta_1}{\eta_2 \cos\theta_2}|t_{12}|^2 \tag{1.6b}$$

At normal incidence with $\mu_1 = \mu_2$, eq. 1.6 reduces to:

$$R = \frac{(n_1 - n_2)^2}{(n_1 + n_2)^2} \qquad \text{and} \qquad T = \frac{4n_1 n_2}{(n_1 + n_2)^2} \tag{1.7}$$

with $R + T = 1$ as required by the conservation of energy.

1.2.3 Transmission through a dielectric slab

The transmission through a thin uniform dielectric slab of thickness d, shown schematically in figure 1.4a, can be expressed in terms of the single-interface reflection (transmission) coefficients r_{12} and r_{23} (t_{12} and t_{23}), from eq. 1.4. Airy's method of summing the contributions from multiple partial reflections [34] or (equivalently) transfer matrix methods [23]

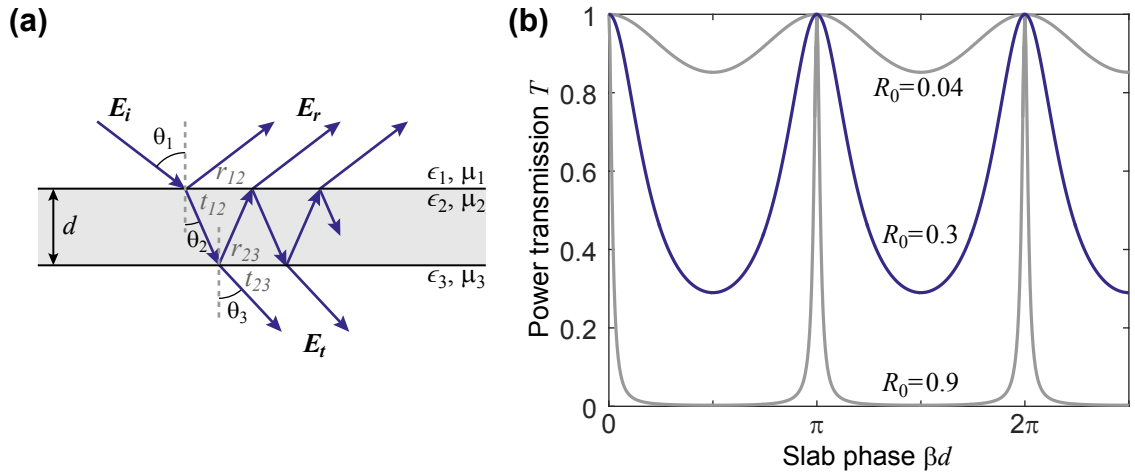

Figure 1.4: (a) Multiple reflection picture for the transmission through a dielectric slab. (b) Power transmission spectra of a symmetric dielectric slab ($\epsilon_1 = \epsilon_3$) for various values of the single interface reflectivity R_0. The highlighted spectrum with $R_0 = 0.3$ corresponds to the infrared reflectivity of silicon ($\epsilon_2 = 11.7$) in air at normal incidence.

give the overall reflection and transmission coefficients for the slab:

$$r = \frac{E_r}{E_i} = \frac{r_{12} + r_{23}e^{i2\beta d}}{1 + r_{12}r_{23}e^{i2\beta d}} \tag{1.8a}$$

$$R = |r|^2 = \frac{r_{12}^2 + r_{23}^2 + 2r_{12}r_{23}\cos(2\beta d)}{1 + r_{12}^2 r_{23}^2 + \cos(2\beta d)} \tag{1.8b}$$

$$t = \frac{E_t}{E_i} = \frac{t_{12}t_{23}e^{i\beta d}}{1 + r_{12}r_{23}e^{i2\beta d}} \tag{1.9a}$$

$$T = \frac{\eta_1 \cos\theta_1}{\eta_3 \cos\theta_3}|t|^2 = \frac{\eta_1 \cos\theta_1}{\eta_3 \cos\theta_3}\left(\frac{t_{12}^2 t_{23}^2}{1 + r_{12}^2 r_{23}^2 + \cos(2\beta d)}\right) \tag{1.9b}$$

In equations 1.8 and 1.9, β is the wavevector component within the slab that is normal to the interfaces,

$$\beta = \frac{n_2\omega}{c}\cos\theta_2 \tag{1.10}$$

Thus, βd represents the phase accumulated by a wave traversing the slab, and $2\beta d$ is the phase accumulated in a round trip. As required by the conservation of energy, $R + T = 1$.

The above expressions can be simplified considerably if the slab is symmetric, so that the input and output half-spaces have the same material properties. In that case, $r_{23} = -r_{12}$, and $t_{12}t_{23} = 1 - r_{12}^2 = 1 - R_0$, where R_0 is the single-interface reflectivity. Substituting

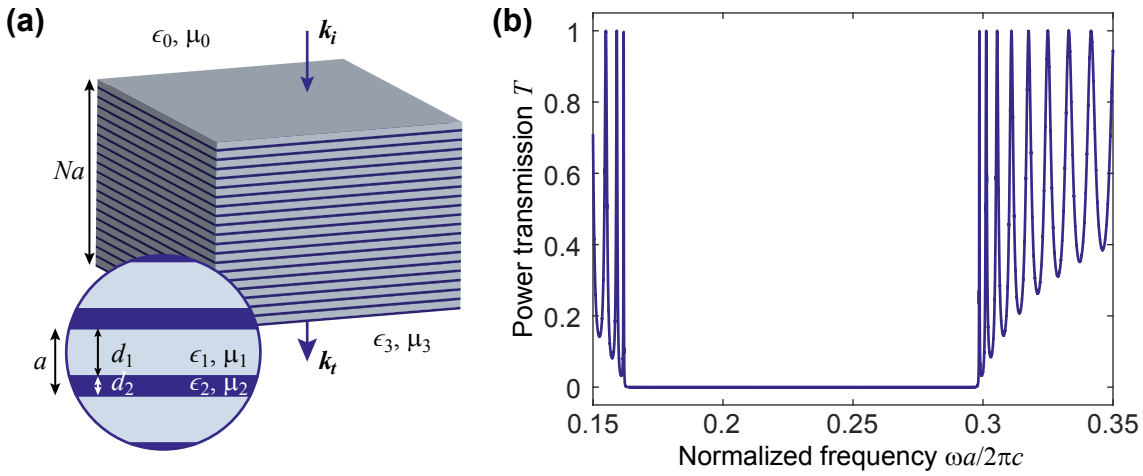

Figure 1.5: (a) Schematic diagram of a multilayer stack comprising N identical dielectric bilayers of thickness $d_1 + d_2 = a$. (b) Transmission at normal incidence through a Si/SiO_2 stack surrounded by air with $N = 20$, $n_1 = 1.5$, $n_2 = 3.9$, $d_1 = 0.72a$, and $d_2 = 0.28a$.

into 1.8 and 1.9 yields:

$$r = \frac{E_r}{E_i} = \frac{r(1 - e^{i2\beta d})}{1 - r^2 e^{i2\beta d}} \tag{1.11a}$$

$$R = |r|^2 = \frac{4R_0 \sin^2(\beta d)}{(1 - R_0)^2 + 4R_0 \sin^2(\beta d)} \tag{1.11b}$$

$$t = \frac{E_t}{E_i} = \frac{(1 - r^2)e^{i\beta d}}{1 - r^2 e^{i2\beta d}} \tag{1.12a}$$

$$T = |t|^2 = \frac{(1 - R_0)^2}{(1 - R_0)^2 + 4R_0 \sin^2(\beta d)} \tag{1.12b}$$

Figure 1.4b plots the transmission from eq. 1.12b as a function of βd for several values of the single-interface reflectivity R. 100% transmission occurs at the Fabry-Pérot resonance condition $\beta d = m\pi$, with $m = 0, 1, 2, \ldots$.

1.2.4 Transmission through multiple dielectric layers

The same techniques used for a single dielectric layer can be extended to analyze the transmission through a multilayer dielectric stack, such as in figure 1.5. The fields at the entrance

and exit planes of the stack are related by a transfer matrix,

$$\begin{pmatrix} E_0 \\ H_0 \end{pmatrix} = \boldsymbol{W} \begin{pmatrix} E_N \\ H_N \end{pmatrix} \tag{1.13}$$

where the transfer matrix $\boldsymbol{W}$ depends on the thicknesses and material properties of the layers in the stack. For a periodic stack comprising N identical bilayers of two contrasting materials, $\boldsymbol{W}$ is given by:

$$\boldsymbol{W} = \left[\begin{pmatrix} \cos\beta_1 d_1 & -i\eta_1 \sin\beta_1 d_1 \\ -i\eta_1^{-1}\sin\beta_1 d_1 & \cos\beta_1 d_1 \end{pmatrix} \begin{pmatrix} \cos\beta_2 d_2 & -i\eta_2 \sin\beta_2 d_2 \\ -i\eta_2^{-1}\sin\beta_2 d_2 & \cos\beta_2 d_2 \end{pmatrix} \right]^N \tag{1.14}$$

In equation 1.14, $\beta_1 d_1$ and $\beta_2 d_2$ are the phases accumulated by waves traveling in each subregion of the bilayer (see eq. 1.10), while η_1 and η_2 are the wave impedances.

Noting that the fields at $z = 0$ are given by a superposition of forward and backward propagating waves, $E_0 = E_i + E_r$, whereas there is no backward propagating wave at the exit, $E_N = E_t$, we set $E_i = 1$, $E_r = r$, and $E_N = t$. Substituting into eq. 1.13 gives a set of two equations for the complex reflection and transmission coefficients:

$$\begin{pmatrix} 1+r \\ (1-r)\eta_0^{-1} \end{pmatrix} = \boldsymbol{W} \begin{pmatrix} t \\ t\eta_3^{-1} \end{pmatrix} \tag{1.15}$$

If the alternating layers are designed such that $\beta_1 d_1 = \beta_2 d_2 = \pi/2, 3\pi/2, \ldots$, then the structure is a quarter-wave stack, or distributed Bragg reflector. Within each layer at the design frequency, the forward propagating waves destructively interfere with each other, while the backward propagating waves constructively interfere, producing a frequency selective, high-reflectance structure. Figure 1.5 shows the transmission spectrum in air for such a multilayer dielectric stack comprising $N = 20$ periods of length a with $d_1 = 0.72a$ and $d_2 = 0.28a$, and refractive indices $n_1 = 1.5$ and $n_2 = 3.9$. The spectrum clearly shows the wide band of high reflection emblematic of distributed Bragg reflectors, widely used in laser and other cavity applications [35–37] as the mirrors in a Fabry-Pérot etalon.

The distributed Bragg reflector is a simple one dimensional example of a photonic crystal [14]; a structure with periodicity of the same order as the wavelength. Such structures have been shown to possess optical band structures, analogous to the electronic bands of crystalline materials [38, 39]. The optical band structure provides an alternate interpretation of the Bragg reflector's characteristic transmission spectrum, with the wide reflection bands corresponding to band gaps where light propagation is forbidden. Besides the obvious utility of the reflection band, the high transmission peaks above the forbidden band

edge of $\omega_G a/2\pi c \simeq 0.3$ are also of interest. As discussed in Chapter 4, these transmission peaks are actually associated with resonant surface avoiding modes that always arise near the band edges in finite periodic structures [22].

1.3 Resonant transmission

Now we will consider the effects of coupling a resonator to an interface. Without the resonator present, incident energy is reflected or transmitted via the interface's direct scattering pathway, described by the r and t coefficients. The resonator provides a second, indirect pathway in which energy is first coupled into the resonator and then later emitted, with a phase shift, into the outgoing waves. By interfering with the direct-scattered waves, the emitted waves from the resonator can either enhance the overall transmission (constructive interference) or suppress it (destructive interference), depending on the phase shift. And since the phase shift introduced by a resonator can be highly frequency-dependent, the spectral response of a resonant interface varies between high transmission and high reflection over narrow frequency ranges.

The distinctive spectral response produced by interference between multiple resonant pathways is quite general and has been observed in numerous physical systems. It is often referred to as a Fano lineshape [40], after a researcher who studied it in atomic and condensed matter systems. First observed as the Wood anomaly in metallic gratings [41], which was eventually explained as interference with a resonant leaky mode supported by the grating [42], Fano lineshapes have also been observed in association with many other resonant phenomena, including guided modes in dielectric gratings and photonic crystal slabs [15,43], surface plasmon polaritons in metallic films [7], Fabry-Pérot type resonances in small slits [11, 44], and infrared optical phonons [45]. The common feature in these systems is the presence of two interfering resonant pathways, one of which has a broad frequency response and provides a slowly-varying background, and the other of which has a narrow frequency response and produces a rapidly-varying lineshape.

In this section we will discuss a simple and intuitive model based on temporal coupled mode theory [46–48] that can quantitatively explain the frequency-dependent transmission behavior of resonant interfaces. In coupled mode theory, the incoming and outgoing radiative fields and the fields associated the resonance are treated as separate objects that couple to each other via their spatial overlaps. This approximation is valid provided the coupling with the resonance is small; that is, when the resonance width is small compared to the frequency. The notation in the following discussion is adapted from refs. [47, 48].

To begin, consider the slab shown in figure 1.6, with sets of incoming waves s_{j+} and as-

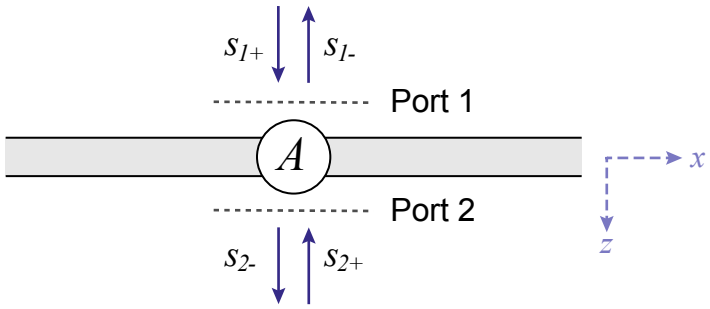

Figure 1.6: Coupled mode model for an interface with an embedded resonance coupled to two radiative modes.

sociated outgoing waves s_{j-}. The wave amplitudes are normalized so that $|s_{j+}|^2$ and $|s_{j-}|^2$ are the electromagnetic power carried by the waves. We will consider just one set of waves on either side of the slab, which can correctly describe the fields if the form of the waves is chosen judiciously–*e.g.*, plane waves for a subwavelength grating structure, focused beams for an aperture in a metallic screen, etc. (Alternatively, a large set of orthogonal basis waves could be used on either side and superimposed to give the correct fields). For simplicity, we will consider a system that is symmetric with respect to reflection across the xy plane ($\widehat{\sigma}_z$ symmetry), so that the direct non-resonant scattering process can be described by:

$$\begin{pmatrix} s_{1-} \\ s_{2-} \end{pmatrix} = \begin{pmatrix} r_s & t_s \\ t_s & r_s \end{pmatrix} \begin{pmatrix} s_{1+} \\ s_{2+} \end{pmatrix} \tag{1.16}$$

where r_s and t_s are suitable reflection and transmission coefficients for the slab with homogenized material properties.

In the following sections, we will consider the effects of adding one or more resonances to the structure.

1.3.1 One added resonance

Consider the situation in figure 1.6 where the slab supports a single resonance A, with amplitude normalized so that $|A|^2$ is the electromagnetic energy in the resonator. The resonance couples radiatively into the two outgoing waves s_{1-} and s_{2-} with coupling constants d_1 and d_2, respectively, giving an overall radiative decay rate of τ_r. In addition, a nonradiative decay rate τ_{nr} heuristically accounts for energy dissipation into modes other than s_{1-} and s_{2-}, including impurity or disorder scattering, material absorption, and inhomogeneous broadening. The incoming waves s_{1+} and s_{2+} scatter into the outgoing waves via the direct pathway in eq. 1.16, and also couple energy into the resonance with coupling

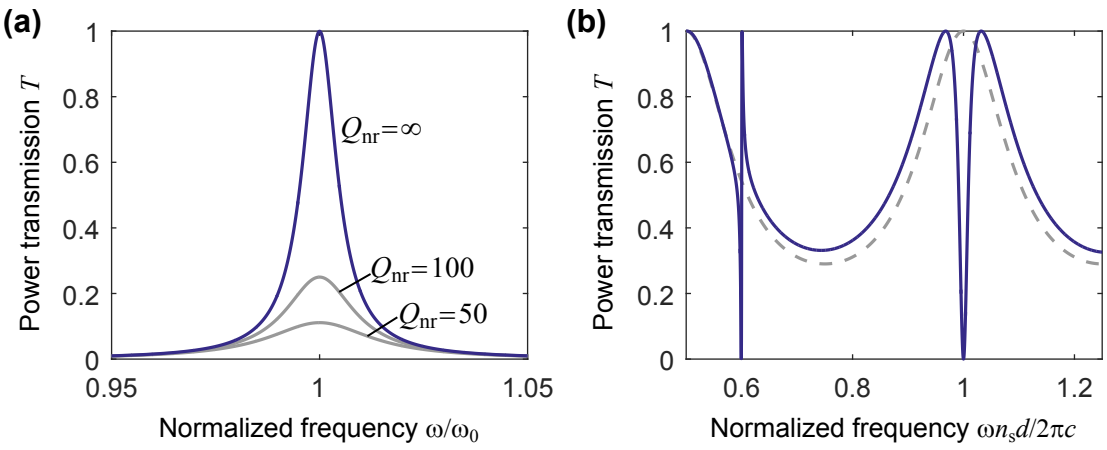

Figure 1.7: (a) Transmission in the coupled-mode model through a small aperture ($t_s \simeq 0$, $r_s \simeq 1$) coupled to a resonance with frequency ω_0 and quality factor $Q_r = 100$, for various values of the non-radiative quality factor Q_{nr}. (b) Transmission in the coupled-mode model through a dielectric slab with $n_s = 3.4$ at normal incidence, with two independent resonances of opposite parity, $\omega_A n_s d/2\pi c = 0.6$, $Q_{rA} = 400$, $\omega_B n_s d/2\pi c = 1$, $Q_{rB} = 50$. The dashed gray line shows the transmission through the slab without added resonances.

constants κ_1 and κ_2. This system is described by the following system of equations:

$$\frac{\mathrm{d}A}{\mathrm{d}t} = \left(-i\omega_A - \frac{1}{\tau_r} - \frac{1}{\tau_{nr}}\right) A + \kappa_1 s_{1+} + \kappa_2 s_{2+} \tag{1.17a}$$

$$s_{1-} = r_s s_{1+} + t_s s_{2+} + d_1 A \tag{1.17b}$$

$$s_{2-} = t_s s_{1+} + r_s s_{2+} + d_2 A \tag{1.17c}$$

Setting $s_{2+} = 0$ and looking for harmonic solutions with $e^{-i\omega t}$ time dependence gives the overall transmission coefficient including resonant effects:

$$t = \frac{s_{2-}}{s_{2+}} = t_s + \frac{d_2 \kappa_1}{\tau_r^{-1} + \tau_{nr}^{-1} - i(\omega - \omega_A)} \tag{1.18}$$

and the power transmission is then $T = |t|^2$. Conservation of energy and time-reversal symmetry put constraints on the relationships between r_s, t_s, τ_r, $\kappa_{1(2)}$, and $d_{1(2)}$ [47]. Using these principles, along with the $\widehat{\sigma}_z$ symmetry of the system, allows us to simplify eq. 1.18 significantly, as follows [48]. First, the reflection symmetry requires that the resonant fields are either even or odd with respect to $\widehat{\sigma}_z$, so:

$$d_2 = \pm d_1 \tag{1.19}$$

where the upper sign is associated with an even resonant mode, and the lower sign with an odd mode. Second, the conservation of energy requires that when the incoming waves s_{1+} and s_{2+} are set to zero, the energy dissipated radiatively from A is carried in the outgoing waves s_{1+} and s_{2+}. That is,

$$\begin{aligned} |d_1|^2 + |d_2|^2 &= 2\tau_r^{-1} \\ |d_1|^2 &= \tau_r^{-1} \end{aligned} \tag{1.20}$$

Third, as shown in ref. [47], time-reversal symmetry and $\widehat{\sigma}_z$ symmetry together require that

$$r_s d_1^* + t_s d_2^* + d_1 = 0 \tag{1.21}$$

and, finally, these symmetries along with the conservation of energy give

$$d_1 = \kappa_2 \quad , \quad d_1 = \kappa_2 \tag{1.22}$$

Using eqs. 1.19, 1.20, and 1.21 together give:

$$\begin{aligned} r_s|d_1|^2 \pm t_s|d_1|^2 + d_1^2 =& 0 \\ d_1^2 =& -\tau_r^2(r_s \pm t_s) \end{aligned} \tag{1.23}$$

Substituting these results into eq. 1.18 gives a simplified expression for the transmission through a symmetric interface supporting a resonance:

$$\begin{aligned} t =& t_s \mp \frac{\tau_r^{-1}(r_s \pm t_s)}{\tau_r^{-1} + \tau_{nr}^{-1} - i(\omega - \omega_A)} \\ =& t_s \mp \frac{Q_r^{-1}(r_s \pm t_s)}{Q_r^{-1} + Q_{nr}^{-1} + 2i(1 - \omega/\omega_A)} \end{aligned} \tag{1.24}$$

where $Q_r = \omega_A \tau_r/2$ and $Q_{nr} = \omega_A \tau_{nr}/2$ are the radiative and nonradiative quality factors, respectively.

Figure 1.7 plots the transmission calculated using eq. 1.24 for some symmetric interfaces with various values of the direct scattering coefficients r_s and t_s. When the nonresonant interface is completely opaque, with $|r_s| = 1$ and $t_s = 0$, then the resonance produces a Lorentzian transmission peak with width given by $Q^{-1} = \delta\omega/\omega = Q_r^{-1} + Q_{nr}^{-1}$ and amplitude proportional to $[Q_r^{-1}/(Q_r^{-1} + Q_{nr}^{-1})]^2$. In the absence of losses ($Q_{nr} \to \infty$), the resonant transmission is perfect. On the other hand, as the resonance becomes decoupled from the continuum, $Q_r \to \infty$, it becomes a bound state and the peak disappears if there

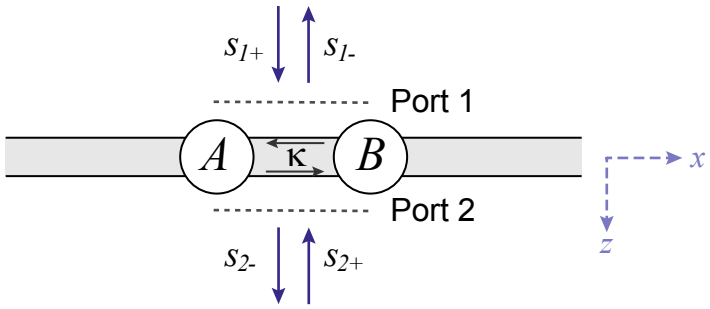

Figure 1.8: Coupled mode model for an interface with two radiative modes and two resonant modes coupled by κ.

are any losses.

Similarly, a completely transparent interface, with $|t_s| = 1$ and $r_s = 0$, will produce a Lorentzian reflection peak, as noted in [15]. For any other combination of r_s and t_s, the resonance produces an asymmetric Fano lineshape, with a rapid transition between perfect reflection and perfect transmission near the resonant frequency.

1.3.2 Multiple resonances

Adding an additional resonance B as shown in figure 1.8 results in the following set of equations:

$$\frac{\mathrm{d}A}{\mathrm{d}t} = \left(-i\omega_A - \frac{1}{\tau_{rA}} - \frac{1}{\tau_{nrA}} - \kappa\right) A + d_{1A}s_{1+} + d_{2A}s_{2+} + \kappa B \tag{1.25a}$$

$$\frac{\mathrm{d}B}{\mathrm{d}t} = \left(-i\omega_B - \frac{1}{\tau_{rB}} - \frac{1}{\tau_{nrB}} - \kappa\right) B + d_{1B}s_{1+} + d_{2B}s_{2+} + \kappa A \tag{1.25b}$$

$$s_{1-} = r_s s_{1+} + t_s s_{2+} + d_{1A}A + d_{1B}B \tag{1.25c}$$

$$s_{2-} = t_s s_{1+} + r_s s_{2+} + d_{2A}A + d_{2B}B \tag{1.25d}$$

The coupling constant κ between modes A and B is in general complex. In a mechanical analog of the model, the real part of κ represents dissipative (dashpot) coupling, while the imaginary part corresponds to spring coupling. As shown by Barker and Hopfield in the particular case of coupled phonons [45], there are many equivalent choices for κ, ω_A, and ω_B, with pure spring-coupling and pure dashpot-coupling forms related by a diagonalization procedure. In any case, the various parameters in eq. 1.25 can be obtained by fitting, although they are constrained by energy conservation and time-reversal symmetry considerations, as in the one-resonance case.

One simple case is when the A and B modes have opposite parity with respect to re-

flections about the xy plane ($\widehat{\sigma}_z$). In that case, $\kappa = 0$ and the modes are independent. The transmission is then simply:

$$t = t_s \mp \frac{Q_{rA}^{-1}(r_s \pm t_s)}{Q_{rA}^{-1} + Q_{nrA}^{-1} + 2i(1-\omega/\omega_A)} \pm \frac{Q_{rB}^{-1}(r_s \mp t_s)}{Q_{rB}^{-1} + Q_{nrB}^{-1} + 2i(1-\omega/\omega_B)} \tag{1.26}$$

Figure 1.7b shows an example transmission spectrum with two such independent modes, calculated using eq. 1.26.

Arranging to have multiple overlapping resonances is one route to achieving a narrow-band transmission filter using transparent dielectric materials. For the transmission filter, it is desirable to have a narrow transmission peak surrounded by a wide free spectral range of low transmission. A dielectric transmission filter therefore requires the incident light to interact with two resonances of similar frequency and different coupling strength: the strongly coupled mode produces a broad reflectance resonance, and Fano interference with the weakly coupled mode produces a narrow transmission peak within this high reflectance background [20, 21, 49–52]. One such filter is discussed in Chapter 3.

CHAPTER 2

Transmission Through Parallel Subwavelength Slits

2.1 Introduction

[1] In a sense, a conducting surface with a very small hole in it is the classic "nearly-opaque" system. From aperture theory [25,26], electromagnetic radiation generally transmits poorly through holes of dimension a much smaller than the wavelength λ, with the ratio of transmitted power to the power incident upon the holes scaling as $(a/\lambda)^4$. However, more recent work has shown that transmission can increase dramatically if the apertures are coupled to a resonant structure. Such extraordinary transmission has been reported both for arrays of apertures coupled by surface plasmon-polaritons [7, 9, 11, 53, 54] and for single apertures, such as a narrow slit in a thick conductor exhibiting Fabry-Pérot–like resonance [27, 30], a slotted metallic cavity [28], a hole surrounded by a corrugated surface [55, 56], and others [57–59]. Resonant cavities in particular have long been used in microwave transmission filters [5]. García-Vidal *et al.* [9] provide a review of work in extraordinary transmission and its applications including sensing, near-field microscopy and light harvesting.

In this chapter, we will examine a particularly simple structure exhibiting resonant transmission, namely a pair of parallel conducting walls, each of which has a single subwavelength slit. We'll show that the presence of the pair of slits leads to the occurrence of a bound resonance, and thereby, to perfect transmission, even though the underlying (slitless) structure does not support strictly localized resonances. Figure 2.1 shows the two-slit structure, which consists of two parallel conducting plates separated by a distance d and extending infinitely in the $\hat{x}$ and $\hat{y}$ directions. Two parallel, narrow slits of width $2\Delta_1$ and $2\Delta_2$, respectively, extend infinitely in the $\hat{y}$ direction. Note that, in the absence of the slits,

[1] Portions of this chapter were originally published in [19] (©2013 AIP Publishing LLC). Reused here with permission.

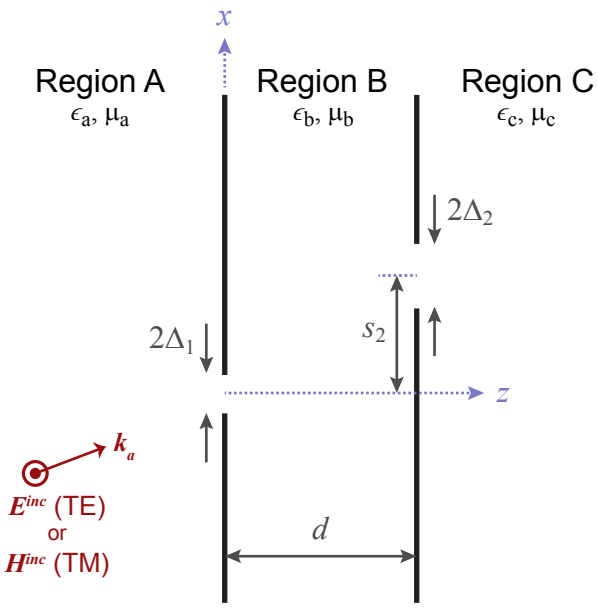

Figure 2.1: Schematic of the two-slit structure. The conducting walls extend infinitely in the $\hat{x}$ and $\hat{y}$ directions.

Region B does not support a localized mode, as there are no walls confining the field in the $\pm\hat{x}$ directions.

We are interested in the electromagnetic power carried by waves incident from region A, through both slits, into region C. We will consider waves that are cylindrically focused or otherwise confined near the first slit, so that the transmission T can be simply defined as the power transmitted into region C, divided by the total power in the incident beam. Note that this measure of transmission differs from the *area-normalized transmittance* T_N commonly used in previous work on extraordinary transmission [7, 9, 27–30] when dealing with extended incident waves, such as plane waves. When the incident beam is cylindrically focused near the diffraction limit, the two measures are related by $T \sim T_N \Delta/\lambda$. The case $T = 1$ (or 0 dB) is called *perfect transmission*.

We will study and contrast two polarizations for the incident waves. Previous work on similar structures has primarily considered the transverse magnetic (TM) case, with the magnetic field in the plane of the walls and parallel to the slits [29, 60–62] (note that this polarization is sometimes called TE in the earlier engineering literature). When the incident beam is TM polarized, enhanced transmission occurs at the Fabry-Pérot–like resonance condition $d = m\lambda/2$, $(m = 1, 2, ...)$. However, the resonant transmission is not perfect, in part because power can be carried away from the slits via waveguide modes that propagate between the conducting plates in the $\pm\hat{x}$ directions. In the less-studied transverse

electric (TE) case, with the electric field parallel to the slits, the structure supports long-lived resonant states localized near the slits at frequencies slightly below the Fabry-Pérot frequencies [18]. The presence of these slit-bound modes, together with the poor coupling of TE radiation through the narrow slits, produces sharp resonant peaks in transmission through the pair of slits. In the limits of narrow slits and perfectly conducting plates, the resonant transmission is perfect ($T = 1$).

2.2 Analytic Transmission Calculation Using the Equivalence Principle

Although the fields and transmission for the two-slit structure of figure 2.1 can be readily found using numeric techniques such as the finite element method, we can gain some insight and physical intuition by finding an approximate analytic solution. In particular, we'll consider the case where the slotted sheets are infinitesimally thin perfect electrical conductors (PEC), with slit widths that are small compared to the wavelength ($k\Delta \ll 1$). Leviatan [29] previously solved this problem with incident TM fields (magnetic field parallel to the slits), and Merlin [18] gave a TE solution in the case with aligned slits ($s_2 = 0$) of equal width ($\Delta_1 = \Delta_2$) and uniform material properties ($\epsilon_a = \epsilon_b = \epsilon_c$). Here, we'll extend the earlier work by giving approximate analytic solutions for both the TE and TM cases, with possibly unequal slits and material properties. The results will be compared to the non-resonant transmission through a single slit.

The equation to be solved is the 2d scalar Helmholtz equation,

$$\left(\frac{\partial^2}{\partial x^2} + \frac{\partial^2}{\partial z^2} + k_i^2\right)\Phi = 0 \tag{2.1}$$

where $k_i = \omega\sqrt{\mu_i\epsilon_i}$ is the free space wavevector in each region. For the TE case, Φ represents the electric field component parallel to the slits, subject to the boundary condition $\Phi = 0$ at the PEC walls. For the TM case, Φ represents the magnetic field parallel to the slits and has the Neumann boundary condition $\partial\Phi/\partial n = 0$ at the walls. Eq. 2.1 can be solved piecewise in each region, with the condition that the tangential electric and magnetic fields are continuous across each slit boundary.

We will use an approach based on the equivalence principle [63] that recasts the problem as a generalized circuit network [64]. A similar approach has been used to analyze transmission through narrow slots in a thick conductor [27], transmission through apertures in a cavity [28], and the TM case of this two slit problem [29], among others [57, 65]. The

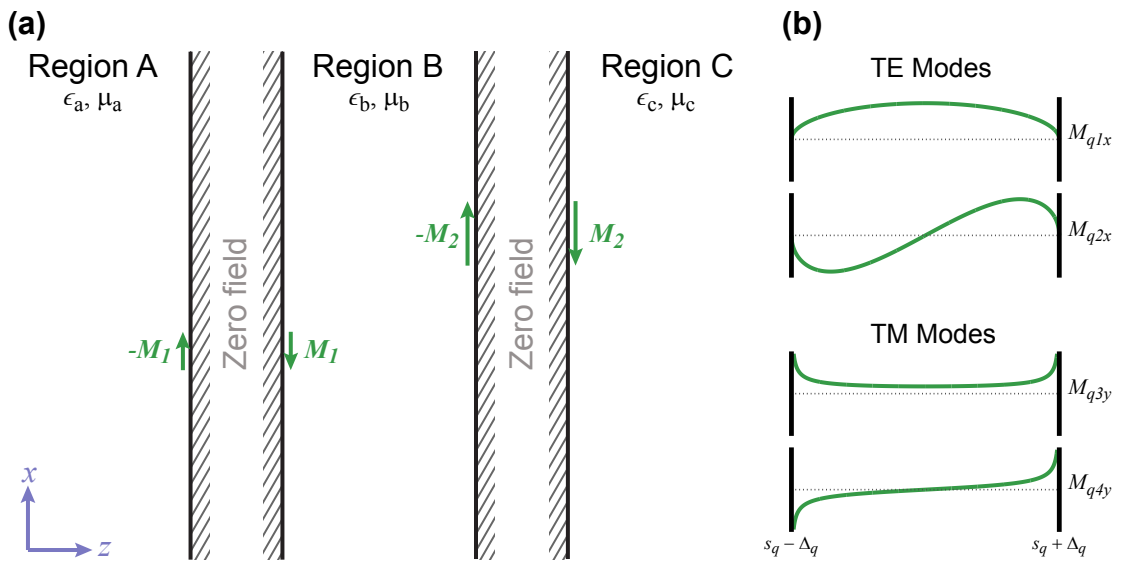

Figure 2.2: (a) The three separate regions of the two-slit structure after using the equivalence principle to replace the slits with magnetic current sheets backed by perfect electrical conductors. The magnetic current directions shown are those for TE excitation. For TM excitation, the currents are in the $\pm\hat{y}$ direction. (b) The lowest order magnetic current modes in the slits, from eq. 2.6.

equivalence principle, based on the uniqueness theorem for Maxwell's equations, states that two different sources producing the same field within a region of space are equivalent. In particular, the three connected regions of figure 2.1 can be represented by the equivalent separate regions of figure 2.2a, with each slit replaced by a perfect electrical conductor backing a (fictitious) magnetic current given by:

$$\boldsymbol{M_q} = \boldsymbol{E_q} \times \hat{\boldsymbol{n}} \tag{2.2}$$

where $\boldsymbol{E_q}$ is the electric field within each slit, and $\hat{\boldsymbol{n}}$ is the outward-pointing unit normal vector.

This approach allows us to consider each region separately. The continuity of the tangential electric field is enforced by using equal and opposite magnetic currents in adjacent regions for each slit. By calculating the fields produced by the magnetic currents in each slit, $\boldsymbol{H}(\boldsymbol{M_q})$, we can also write equations for the continuity of the tangential magnetic field:

$$\boldsymbol{H_t^a}(-\boldsymbol{M_1}) - \boldsymbol{H_t^b}(\boldsymbol{M_1}) - \boldsymbol{H_t^b}(-\boldsymbol{M_2}) = -\boldsymbol{H_t^{sc}} \qquad \text{over slit 1} \tag{2.3a}$$

$$\boldsymbol{H_t^b}(\boldsymbol{M_1}) + \boldsymbol{H_t^b}(-\boldsymbol{M_2}) - \boldsymbol{H_t^c}(\boldsymbol{M_2}) = 0 \qquad \text{over slit 2} \tag{2.3b}$$

In eq. 2.3a, H_t^{sc} is the "short-circuit" magnetic field corresponding to the incident field in region A with the slit replaced by a PEC.

If we have the solution to eq. 2.3, then we are done. Unfortunately, we don't know *a priori* the precise form of the magnetic current in each slit. To make progress, we can expand the magnetic current as the sum of an orthogonal set of basis functions,

$$\boldsymbol{M_q} = \sum_{n=1}^{\infty} V_{qn} \boldsymbol{M_{qn}} \tag{2.4}$$

and define an inner product for each slit:

$$\langle \boldsymbol{A}, \boldsymbol{B} \rangle_q = \int_{s_q - \Delta_q}^{s_q + \Delta_q} \boldsymbol{A} \cdot \boldsymbol{B} \, \mathrm{d}x \,, \qquad q = 1, 2 \tag{2.5}$$

Eq. 2.3 can then be projected onto each mode $\boldsymbol{M_{qn}}$ to give a set of linear algebraic equations for the coefficients V_{qn}.

Butler and Wilton [66] have already calculated analytic expressions for the modes in a single narrow slit. We will take a shortcut by choosing their solutions as the basis functions in this problem. The two lowest-order modes in each polarization are given by:

$$\text{TE} \begin{cases} \boldsymbol{M_{q1}} = \hat{\boldsymbol{x}} \sqrt{\Delta_q^2 - (x - s_q)^2} \\ \boldsymbol{M_{q2}} = \hat{\boldsymbol{x}} \, (x - s_q) \sqrt{\Delta_q^2 - (x - s_q)^2} \end{cases} \tag{2.6a}$$

$$\text{TM} \begin{cases} \boldsymbol{M_{q3}} = \hat{\boldsymbol{y}} \, \dfrac{1}{\sqrt{\Delta_q^2 - (x - s_q)^2}} \\ \boldsymbol{M_{q4}} = \hat{\boldsymbol{y}} \, \dfrac{(x - s_q)}{\sqrt{\Delta_q^2 - (x - s_q)^2}} \end{cases} \tag{2.6b}$$

These modes are plotted in figure 2.2b. The assumption is that the slit modes occurring in our problem with two parallel walls are well approximated by the solutions for a single slotted wall. This is likely to be true for slits that are narrow compared to the wavelength and wall separation.

Sometimes, the polarization and symmetry of the incident field will allow us to use only one of the modes from eq. 2.6, taking the other V_{qn} coefficients to be zero. In that case, projecting eq. 2.3 using the inner product gives an especially simple form:

$$Y_{11}^{an} V_{1n} + Y_{11}^{bn} V_{1n} + Y_{12}^{bn} V_{2n} = I_1^{an} \tag{2.7a}$$

$$Y_{21}^{bn} V_{1n} + Y_{22}^{bn} V_{2n} + Y_{22}^{cn} V_{2n} = 0 \tag{2.7b}$$

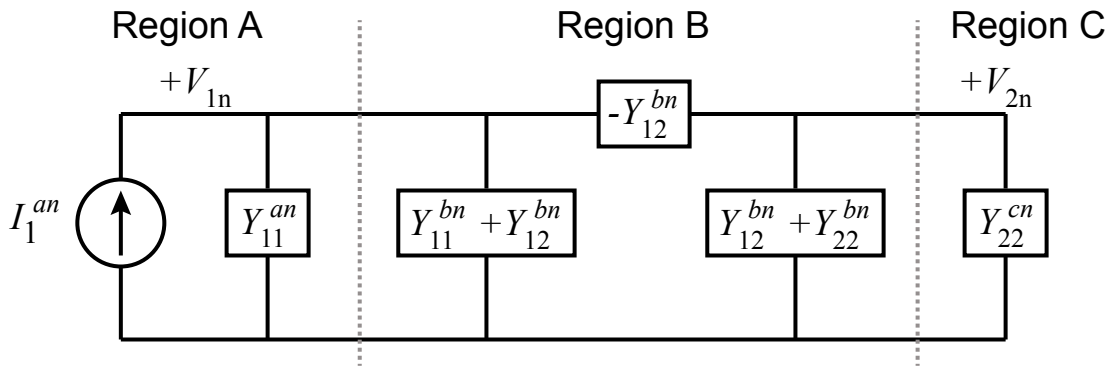

Figure 2.3: Equivalent circuit model for the two-slit structure when each slit supports only one mode, $\boldsymbol{M_{qn}}$.

where the matrix elements are defined as follows:

$$\begin{aligned} Y_{qq}^{pn} &= -\left\langle \boldsymbol{M_{qn}}, \boldsymbol{H_t^p}(\boldsymbol{M_{qn}}) \right\rangle_q \\ Y_{qr}^{bn} &= \left\langle \boldsymbol{M_{qn}}, \boldsymbol{H_t^p}(\boldsymbol{M_{rn}}) \right\rangle_q , \qquad q \neq r \\ I_1^{an} &= -\left\langle \boldsymbol{M_{qn}}, \boldsymbol{H_t^{sc}} \right\rangle_1 \end{aligned} \tag{2.8}$$

The notation in eq. 2.7 has been chosen suggestively. The equations are the same as those for the generalized electrical circuit network shown in figure 2.3, with generalized admittances Y_{qr}^{pm}, generalized source current I_1^{an}, and generalized node voltages V_{qn}. After calculating the various generalized admittances (see Appendix A), the "transfer admittance" Y_{12} will give the magnetic current magnitude in the second slit for a given incident field:

$$Y_{12} = \frac{I_1^{an}}{V_{2n}} = \frac{Y_{12}^{bn}Y_{21}^{bn} - (Y_{11}^{an}+Y_{11}^{bn})(Y_{22}^{bn}+Y_{22}^{cn})}{Y_{21}^{bn}} \tag{2.9}$$

Finally, the circuit analogy gives the time average power transmitted into region C:

$$P_{trans} = \frac{1}{2}\left|\frac{I_1^{an}}{Y_{12}}\right|^2 \mathrm{Re}\left\{Y_{22}^{cn}\right\} \tag{2.10}$$

As suggested by the circuit analogy, maximizing the transmission through the slits is equivalent to an impedance matching problem.

2.2.1 Single Slit, TE Case

As a demonstration of the method, we will first calculate the transmitted power in the simpler case where there is only one conducting wall and only one slit located at $(x, z) = (0, 0)$

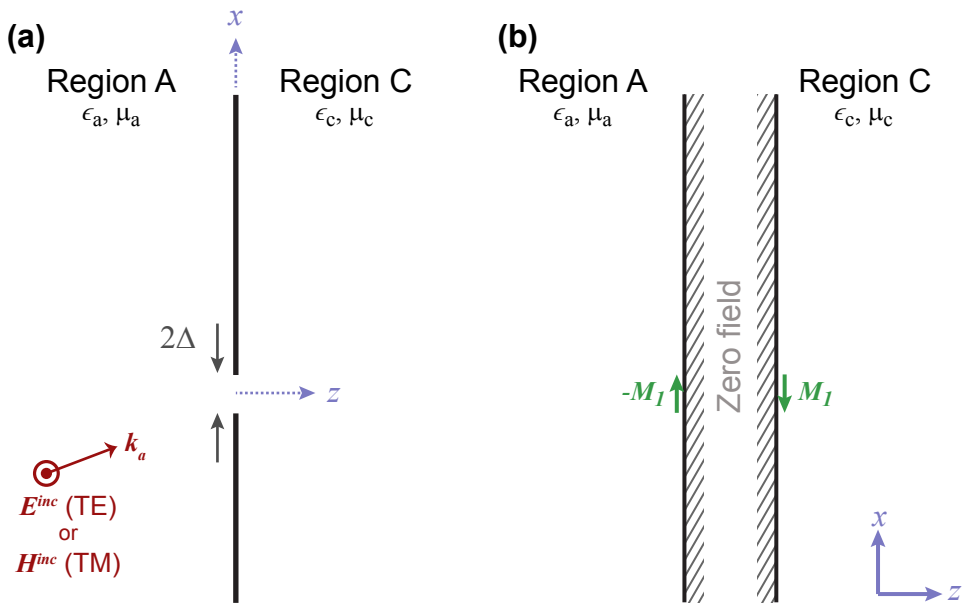

Figure 2.4: (a) Schematic of the one-slit structure. (b) The two separate regions of the one-slit structure after using the equivalence principle to replace the slit with magnetic current sheets backed by perfect electrical conductors. The magnetic current directions shown are those for TE excitation. For TM excitation, the currents are in the $\pm\hat{y}$ direction.

(see figure 2.4). This will also give a baseline for assessing the transmission enhancement produced by introducing a second slit.

Let $\boldsymbol{E^{sc}}$ be the following TE solution of Helmholtz' equation for $z < 0$ when the slit is short-circuited (replaced with perfect conductors), (assuming $e^{-i\omega t}$ time dependence and expressed in polar coordinates):

$$\begin{aligned}\boldsymbol{E^{sc}} &= \hat{\boldsymbol{y}} E_0 J_1(k_a\rho)\sin\varphi \\ &= \hat{\boldsymbol{y}} E_0 \sin\varphi \cdot \frac{1}{2}\left[H_1^{(1)}(k_a\rho) + H_1^{(2)}(k_a\rho)\right]\end{aligned} \tag{2.11}$$

Here, k_a is the wavevector magnitude in region a, ρ is the distance from the slit ($\rho^2 = x^2 + z^2$), and φ is the angle between the vector $\hat{\rho}$ and the x-axis ($\sin\varphi = -z/\rho$). J_1 is a first-order Bessel function, and $H_1^{(1)}$ and $H_1^{(2)}$ are first order Hankel functions of the first and second kind, which represent the superimposed outgoing and incoming waves, respectively. The incoming wave represents a diffraction limited beam focused on the slit.

We can find the total average power per unit length carried by the incoming wave by integrating the radial component of the Poynting vector over a semicircle centered on the slit location. A simple approach is to consider a large semicircle of radius $k_a L \gg 1$, so that

the Hankel function can be replaced with its large argument approximation [67].

$$\boldsymbol{E^{inc}} \simeq \hat{\boldsymbol{y}} \frac{E_0}{2} \sqrt{\frac{2}{\pi k_a \rho}} e^{-i(k_a \rho - \frac{3\pi}{4})} \sin\varphi$$
$$\boldsymbol{H^{inc}} = \frac{1}{i\eta_a k_a} \nabla \times \boldsymbol{E^{inc}}$$

where $\eta_a = \sqrt{\mu/\epsilon_a}$ is the impedance of region a. Then the time-average power per unit length is:

$$\begin{aligned} P_{inc} &= \int_0^{\pi} -\hat{\boldsymbol{\rho}} \cdot \frac{1}{2} \mathrm{Re}\{\boldsymbol{E^{inc}} \times \boldsymbol{H^{inc}}\} \, \mathrm{d}\varphi \\ &= \frac{|E_0|^2}{8\eta_a k_a} \end{aligned} \tag{2.12}$$

Also of interest is the tangential component of the short-circuit magnetic field at the slit location. For a TE incident field, $\boldsymbol{H_t^{sc}}$ is oriented in the $\hat{x}$ direction, with a magnitude at $x, z = 0$ given by:

$$\begin{aligned} H_t^{sc} &= \hat{\boldsymbol{x}} \cdot \left. \frac{\nabla \times \boldsymbol{E^{sc}}}{i\eta_a k_a} \right|_{x,z=0} = \frac{1}{i\eta_a k_a} \lim_{\rho \to 0} \left(\frac{1}{\rho} \left. \frac{\partial E_y^{sc}}{\partial \varphi} \right|_{\varphi=0} \right) \\ &= \frac{E_0}{2i\eta_a} \end{aligned} \tag{2.13}$$

If the slit width is small relative to the wavelength, $k_a \Delta \ll 1$, then for our purposes we can treat this tangential field as approximately constant over the slit area.

The matching condition for the tangential magnetic field in the slit is:

$$-\boldsymbol{H_t^a}(\boldsymbol{M_1}) - \boldsymbol{H_t^c}(\boldsymbol{M_1}) = -\boldsymbol{H_t^{sc,a}} \tag{2.14}$$

Noting that this incident TE field is even with respect to reflection across the $x = 0$ plane, and assuming a small slit width, the magnetic current in the slit can be well approximated using just the first (even) TE mode from eq. 2.6a. That is,

$$\boldsymbol{M_1} = V_{11} \boldsymbol{M_{11}} = \hat{\boldsymbol{x}} V_{11} \sqrt{\Delta^2 - x^2} \tag{2.15}$$

Projecting each term in equation 2.14 onto $\boldsymbol{M_{11}}$ and using equation 2.15 gives a linear equation that can be solved for the magnetic current coefficient V_{11}:

$$Y_{11}^{a1} V_{11} + Y_{11}^{c1} V_{11} = I_1^{a1} \tag{2.16}$$

Here, the generalized input current I_1^{a1} is given by

$$\begin{aligned} I_1^{a1} &= -\left\langle \boldsymbol{M_{11}}, \boldsymbol{H_t^{sc}} \right\rangle = -\int_{\Delta}^{\Delta} \sqrt{\Delta^2 - x^2} \frac{E_0}{2i\eta_a} \, \mathrm{d}x \\ &= \frac{iE_0}{4\eta_a} \pi \Delta^2 \end{aligned} \tag{2.17}$$

And for a small slit width ($k\Delta \ll 1$), the generalized admittances Y_{11}^{a1} and Y_{11}^{c1} are given by

$$\begin{aligned} Y_{11}^{i1} &= -\left\langle \boldsymbol{M_{11}}, \boldsymbol{H_t^i}(\boldsymbol{M_{11}}) \right\rangle \\ &= \frac{\pi^2 k_i \Delta^4}{16\eta_i} + \frac{i\pi k_i \Delta^4}{4\eta_i} \left[\ln\left(\frac{\alpha k_i \Delta}{2\pi} \right) + \frac{1}{4} \right] + \frac{i\pi\Delta^2}{2\eta_i k_i} \end{aligned} \tag{2.18}$$

In eq. 2.18, the index $i = a$ or c is the appropriate region. $\alpha = 1.696915\ldots$. Appendix A has detailed derivations of equations 2.17 and 2.18. Note that in the small-slit limit $k\Delta \to 0$, the last term in eq. 2.18 dominates the others.

Using the circuit model implied by equation 2.16, we can solve for the generalized voltage V_{11} and consequently find the time-average power transmitted into region c:

$$P_{trans} = \frac{1}{2} \left| \frac{I_1^{a1}}{Y_{11}^{a1} + Y_{11}^{c1}} \right|^2 \mathrm{Re}\left\{ Y_{11}^{c1} \right\} \tag{2.19}$$

For the case where regions a and c are identical (so $Y_{11}^{a1} = Y_{11}^{c1}$), using the input current from eq. 2.17, and using only the last, dominant term of eq. 2.18, we find the transmitted power in the small-slit limit to be:

$$P_{trans} \simeq \frac{|E_0|^2 \pi^2 k^2 \Delta^4}{512\eta} \tag{2.20}$$

and using the incident power from eq. 2.12, the transmission efficiency for the TE case is:

$$T = \frac{P_{trans}}{P_{inc}} \simeq \frac{\pi^2 (k\Delta)^4}{64} \tag{2.21}$$

2.2.2 Single Slit, TM Case

Proceeding as in section 2.2.1, we define an incident TM field representing a diffraction limited beam focused on the slit. Let $\boldsymbol{H^{sc}}$ be the following TM solution of Helmholtz' equation for $z < 0$ when the slit is short-circuited (replaced with perfect conductors),

(assuming $e^{-i\omega t}$ time dependence and expressed in polar coordinates):

$$\begin{aligned}\boldsymbol{H^{sc}} &= \hat{\boldsymbol{y}} H_0 J_0(k_a\rho) \\ &= \hat{\boldsymbol{y}}\frac{H_0}{2}\left[H_0^{(1)}(k_a\rho) + H_0^{(2)}(k_a\rho)\right]\end{aligned} \tag{2.22}$$

J_0 is a zero-order Bessel function, and $H_0^{(1)}$ and $H_0^{(2)}$ are zero-order Hankel functions of the first and second kind, which represent the superimposed outgoing and incoming waves, respectively.

The incoming wave, representing a diffraction limited beam focused on the slit, is therefore described by:

$$\begin{aligned}\boldsymbol{H^{inc}} &= \hat{\boldsymbol{y}}\frac{H_0}{2}H_0^{(2)}(k_a\rho) \\ &\simeq \hat{\boldsymbol{y}}\frac{H_0}{2}\sqrt{\frac{2}{\pi k_a\rho}}e^{-i(k_a\rho-\frac{\pi}{4})} \qquad (k_a\rho \gg 1) \\ \boldsymbol{E^{inc}} &= \frac{i\eta_a}{k_a}\nabla\times\boldsymbol{H^{inc}}\end{aligned}$$

with incident power per unit length given by:

$$P_{inc} = \frac{|H_0|^2\eta_a}{4k_a} \tag{2.23}$$

Given the symmetry of the incident field and assuming a small slit width, the magnetic current in the slit can be well approximated using just the first TM mode from eq. 2.6b. That is,

$$\boldsymbol{M_1} = V_{13}\boldsymbol{M_{13}} = \hat{\boldsymbol{x}}\frac{V_{13}}{\sqrt{\Delta^2 - x^2}} \tag{2.24}$$

Projecting each term in equation 2.14 onto $\boldsymbol{M_{13}}$ and using equation 2.24 gives a linear equation that can be solved for the magnetic current coefficient V_{13}:

$$Y_{11}^{a3}V_{13} + Y_{11}^{c3}V_{13} = I_1^{a3} \tag{2.25}$$

Here, the generalized input current I_1^{a3} is given by

$$\begin{aligned}I_1^{a3} &= -\left\langle \boldsymbol{M_{13}}, \boldsymbol{H_t^{sc}}\right\rangle = -\int_{\Delta}^{\Delta}\frac{H_0}{\sqrt{\Delta^2 - x^2}}\,\mathrm{d}x \\ &= -\pi H_0\end{aligned} \tag{2.26}$$

And for a small slit width ($k\Delta \ll 1$), the generalized admittances Y_{11}^{a3} and Y_{11}^{c3} have been

derived by Leviatan [29] (see eq. 2.40a):

$$\begin{aligned} Y_{11}^{i3} &= -\left\langle \boldsymbol{M_{13}}, \boldsymbol{H_t^i}(\boldsymbol{M_{13}}) \right\rangle \\ &= \frac{\pi^2 k_i}{2\eta_i} + i\frac{k_i \pi}{\eta_i} \ln\left(\frac{\gamma k_i \Delta}{4}\right) \end{aligned} \tag{2.27}$$

In eq. 2.27, $\gamma = 1.7810724\ldots$. Note that in the small-slit limit $k\Delta \to 0$, the second term in eq. 2.27 dominates the first.

Using the circuit model implied by equation 2.25, we can solve for the generalized voltage V_{13} and consequently find the time-average power transmitted into region c:

$$P_{trans} = \frac{1}{2}\left|\frac{I_1^{a3}}{Y_{11}^{a3} + Y_{13}^{c1}}\right|^2 \text{Re}\left\{Y_{11}^{c3}\right\} \tag{2.28}$$

For the case where regions a and c are identical (so $Y_{11}^{a3} = Y_{11}^{c3}$), using the input current from eq. 2.26, and using only the last, dominant term of eq. 2.27, we find the transmitted power in the small-slit limit to be:

$$P_{trans} \simeq \frac{\eta_a |H_0|^2 \pi^2}{16 k_a \left[\ln(\frac{\gamma k_a \Delta}{4})\right]^2} \tag{2.29}$$

and using the incident power from eq. 2.23, the asymptotic transmission efficiency for the TM case is:

$$T = \frac{P_{trans}}{P_{inc}} \simeq \frac{\pi^2}{4}\left[\ln\left(\frac{\gamma k_a \Delta}{4}\right)\right]^{-2} \tag{2.30}$$

Notably, the transmitted power in the TM case is much higher than that in the TE case (eq. 2.21), by a factor on the order of $(k\Delta)^{-4}\ln^{-2}(k\Delta)$.

2.2.3 Two Slits, TE Case

Returning to the two-slit problem (figures 2.1 and 2.2), we will again consider the focused incident TE field of eq. 2.11. Based on the incident field symmetry, we will perform a one mode expansion in each slit with $\boldsymbol{M_q} = V_{q1}\boldsymbol{M_{q1}}$. The applicable generalized admittances

are:

$$Y_{11}^{a1} \simeq \frac{\pi^2 k_a \Delta_1^4}{16\eta_a} + i\frac{\pi k_a \Delta_1^4}{4\eta_a}\left[\ln\left(\frac{\alpha k_a \Delta_1}{2\pi}\right) + \frac{1}{4}\right] + i\frac{\pi\Delta_1^2}{2\eta_a k_a} \tag{2.31a}$$

$$\begin{aligned} Y_{11}^{b1} \simeq & \frac{\pi^2 k_b \Delta_1^4}{16\eta_b} + i\frac{\pi k_b \Delta_1^4}{4\eta_b}\left[\ln\left(\frac{\alpha k_b \Delta_1}{2\pi}\right) + \frac{1}{4}\right] + i\frac{\pi\Delta_1^2}{2\eta_b k_b} \\ & + \frac{k_b}{\eta_b}\sum_{n=1}^{N_1}\int_{-\Delta_1}^{\Delta_1}\int_{-\Delta_1}^{\Delta_1}\sqrt{\Delta_1^2 - x^2}\sqrt{\Delta_1^2 - x'^2}H_0^{(1)}(k_b\sqrt{(x-x')^2 + (2nd)^2})\,\mathrm{d}x'\,\mathrm{d}x \\ & + \frac{1}{\eta_b}\sum_{n=1}^{N_1}\int_{-\Delta_1}^{\Delta_1}\int_{-\Delta_1}^{\Delta_1}\frac{\sqrt{\Delta_1^2 - x^2}}{\sqrt{\Delta_1^2 - x'^2}}\frac{x'(x-x')}{\sqrt{(x-x')^2 + (2nd)^2}}H_1^{(1)}(k_b\sqrt{(x-x')^2 + (2nd)^2})\,\mathrm{d}x'\,\mathrm{d}x \\ & + \sum_{n=N_1+1}^{\infty}\left[\frac{\pi^2\Delta_1^4 k_b}{4\eta_b}\left(H_0^{(1)}(2k_b nd) - \frac{H_1^{(1)}(2k_b nd)}{2k_b nd}\right)\right] \end{aligned} \tag{2.31b}$$

$$\begin{aligned} Y_{12}^{b1} \simeq & -\frac{k_b}{2\eta_b}\sum_{n=1}^{N_{12}}\int_{-\Delta_1}^{\Delta_1}\int_{s_2-\Delta_2}^{s_2+\Delta_2}\sqrt{\Delta_1^2 - x^2}\sqrt{\Delta_2^2 - (x'-s_2)^2} \\ & \qquad \times H_0^{(1)}(k_b\sqrt{(x-x')^2 + [(2n-1)d]^2})\,\mathrm{d}x'\,\mathrm{d}x \\ & - \frac{1}{2\eta_b}\sum_{n=1}^{N_{12}}\int_{-\Delta_1}^{\Delta_1}\int_{s_2-\Delta_2}^{s_2+\Delta_2}\frac{\sqrt{\Delta_1^2 - x^2}}{\sqrt{\Delta_2^2 - (x'-s_2)^2}}\frac{(x'-s_2)(x-x')}{\sqrt{(x-x')^2 + [(2n-1)d]^2}} \\ & \qquad \times H_1^{(1)}(k_b\sqrt{(x-x')^2 + [(2n-1)d]^2})\,\mathrm{d}x'\,\mathrm{d}x \\ & + \sum_{n=N_{12}+1}^{\infty}\left[\frac{\pi^2\Delta_1^2\Delta_2^2 k_b}{4\eta_b}\left(-H_0^{(1)}(k_b\sqrt{s_2^2 + [(2n-1)d]^2}) + \frac{H_1^{(1)}(k_b\sqrt{s_2^2 + [(2n-1)d]^2})}{k_b\sqrt{s_2^2 + [(2n-1)d]^2}}\right)\right] \end{aligned} \tag{2.31c}$$

$$Y_{21}^{b1} = Y_{12}^{b1} \qquad \text{(reciprocity)} \tag{2.31d}$$

$$\begin{aligned} Y_{22}^{b1} \simeq & \frac{\pi^2 k_b \Delta_2^4}{16\eta_b} + i\frac{\pi k_b \Delta_2^4}{4\eta_b}\left[\ln\left(\frac{\alpha k_b \Delta_2}{2\pi}\right) + \frac{1}{4}\right] + i\frac{\pi\Delta_2^2}{2\eta_b k_b} \\ & + \frac{k_b}{\eta_b}\sum_{n=1}^{N_2}\int_{-\Delta_2}^{\Delta_2}\int_{-\Delta_1}^{\Delta_2}\sqrt{\Delta_2^2 - x^2}\sqrt{\Delta_2^2 - x'^2}H_0^{(1)}(k_b\sqrt{(x-x')^2 + (2nd)^2})\,\mathrm{d}x'\,\mathrm{d}x \\ & + \frac{1}{\eta_b}\sum_{n=1}^{N_2}\int_{-\Delta_2}^{\Delta_2}\int_{-\Delta_2}^{\Delta_2}\frac{\sqrt{\Delta_2^2 - x^2}}{\sqrt{\Delta_2^2 - x'^2}}\frac{x'(x-x')}{\sqrt{(x-x')^2 + (2nd)^2}}H_1^{(1)}(k_b\sqrt{(x-x')^2 + (2nd)^2})\,\mathrm{d}x'\,\mathrm{d}x \\ & + \sum_{n=N_2+1}^{\infty}\left[\frac{\pi^2\Delta_2^4 k_b}{4\eta_b}\left(H_0^{(1)}(2k_b nd) - \frac{H_1^{(1)}(2k_b nd)}{2k_b nd}\right)\right] \end{aligned} \tag{2.31e}$$

$$Y_{22}^{c1} \simeq \frac{\pi^2 k_c \Delta_2^4}{16\eta_c} + i\frac{\pi k_c \Delta_2^4}{4\eta_c}\left[\ln\left(\frac{\alpha k_c \Delta_2}{2\pi}\right) + \frac{1}{4}\right] + i\frac{\pi\Delta_2^2}{2\eta_c k_c} \tag{2.31f}$$

In eq. 2.31, N_1 is the largest integer n such that $n^2 \leq (10\Delta_1/d)^2$, N_{12} is the largest integer n such that $(2n-1)^2 \leq (10(\Delta_1+\Delta_2)/d)^2$, and N_2 is the largest integer n such that $n^2 \leq (10\Delta_2/d)^2$. $\alpha = 1.696915\ldots$. While these expressions may seem intimidating, they can easily and quickly be numerically calculated on a personal computer using standard software such as MATLAB. Appendix A contains a detailed derivation of these expressions, as well as some further refinements to reduce computation time and minimize numerical errors when computing the infinite sums.

$$Y_{11} = \frac{I_1^{a1}}{V_{11}} = \frac{(Y_{11}^{a1}+Y_{11}^{b1})(Y_{22}^{b1}+Y_{22}^{c1}) - Y_{12}^{b1}Y_{21}^{b1}}{(Y_{22}^{b1}+Y_{22}^{c1})} \tag{2.32a}$$

$$Y_{12} = \frac{I_1^{a1}}{V_{21}} = \frac{(Y_{11}^{a1}+Y_{11}^{b1})(Y_{22}^{b1}+Y_{22}^{c1}) - Y_{12}^{b1}Y_{21}^{b1}}{-Y_{21}^{b1}} \tag{2.32b}$$

$$P_{trans} = \frac{1}{2}\left|\frac{I_1^{a1}}{Y_{12}}\right|^2 \text{Re}\left\{Y_{22}^{c1}\right\} \tag{2.33}$$

With the TE excitation and corresponding I_1^a given in eqs. 2.11 and 2.17, the transmitted power is:

$$T = \frac{P_{trans}}{P_{inc}} = \frac{\pi^2 k_a \Delta_1^4}{4\eta_a}\left|\frac{1}{Y_{12}}\right|^2 \text{Re}\{Y_{22}^{c1}\} \tag{2.34}$$

2.2.3.1 Special case: symmetric slits and perfect transmission

Let us now apply these results to the special case of symmetric slits that was treated in ref. [18]. That is, $s_2 = 0$, $\Delta_1 = \Delta_2 = \Delta$, and the material properties are the same in all three regions. It follows that $Y_{11}^{a1} = Y_{22}^{c1}$ and $Y_{11}^{b1} = Y_{22}^{b1}$. Figure 2.5 shows the TE transmission spectrum when $\Delta = d/10$ as calculated using eq. 2.34, as well as the electric field magnitude at three frequencies of interest (for details of how to compute the field once the slits' magnetic current amplitudes V_{11} and V_{21} are known, see Appendix A). As can be seen from the figure, the system exhibits greatly enhanced transmission (approaching perfect transmission) at a frequency near, but slightly below, the first cutoff frequency of the parallel plate waveguide, $f_c = c/2d$. The transmission peak is narrowband, with a quality factor in this case given by $Q = f/\delta f \simeq 5500$, where δf is the peak's full width at half-maximum transmission.

We can gain insight into this behavior by writing the magnetic current amplitudes for each slit, from eq. 2.32, in the form:

$$V_{11} = \frac{A}{A^2-B^2}I_1^{a1} \qquad , \qquad V_{21} = \frac{-B}{A^2-B^2}I_1^{a1} \tag{2.35}$$

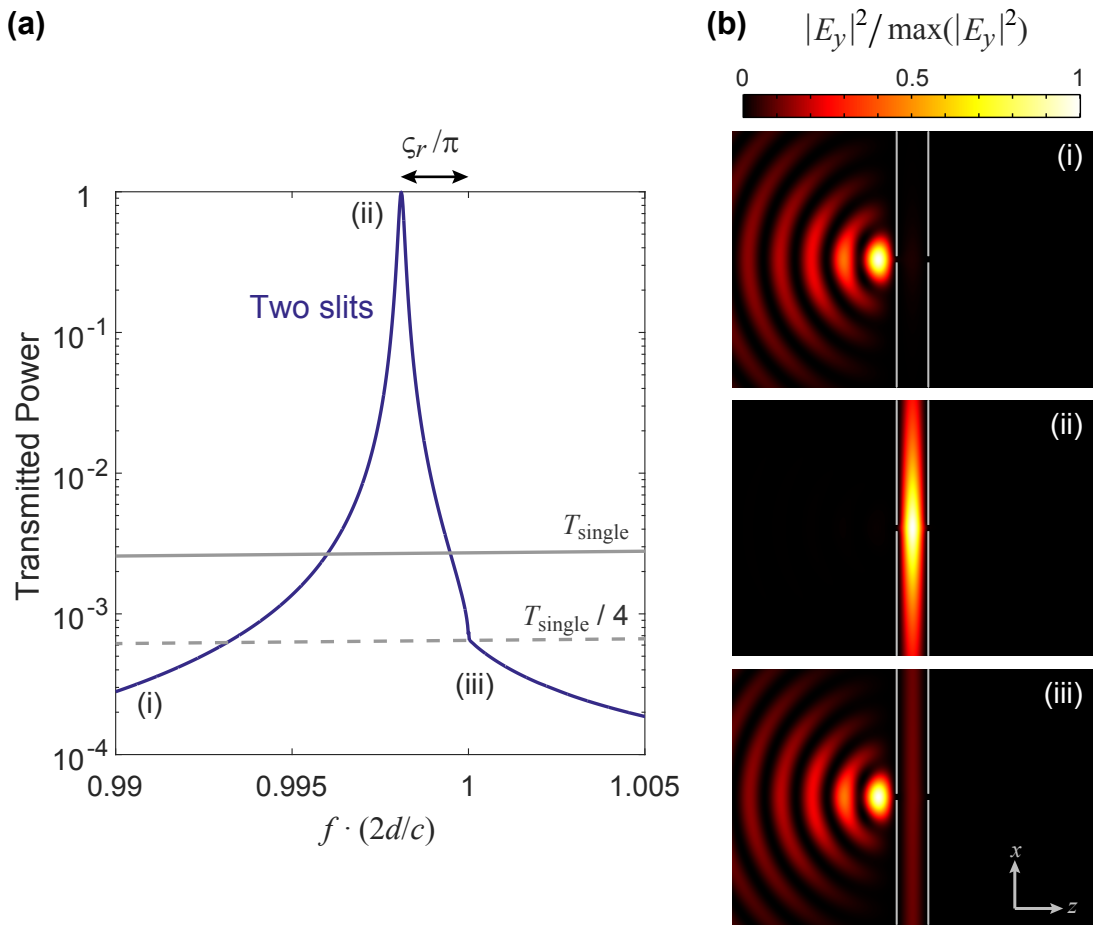

Figure 2.5: (a) TE transmitted power spectrum through the two parallel slotted screens separated by distance d with $\Delta_1 = \Delta_2 = d/10$ (blue solid line), as well as the transmitted power T_{single} through a single slotted screen with the same slit dimension (gray solid and dashed lines), near the first waveguide cutoff frequency $f_c = c/2d$. (b) Contour plots of $|E_y(x,z)|^2$, normalized to the highest value, at three representative frequencies: (i) below resonance ($\varsigma = 10\varsigma_r$), frequency of maximum power transmission ($\varsigma = \varsigma_r$), and (iii) the waveguide cutoff frequency ($\varsigma = 0$). Waves are incident from the left.

where $A = Y_{22}^{b1} + Y_{22}^{c1}$, and $B = Y_{12}^{b1}$. Notice from eq. 2.31 that these generalized admittances have singularities at the waveguide cutoff frequencies given by $kd = m\pi\,, (m = 1, 2, ...)$. Following [18], we can expand near the first cutoff frequency $f_c = c/2d$ and write $kd = \pi - \varsigma$ ($|\varsigma| \ll 1$). Near this cutoff frequency, A and B are approximately:

$$B = Y_{12}^{b1} \simeq -\frac{k\pi\Delta^4}{8\eta}\sqrt{\frac{2\pi}{|\varsigma|}} \times \begin{cases} i\,, & \varsigma > 0 \\ -1\,, & \varsigma < 0 \end{cases} \tag{2.36a}$$

$$A = Y_{22}^{b1} + Y_{22}^{c1} \simeq B + \frac{\pi^2 k\Delta^4}{16\eta} + \frac{i\pi k\Delta^4}{2\eta}\left[\ln\left(\frac{\alpha k\Delta}{2\pi}\right) + \frac{1}{4} + \frac{2}{k^2\Delta^2}\right] \tag{2.36b}$$

Point (i) in figure 2.5 represents frequencies well below f_c, for which $|B| \ll |A|$. From this, we can conclude that the magnetic current amplitude for the second slit, and thus the power transmitted into region C, is vanishingly small. In fact, as discussed more later, the power transmittance far from resonance is of the order $T \sim T_{\text{single}}^2$, where T_{single} is the TE transmittance through a single slotted screen. This is the transmission behavior that would be expected for light that passes through two slotted screens in series, with no interaction effects between the slits.

Of particular interest is the resonant frequency marked by point (ii), for which $\text{Im}\{A\} = -\text{Im}\{B\}$. That is, when

$$\varsigma = \varsigma_r \simeq \frac{\pi}{2}\left[\ln\left(\frac{\alpha k\Delta}{2\pi}\right) + \frac{1}{4} + \frac{2}{k^2\Delta^2}\right]^{-2} \tag{2.37}$$

Noting that $\text{Re}\{B\} = 0$ and $\text{Re}\{A\} \ll \text{Im}\{A\}$ when $k\Delta$ is small, we can calculate the transmitted power using eq. 2.34 as:

$$\begin{aligned} T &= \frac{\pi^2 k\Delta^4}{4\eta_a}\left|\frac{1}{Y_{12}}\right|^2 \text{Re}\{Y_{22}^{c1}\} \\ &= 4\text{Re}\{A\}\left|\frac{-B}{A^2 - B^2}\right|^2 \text{Re}\{A\} \\ &= 4\text{Re}\{A\}^2\left|\frac{i\text{Im}\{A\}}{\text{Re}\{A\}\left(\text{Re}\{A\} + i2\text{Im}\{A\}\right)}\right|^2 \\ &\to 1 \qquad (\text{as } k\Delta \to 0) \end{aligned} \tag{2.38}$$

That is, there is a resonant frequency *below* the waveguide's first cutoff frequency (by an amount $\delta f = \varsigma_r f_c/\pi$) for which perfect power transmission occurs through vanishingly narrow slits. From eqs. 2.38 and 2.36, the transmission peak's quality factor is $Q = f/\delta f \sim \varsigma_r^{-3/2}$. In addition, at the resonance frequency $V_{11} \simeq V_{21}$, so $M_2 = -M_1$; the

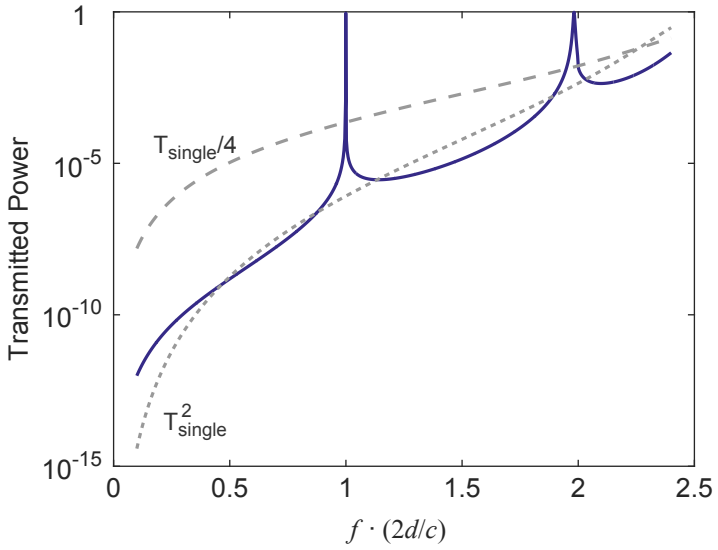

Figure 2.6: TE transmitted power spectrum through the two parallel slotted screens separated by distance d with $\Delta_1 = \Delta_2 = 0.08d$ (solid blue line), including the first two resonant peaks. For comparison, the dashed and dotted gray lines show $1/4$th the TE transmission through a single screen with the same slit dimension, and the square of the transmission through a single slit, respectively.

magnetic currents and fields in the two slits are equal and π radians out of phase.

Figure 2.5b(ii) shows the field profile at this resonance frequency. A strong field exists between the plates, localized to the slits. In this sense the resonance is similar to that in a conventional cavity, although of course in this case the field is not confined entirely by walls. Instead, power is prevented from propagating in the $\pm x$ directions because the resonance occurs below the TE cutoff frequency of the parallel plate waveguide; the field at $z = 0$ decays exponentially as $|E_y|^2 \sim \exp(-\alpha|x|)$ with $\alpha = k_b(8\varsigma_r/\pi)^{1/2}$.

Finally, point (iii) is the waveguide cutoff frequency. The transmission spectrum exhibits a cusp due to the onset of the continuum of TE waveguide modes. Approaching point (iii) corresponds to $B \to \infty$, giving:

$$V_{21} = \frac{-BI_1^{a1}}{(A-B)(A+B)} \simeq \frac{-I_1^{a1}}{2(A-B)} \simeq \frac{-I_1^{a1}}{4Y_{11}^{a1}} \tag{2.39}$$

Comparing this result to eq. 2.19, we find that at the cutoff frequency f_c, the magnetic current magnitude in the second slit is half of that for a single slit. Consequently, the transmission at the waveguide cutoff frequency is the same order as the transmission through a single slit, $T = T_{\text{single}}/4$. Figure 2.5b(iii) shows the field profile at the waveguide cutoff frequency.

Figure 2.6 further illustrates the relation between the 2-slit transmission T and the transmission through a single slit T_{single}. At the TE waveguide cutoff frequencies given by $f_{c,m} = mc/2d$, the 2-slit transmission is equal to $1/4$th the transmission through a single slit (seen more clearly in figure 2.5). At resonant frequencies slightly below the waveguide cutoffs, the system exhibits perfect transmission. Far from resonance, $T \simeq T_{\text{single}}^2$, as would be expected from two slits in series that don't interact with each other.

Notably, the second resonance at $f \simeq c/d$ exhibits perfect transmission, even though the resonant state overlaps in frequency with the propagating TE waveguide modes that have a cutoff at $f_{c,1} = c/2d$. This is because the slit-bound state and the waveguide modes have opposite parity with respect to reflection across the $z = 0$ plane, and are thus prevented by their symmetries from exchanging energy with each other. The second transmission peak is wider than the first, as expected since $k\Delta$ is twice as large. In fact, the lower Q exhibited by the second order peak may make it more useful in certain applications, because the overall transmission will be higher once conduction losses are accounted for [68].

2.2.3.2 Effects of varying slit width and asymmetric slits

Figure 2.7 shows the calculated TE transmitted power spectrum near the first resonance for a variety of slit widths, ranging from $\Delta = 0.1d$ to $\Delta = 0.03d$. If the two slits remain symmetric, with $\Delta_1 = \Delta_2$, then the perfect transmission on resonance is preserved even as both slit widths approach zero. As predicted in the previous section, the effect of the smaller slits is to shift the resonance frequency closer to f_c, increase the quality factor, and decrease the off-resonance transmission.

However, if only one slit is made smaller while the other is maintained at $\Delta_1 = 0.1d$, the peak resonant transmission decreases rapidly, in this case to only 0.6% when $\Delta_2 = 0.03d$. Evidently, the non-equal slit widths prevent achieving a perfect impedance match.

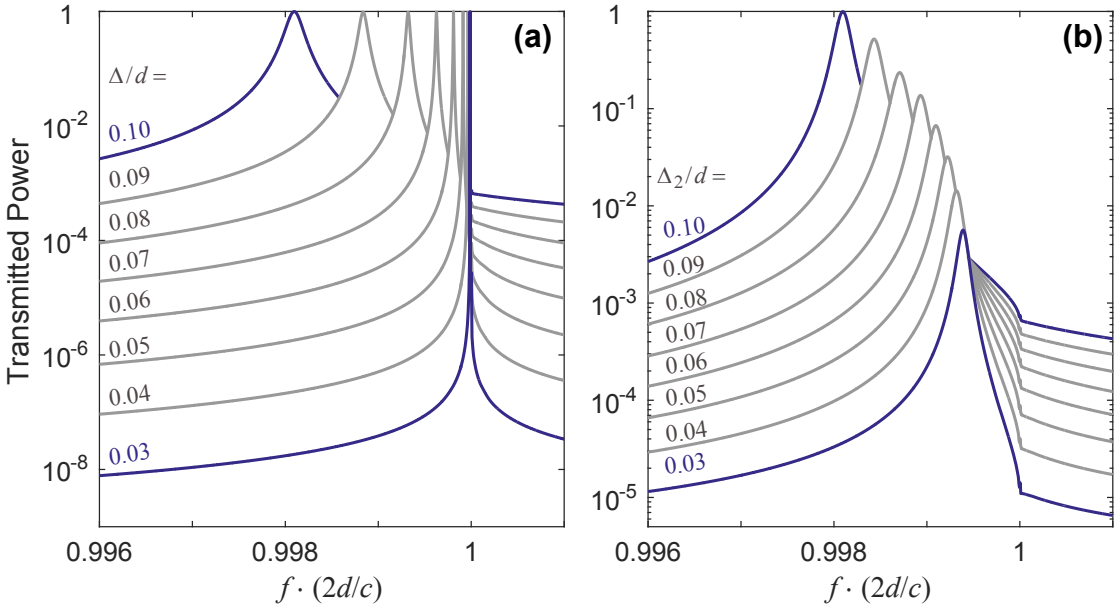

Figure 2.7: (a) TE transmitted power spectrum through two identical parallel slotted screens separated by distance d with varying $\Delta_1 = \Delta_2 = \Delta$. (b) TE transmitted power spectrum through two parallel slotted screens separated by distance d with $\Delta_1 = 0.1d$ and varying Δ_2.

2.2.4 Two Slits, TM Case

Considering the focused incident TM field of eq. 2.22, we will perform a one mode expansion in each slit with $\boldsymbol{M_q} = V_{q3}\boldsymbol{M_{q3}}$. The generalized admittance parameters for the two-slit problem of figure 2.1 with TM polarization were derived by Leviatan [29]. With some slight notation modifications and using the $e^{-i\omega t}$ time evolution convention, they are:

$$Y_{11}^{a3} \simeq \frac{\pi^2 k_a}{2\eta_a} + i\frac{k_a\pi}{\eta_a}\ln\left(\frac{\gamma k_a \Delta_1}{4}\right) \tag{2.40a}$$

$$\begin{aligned} Y_{11}^{b3} \simeq & \frac{\pi^2 k_b}{2\eta_b} + i\frac{k_b\pi}{\eta_b}\ln\left(\frac{\gamma k_b \Delta_1}{4}\right) \\ & + \frac{k_b}{\eta_b}\sum_{n=1}^{N_1}\int_{-\Delta_1}^{\Delta_1}\int_{-\Delta_1}^{\Delta_1}\frac{1}{\sqrt{\Delta_1^2 - x^2}}\frac{1}{\sqrt{\Delta_1^2 - x'^2}}H_0^{(1)}(k_b\sqrt{(x-x')^2 + (2nd)^2})\,\mathrm{d}x'\,\mathrm{d}x \\ & + \sum_{n=N_1+1}^{\infty}\frac{k_b\pi^2}{\eta_b}H_0^{(1)}(2k_b nd) \end{aligned} \tag{2.40b}$$

$$\begin{aligned} Y_{12}^{b3} \simeq & -\frac{k_b}{\eta_b}\sum_{n=1}^{N_{12}}\int_{-\Delta_1}^{\Delta_1}\int_{s_2-\Delta_2}^{s_2+\Delta_2}\frac{1}{\sqrt{\Delta_1^2 - x^2}}\frac{1}{\sqrt{\Delta_2^2 - (x'-s_2)^2}} \\ & \qquad \times H_0^{(1)}(k_b\sqrt{(x-x')^2 + [(2n-1)d]^2})\,\mathrm{d}x'\,\mathrm{d}x \\ & - \frac{k_b\pi^2}{\eta_b}\sum_{n=N_{12}+1}^{\infty}H_0^{(1)}(k_b\sqrt{s_2^2 + [(2n-1)d]^2}) \end{aligned} \tag{2.40c}$$

$$Y_{21}^{b3} = Y_{12}^{b3} \qquad \text{(reciprocity)} \tag{2.40d}$$

$$\begin{aligned} Y_{22}^{b3} \simeq & \frac{\pi^2 k_b}{2\eta_b} + i\frac{k_b\pi}{\eta_b}\ln\left(\frac{\gamma k_b \Delta_2}{4}\right) \\ & + \frac{k_b}{\eta_b}\sum_{n=1}^{N_1}\int_{-\Delta_2}^{\Delta_2}\int_{-\Delta_2}^{\Delta_2}\frac{1}{\sqrt{\Delta_2^2 - x^2}}\frac{1}{\sqrt{\Delta_2^2 - x'^2}}H_0^{(1)}(k_b\sqrt{(x-x')^2 + (2nd)^2})\,\mathrm{d}x'\,\mathrm{d}x \\ & + \sum_{n=N_1+1}^{\infty}\frac{k_b\pi^2}{\eta_b}H_0^{(1)}(2k_b nd) \end{aligned} \tag{2.40e}$$

$$Y_{22}^{c3} \simeq \frac{\pi^2 k_c}{2\eta_c} + i\frac{k_c\pi}{\eta_c}\ln\left(\frac{\gamma k_c \Delta_2}{4}\right) \tag{2.40f}$$

In eq. 2.40, $\gamma = 1.7810724\ldots$ is the exponential of the Euler-Mascheroni constant.

Using the same approach as in the TE case, the generalized TM input admittance, trans-

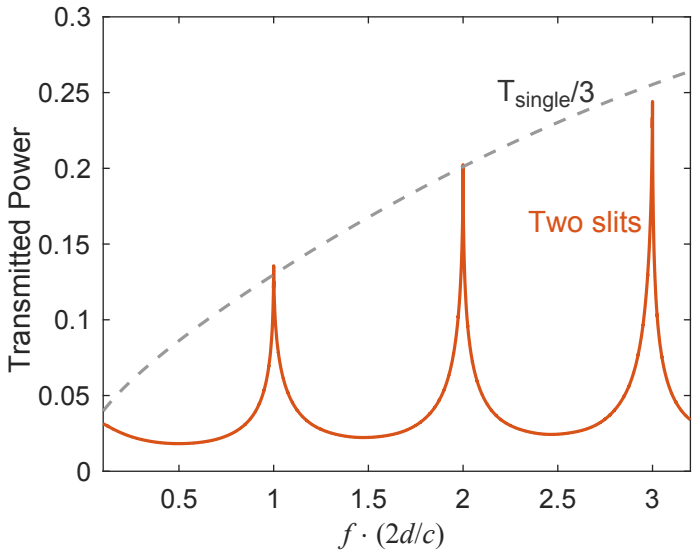

Figure 2.8: TM transmitted power spectrum through the two parallel slotted screens separated by distance d with $\Delta_1 = \Delta_2 = 0.1d$ (solid red line), including the first three peaks. For comparison, the dashed gray line shows $1/3$rd the TM transmission through a single screen with the same slit dimension.

admittance, and transmitted power into region C are:

$$Y_{11}^{\text{TM}} = \frac{I_1^{a3}}{V_{11}} = \frac{(Y_{11}^{a3} + Y_{11}^{b3})(Y_{22}^{b3} + Y_{22}^{c3}) - Y_{12}^{b3}Y_{21}^{b3}}{(Y_{22}^{b3} + Y_{22}^{c3})} \tag{2.41a}$$

$$Y_{12}^{\text{TM}} = \frac{I_1^{a3}}{V_{21}} = \frac{(Y_{11}^{a3} + Y_{11}^{b3})(Y_{22}^{b3} + Y_{22}^{c3}) - Y_{12}^{b3}Y_{21}^{b3}}{-Y_{21}^{b3}} \tag{2.41b}$$

$$P_{trans} = \frac{1}{2}\left|\frac{I_1^{a3}}{Y_{12}^{\text{TM}}}\right|^2 \text{Re}\left\{Y_{22}^{c3}\right\} \tag{2.42}$$

With the TM excitation and corresponding I_1^a given in eqs. 2.22 and 2.26, the TM transmission is:

$$T = \frac{P_{trans}}{P_{inc}} = \frac{2\pi^2 k_a}{\eta_a}\left|\frac{1}{Y_{12}^{\text{TM}}}\right|^2 \text{Re}\{Y_{22}^{c3}\} \tag{2.43}$$

Figure 2.8 shows the TM transmitted power spectrum with $\Delta_1 = \Delta_2 = 0.1d$, including the first three resonant peaks. In contrast to the TE case, the TM case never exhibits perfect transmission, and in fact never has greater transmission than in the corresponding one-slit problem. The TM spectrum does show peaks of enhanced transmission occurring at exactly the Fabry-Pérot–like frequencies, $f_{c,m} = mc/2d$. As in the TE case, the transmission through two slits at the Fabry-Pérot frequencies is the same order as the transmission through a single slit, in this case $T \simeq T_{\text{single}}/3$. Interestingly, the TM transmission peaks

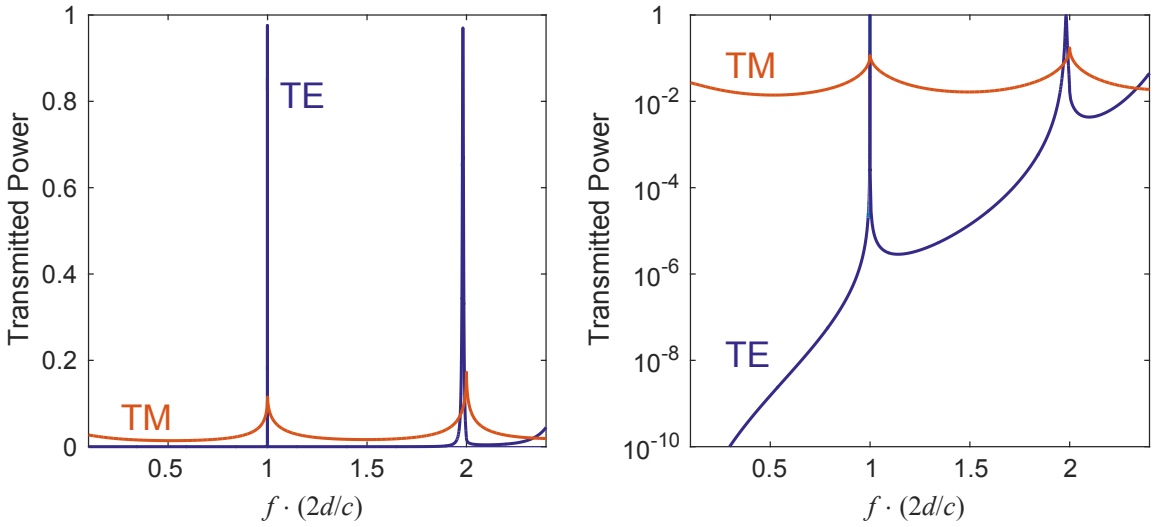

Figure 2.9: TE (blue) and TM (red) transmitted power spectrum through the two parallel slotted screens separated by distance d with $\Delta_1 = \Delta_2 = 0.08d$ (solid red line). [Left] Linear scale. [Right] Logarithmic scale.

do not have smooth Lorentzian shapes, but rather have sharp cusps at each peak, associated with the onset of a new band of TM waveguide modes.

2.2.5 Comparison and Discussion

Figure 2.9 compares the two-slit transmission spectra for TE and TM excitations with perfectly conducting, infinitesimally thin walls. The off resonant transmission is much greater with TM excitation, but the TE excitation produces sharp peaks of nearly perfect transmission at frequencies just below the Fabry-Pérot–like frequencies, $f_{c,m} = mc/2d$. As we have seen, the reason for this difference is that the TE excitation couples to a long-lived, localized resonant state associated with interactions between the slits. While there are Fabry-Pérot resonances in the TM case, they are not localized and thus cannot produce perfect transmission features.

One way to understand the resonance localization is in terms of the continuum of waveguide modes that can exist between parallel unslotted plates. The TE modes all have cutoff frequencies, below which the guided modes decay exponentially with distance. Since the TE slit-bound resonance frequency is below the lowest waveguide cutoff, it cannot exchange energy with the waveguide modes and remains localized. On the other hand, the lowest order TM waveguide mode has no cutoff frequency. Thus, there is no barrier to energy propagating away from the slits in the TM case.

2.3 Numeric Transmission Calculation

To explore the properties of the localized TE mode in the presence of thick, possibly imperfectly-conducting walls, we used a commercially available finite-element solver (COMSOL Multiphysics 3.5) to solve the two-dimensional (2d) Helmholtz equation:

$$\nabla^2 E_y + \epsilon_r k_0^2 E_y = 0$$

for the geometry shown in Figure 2.10. To reduce the size of the numerical problem and more closely correspond to our experiment, we replaced the half-space regions A and C with rectangular waveguides excited in the TE_{10} mode; this produces a confined incident field at the first slit that is similar to a diffraction-limited focus and results in nearly the same calculated transmission. We modeled the conducting walls as either perfect conductors ($E_y = 0$) or using the impedance boundary condition:

$$\hat{\boldsymbol{n}} \times \boldsymbol{H} + \sqrt{\frac{\epsilon_0 \epsilon_{r,wall}}{\mu_0}} E_y \hat{\boldsymbol{y}} = 0 \tag{2.44}$$

with the permittivity given by $\epsilon_{r,wall} = 1 + i\sigma/2\pi f\epsilon_0$, where σ is the conductivity and f a frequency in the microwave regime. Finally, we found that the infinite extent in the $\pm\hat{x}$ directions was best approximated by truncating the walls after several decay lengths of the localized mode and using COMSOL's "Port" boundary condition set for the TE_{10} mode.

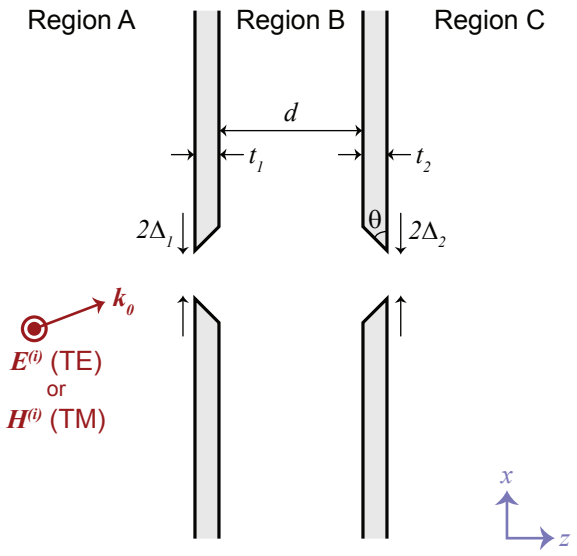

Figure 2.10: Schematic of the two-slit structure with thick walls. The conducting walls extend infinitely in the $\hat{x}$ and $\hat{y}$ directions.

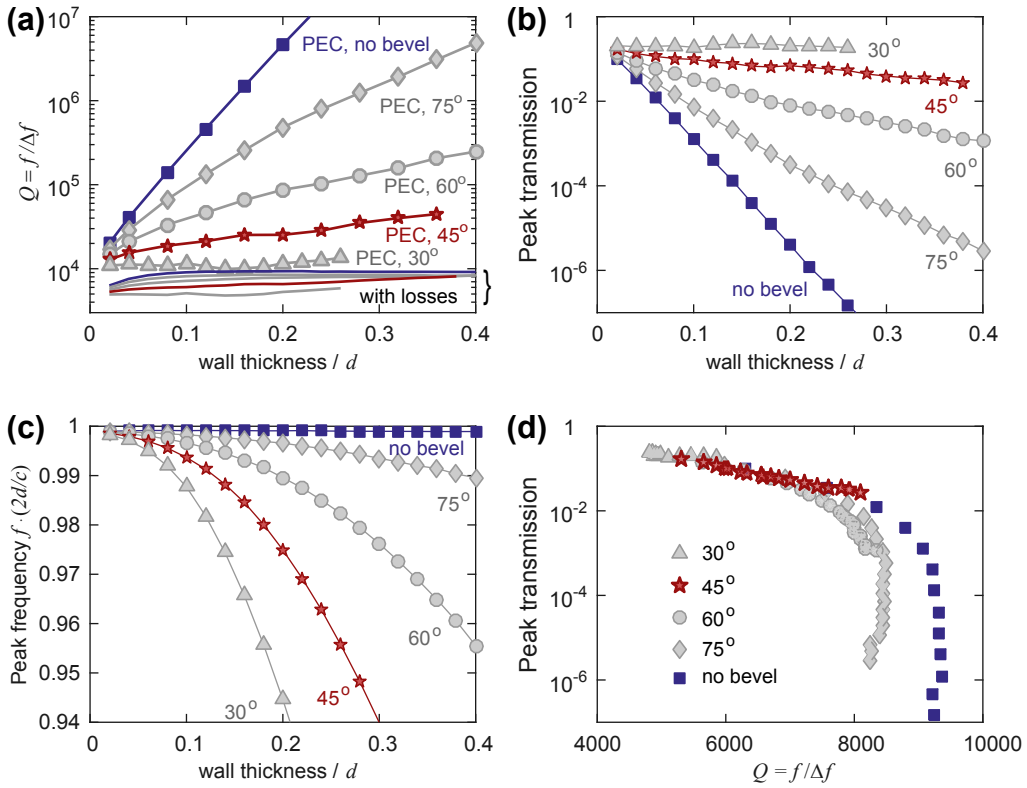

Figure 2.11: Summary of numerical TE transmission calculations with $\Delta_1 = \Delta_2 = d/10$, $\epsilon = 1$, $s_2 = 0$, and various bevel angles. (a) Quality factor (i.e., inverse bandwidth) versus thickness for perfect conductors (marked with shapes) and considering losses (no shapes). (b) Maximum transmission coefficient versus wall thickness when losses are considered. (c) Effect of wall thickness on the frequency of peak transmission. This relation is the same for real metals and perfect conductors. (d) The relation between transmission coefficient and quality factor, considering losses, is the same for a variety of wall thicknesses and bevel angles.

The transmission spectra obtained using the finite element method agree quantitatively with the analytic results of the previous section when perfectly conducting walls are used, and they agree qualitatively when conduction losses are introduced. Figure 2.11 shows the results of numerical sensitivity studies for various parameters including the wall thickness t and slit bevel angle θ. The results marked "with losses" assumed a wall conductivity of $\sigma = 3.5 \times 10^7$ S/m, representative of pure aluminum at microwave frequencies [69].

The numerical results highlight that the nonradiative conduction losses matter greatly in a practical device and put an upper limit on the achievable quality factor. Using the relation for the overall quality factor $1/Q = 1/Q_r + 1/Q_{nr}$, we can conclude that $Q_{nr} \simeq 10^4$ when realistic losses are included at microwave frequencies. Increasing the radiative quality factor Q_r much beyond this nonradiative value will serve mostly to decrease the resonant

transmission according to $T \sim Q_r^{-1}/(Q_r^{-1} + Q_{nr}^{-1})$ without appreciably narrowing the peak width. As seen in the figure, decreasing the slit width with thick walls rapidly increases Q_r beyond the useful range, and also requires tight manufacturing tolerances to make a repeatable device. This situation can be ameliorated by making a bevel in each slit to deliberately lower Q_r. Numerical studies such as those shown in figure 2.11 can be used to optimize transmission and frequency resolution for a given application.

2.4 Experiment

We have built and tested a two-slit structure that operates in the X-band microwave at 10 GHz, shown in Figure 2.12(a). The two slits are fed by commercially available rectangular WR90 waveguides, which operate in the TE_{10} mode between 8.2 and 12.4 GHz. The region between the slits is milled from two pieces of stress-relieved Alloy 6061 aluminum, with polished inner surfaces. When assembled, the structure resembles a cavity with two open ends. Compared to the ideal 2d models discussed earlier, the physical structure has additional ground planes at $y = 0$ and $y = h$ to accomodate the rectangular waveguide. Since the ground planes are perpendicular to the expected electric field, they are not expected to significantly perturb the field. They do, however, carry induced surface currents that lead to additional conduction losses. From symmetry considerations, we expect negligible current flow across the joint between the cavity halves. Table 2.1 summarizes the structure's dimensions as measured after fabrication. The dimensions were chosen for ease of manufacturing while providing reasonable expected power transmission and quality factor based on the simulation results in Figure 2.11.

Figure 2.12(b) shows the $|S_{21}|^2$ power transmission coefficient through the two slits as measured using a network analyzer. The measured transmission agrees well with a three-dimensional finite element calculation that accounts for finite conductivity of the walls and additional ground planes. We used the as-built dimensions and used the conductivity of the aluminum as a fitting parameter, obtaining the best fit for $\sigma = 1.2 \times 10^7$ S/m, which is consistent with other microwave conductivity measurements [69]. The effect of conduction losses is significant even at microwave frequencies: our device has a peak transmission that is nearly two orders of magnitude lower than the ideal, perfectly conducting case. On the other hand, we observe a resonant enhancement of approximately four orders of magnitude compared to the off-resonant transmission, with good signal-to-noise ratio.

The measured transmission spectrum exhibits ripples above the cutoff frequency $f_c = c/2d$ because the walls do not extend infinitely away from the slits in the $\pm\hat{x}$ directions but instead end after about five wavelengths. Thus, additional weak transmission peaks

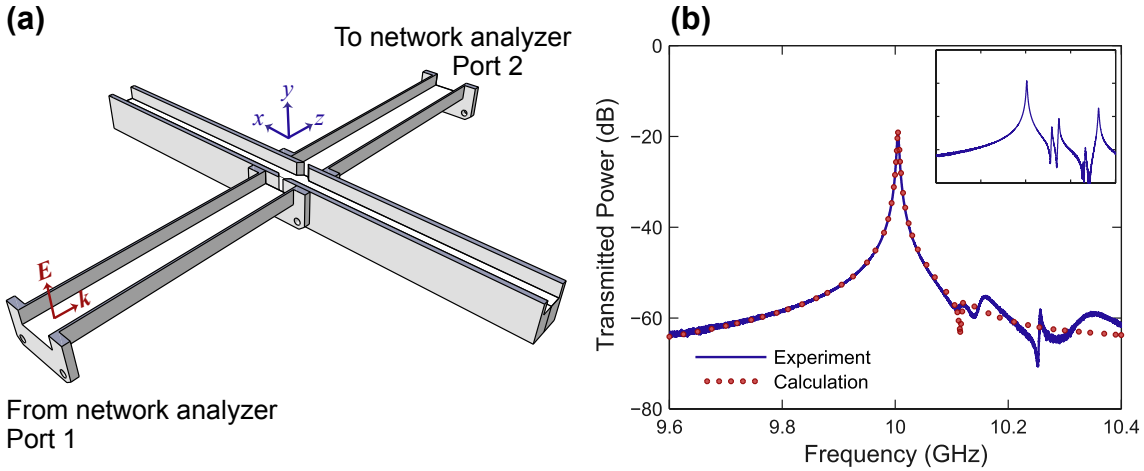

Figure 2.12: (a) Drawing of the aluminum cavity and waveguides used in the experiment. For clarity, the upper ground plane at $y = h$ is not shown. (b) Measured (blue line) and calculated (red dots) power transmission coefficient from port 1 to port 2. (inset) Measured transmission when the open cavity ends are covered with conducting plates.

Table 2.1: As-built parameters of the two-slit cavity used in the experiment.

Wall separation	d	14.8 mm
Slit 1 width	$2\Delta_1$	2.92 mm
Slit 2 width	$2\Delta_2$	3.07 mm
Wall 1 thickness	t_1	2.01 mm
Wall 2 thickness	t_2	2.01 mm
Slit bevel	θ	45^o
Height in $\hat{y}$-direction	h	10.2 mm
Length in $\hat{x}$-direction	L	305 mm
Design operating wavelength	λ_0	30 mm
Design operating frequency		10 GHz
Measured peak frequency	f_0	10.004 GHz
Measured quality factor	$Q = f_0/\delta f$	∼2760
Wall conductivity[a]	σ	1.2×10^7 S/m

[a]Calculated from fit of measured transmission spectrum

emerge due to propagating waveguide modes partially reflecting from the waveguide/free-space interface. If we simply cover the open ends with conducting plates, the main peak is unchanged but the additional peaks become much stronger (Figure 2.12(b) inset) and can be assigned to conventional cavity modes. The Fano-like [40] shape of the additional peaks suggests interference between these cavity modes and the slit-bound mode [45].

2.5 Conclusions

In conclusion, we have demonstrated resonantly enhanced transmission associated with a localized mode bound to two narrow slits in an open structure. The effect is reminiscent of the coupling to Fabry-Pérot–like modes in open cavity devices such as masers and lasers, with the crucial difference that the apertures in our case are essential for the existence of the resonance as opposed to merely serving as a means to couple to an existing cavity mode. One consequence of the slit-bound mode is elimination of the diffraction losses usually associated with open, flat-walled cavities [70].

Although our experimental demonstration was performed in the X-band microwave, the results are applicable in other frequency regimes as well, provided conductors can be found with sufficiently low losses. Subsequent to this work, a tunable frequency filter based on the two-slit resonance was demonstrated in the 0.1 - 10 THz range [68]. Materials with a plasmonic response won't affect coupling to the resonance studied here, because surface plasmon polaritons couple only to p-polarized light, whereas the two-slit resonance couples to s-polarized incident light.

The open-ended structure, with its narrow transmission peak, holds promise for applications in spectroscopy and characterization of free-flowing fluids and gases.

CHAPTER 3

A Transmission Filter Based on a Dielectric Grating

[1] As seen in the previous chapter, the quality factor and peak resonant transmission of the two-slit structure were substantially decreased by metallic absorption losses. If greater resonant transmission is desired, it is natural to look for resonant phenomena in transparent dielectric structures, which typically have lower material absorption than metals. In this chapter, we'll focus our attention on periodic dielectric structures, known as photonic crystals. These periodic structures possess band structures that can be exploited to engineer the electromagnetic response of a given system, and are analogous to the electronic bands of crystalline materials [38, 39]. With advances in fabrication techniques and computational power, photonic crystals have attracted increasing interest over the past three decades, enabling studies of many interesting physical phenomena and finding numerous applications (for a review, see [14]).

As we are interested in resonant phenomena, we will focus on a specific class of photonic crystals called photonic crystal slabs [15, 71, 72]. These slabs (or gratings) have their periodicity confined to a thin layer that is surrounded by a low-index material; consequently they have bands that extend into the light cone and can exchange energy with the radiative continuum [73]. These so-called 'leaky' modes are resonant states that can be excited by incident plane waves to produce Fano lineshapes [15, 40, 43, 47] and similarly decay into the continuum when the excitation source is removed. The lifetime of an excited mode and its associated coupling strength to the continuum is largely determined by the mutual symmetry of the mode and permissible outgoing waves [73]. Select modes possess infinite lifetimes at zone center as a result of their symmetry mismatch with allowed radiation modes [74, 75]. These symmetry-protected modes have recently been used to demonstrate high quality factor resonances near normal incidence [20, 76, 77].

[1] Portions of this chapter were originally published in [20] (©2013 AIP Publishing LLC) and [21] (©2014 American Physical Society). Reused here with permission.

Numerous optical elements have been proposed based on resonant coupling to leaky modes, starting with Magnusson *et al.* [15]. Frequency filters based on the principle have predominantly operated in a reflective geometry (or as notch filters in transmission) [78–80], which is understandable given that the dielectric material is transparent off-resonance; as discussed in chapter 1, a single resonance with a transparent background will produce a spectrum with a narrow peak of high reflectance. A dielectric transmission filter requires the incident light to interact with two resonances of similar frequency and different coupling strength: the strongly coupled mode produces a broad reflectance resonance, and Fano interference with the weakly coupled mode produces a narrow transmission peak within this high reflectance background. Previous theoretical proposals have achieved this overlapping of strong and weak resonances by coupling modes of different diffractive orders [51]; using asymmetric grating structures [81]; combining multiple adjacent gratings [49, 50]; forming a Fabry-Pérot cavity with parallel gratings [82, 83] or a grating and Bragg reflector [37]; or coupling gratings with quarter-wave reflector systems [52, 84, 85]. While a few transmission filter designs have been experimentally validated [52, 86–88], experimental demonstrations of multilayer narrowband transmission filters have generally been rare, perhaps due to the involved fabrication required.

We have experimentally demonstrated a narrowband transmission filter based on a simple, single-layer, one dimensional dielectric grating that operates in the infrared spectrum (7-14 μm) [20, 21, 89]. In this chapter, after briefly reviewing how leaky modes arise in dielectric slabs, we will analyze the particular resonant states that arise in our single-layer structure. We will show using basic group theory how certain modes are prevented by their symmetry from coupling to normally-incident light, and show how we can exploit this symmetry protection to make a narrowband reflection filter with a broad rejection band. Finally, we will discuss an experimental demonstration in the infrared.

3.1 System description

Figure 3.1 shows a schematic of the investigated grating and defines the coordinate system. The grating is defined by its relative permittivity (ϵ_g), period (Λ), thickness (t), and fill factor (FF, defined as the ratio of the grating width to the grating period, w/Λ), as well as the surrounding material's relative permittivity (ϵ_s). The materials are also assumed to be non-magnetic, $\mu_g = \mu_s = 1$. We consider plane waves with the electric field perpendicular to the y-axis ($\boldsymbol{E_{xz}}$, green-dotted plane) and the magnetic field perpendicular to the x-axis ($\boldsymbol{H_{yz}}$, red-dashed plane) with a plane wave's incidence defined by its angle with respect to the normal in the xz-plane (θ) and yz-plane (φ). The grating's periodicity in the x-

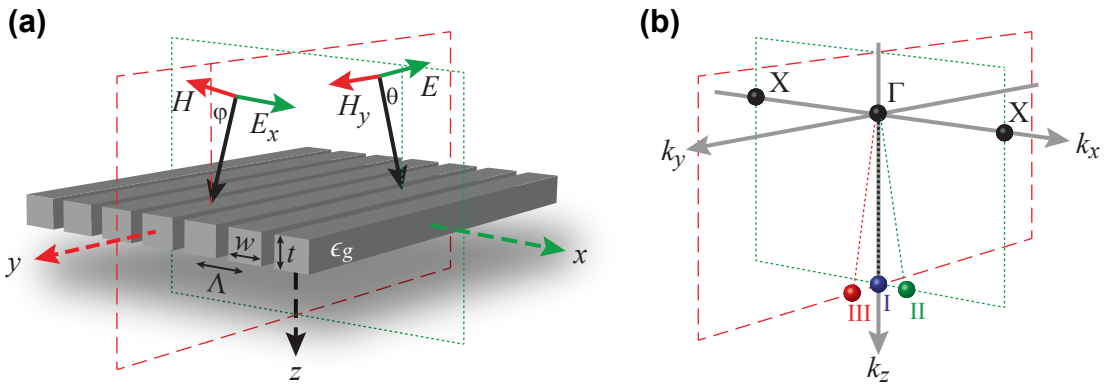

Figure 3.1: Grating schematic and its corresponding Brillouin zone with incident fields, dimensions, and material properties defined. a) The grating includes its period (Λ), height (t), width (w, defined as $\Lambda \times FF$ where FF is the fill factor) and material permittivities for the grating (ϵ_g) and surrounding material (ϵ_s). The electric field lies parallel to the xz-plane and the magnetic field lies parallel to the yz-plane. The angles with respect to normal are θ and φ, which lie in the xz- and yz-planes, respectively. b) Brillouin zone of the grating structure with analyzed incident wave vectors: Point I: normal incidence or $\theta = \varphi = 0°$ ($k_x = k_y = 0, |k_z| > 0$), Point II: $\theta > 0°$ ($|k_x|, |k_z| > 0$, $k_y = 0$), and Point III: $\varphi > 0°$ ($k_x = 0$, and$|k_y|, |k_z| > 0$).

direction limits the extent of the first Brillouin zone in the k_x direction while k_y and k_z remain unbounded. (Note that, strictly speaking, k_z is not a good quantum number, as the system lacks translation symmetry in the z-direction. We refer here to the far-field (plane-wave) wavevector of incident or radiated fields associated with the resonant modes, defined by $k_z^2 = \omega^2/c^2 - k_x^2 - k_y^2$.)

This structure is part of a particular class of one-dimensional photonic crystal slabs, often called high contrast gratings, that have attracted considerable interest for their spectral engineering capabilities including ultra-broadband reflectors [16, 37, 90], two-dimensional lenses [91, 92], and frequency filters [15, 20, 50, 51, 79, 80, 86]. Recently, one such structure, designed as a broadband reflector for visible light, showed anomalous dips in reflectivity when using high numerical aperture lenses [90]. At the time, the dips were attributed to a depolarization of the incident electric field. In fact, as we'll show in this chapter, the dips were caused by coupling to resonant guided modes in the grating that are prevented by their symmetry from coupling to normally incident light, but can couple weakly at slightly oblique incidence.

Analyzing the symmetry of the grating's supported modes can help us selectively couple to particular sets of modes, producing narrowband transmission filters. We will discuss mode coupling at several incidence angles, defined by coordinates in reciprocal space: nor-

mal incidence Point I ($|k_z| > 0$, $\theta = \varphi = 0°$); and off-normal incidence in the xz- and yz-planes, Point II ($|k_z|, |k_x| > 0$, $\theta > 0°$) and Point III ($|k_z|$,$|k_y| > 0$, $\varphi = 0°$), respectively.

3.2 Origin of leaky modes

3.2.1 Guided modes in a uniform dielectric slab

To begin, let us review the textbook problem of guided modes in a uniform dielectric slab (c.f. [1, 63, 73]). Figure 3.2 shows the slab geometry. If the refractive index within the slab is greater than in the surrounding material, confined modes can exist due to total internal reflection. In this section, we will derive the dispersion relation between the tangential wavevector and mode frequencies, which will be useful later.

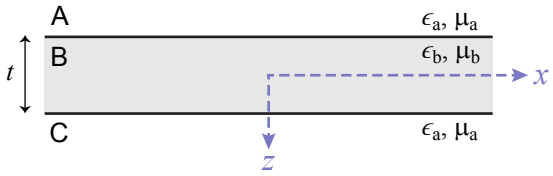

Figure 3.2: Geometry of a uniform dielectric slab supporting guided modes propagating along the x-axis.

Given the symmetry of the structure, the characteristic solutions can be classified as either odd or even with respect to reflection across the $z = 0$ plane. Without loss of generality, we can consider wave propagation solely in the $\pm x$ direction, with no field variation in the $\pm y$ direction, in which case the solutions are either transverse magnetic (TM), with magnetic field in the y direction, or transverse electric (TE), with electric field

in the y direction. The fields for odd TM guided modes have the form:

$$\text{Region A} \begin{cases} H_{ay} = -iA\omega\epsilon_a\nu e^{\nu z}e^{ik_x x} \\ E_{ax} = A\nu^2 e^{\nu z}e^{ik_x x} \\ E_{az} = -iAk_x\nu e^{\nu z}e^{ik_x x} \end{cases} \quad z < -\frac{t}{2} \tag{3.1a}$$

$$\text{Region B} \begin{cases} H_{by} = iB\omega\epsilon_b k_{bz}\cos(k_{bz}z)e^{ik_x x} \\ E_{bx} = Bk_{bz}^2\sin(k_{bz}z)e^{ik_x x} \\ E_{bz} = -iBk_x k_{bz}\cos(k_{bz}z)e^{ik_x x} \end{cases} \quad |z| \le \frac{t}{2} \tag{3.1b}$$

$$\text{Region C} \begin{cases} H_{cy} = -iA\omega\epsilon_a\nu e^{-\nu z}e^{ik_x x} \\ E_{cx} = -A\nu^2 e^{-\nu z}e^{ik_x x} \\ E_{cz} = iAk_x\nu e^{-\nu z}e^{ik_x x} \end{cases} \quad z > \frac{t}{2} \tag{3.1c}$$

Here, the wave guidance is chosen to be solely in the $\pm z$ direction, so $k_{\ell y} = 0$ in each region ℓ, and $k_{az} = k_{bz} = i\nu$ so that the fields decay evanescently away from the slab in regions A and C. Thus,

$$\begin{aligned} k_{bz}^2 &= k_b^2 - k_x^2 = \omega^2\mu_b\epsilon_b - k_x^2 \\ \nu^2 &= k_x^2 - k_a^2 = k_x^2 - \omega^2\mu_a\epsilon_a \end{aligned} \tag{3.2}$$

The phase matching condition is implicitly enforced by using the same k_x in each region. The continuity of the tangential electric and magnetic fields at $z = \pm t/2$ gives:

$$\begin{aligned} Bk_{bz}^2\sin\left(k_{bz}\frac{t}{2}\right) &= -A\nu^2 e^{-\nu t/2} \\ iB\omega\epsilon_b k_{bz}\cos\left(k_{bz}\frac{t}{2}\right) &= -iA\omega\epsilon_a\nu e^{-\nu t/2} \end{aligned}$$

Dividing the first of these equations by the second yields a relation between k_{bz} and ν:

$$k_{bz}\tan\left(k_{bz}\frac{t}{2}\right) = \frac{\epsilon_b}{\epsilon_a}\nu \qquad \text{(odd TM modes)} \tag{3.3}$$

Furthermore, adding the equations in (3.2) yields:

$$k_{bz}^2 + \nu^2 = \omega^2(\mu_b\epsilon_b - \mu_a\epsilon_a) \tag{3.4}$$

Equations 3.2 and 3.4 can be solved simultaneously for a given frequency ω to give the wavevectors k_{bz}, ν, and thus k_x.

Solutions for even TM guided modes can be found using a procedure similar to the

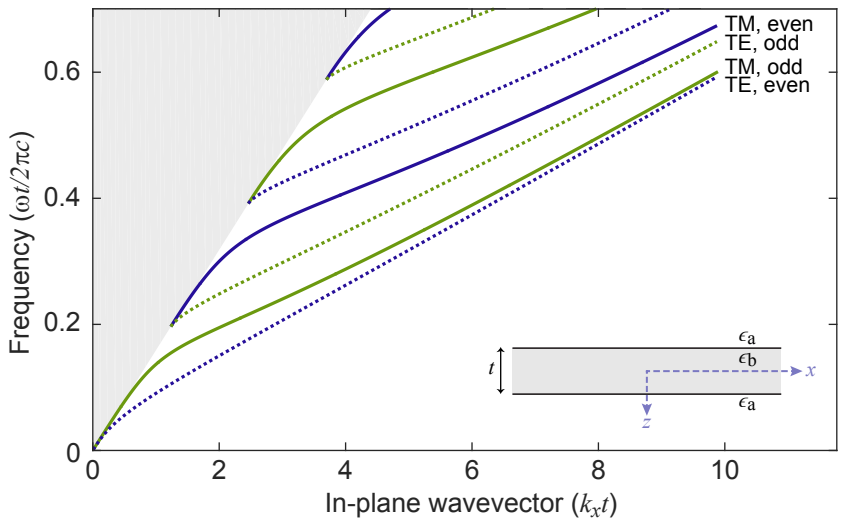

Figure 3.3: Dispersion relations of guided modes in a dielectric slab of permittivity $\epsilon_b = 7.52$ surrounded by vacuum. The frequency ω and in-plane wavevector k_x are normalized to the slab thickness t. Modes are classified by polarization (TM solid lines and TE dotted lines) and parity with respect to reflection of the in-plane electric field across the $z = 0$ plane ($\hat{\sigma_z}$). Even ($\sigma_z = 1$) modes are blue and odd ($\sigma_z = -1$) modes are green. The light cone is shown in light gray.

above, replacing $\sin()$ with $\cos()$ (and vice-versa) in eq. 3.1 and keeping track of sign changes to give fields of even parity. The dispersion relations are then found by solving eq. 3.4 simultaneously with eq. 3.5 (instead of with eq. 3.3):

$$-k_{bz} \cot\left(k_{bz}\frac{t}{2}\right) = \frac{\epsilon_b}{\epsilon_a}\nu \qquad \text{(even TM modes)} \tag{3.5}$$

Finally, the TE solutions can be found using duality relations, giving:

$$k_{bz} \tan\left(k_{bz}\frac{t}{2}\right) = \frac{\mu_b}{\mu_a}\nu \qquad \text{(even TE modes)} \tag{3.6a}$$

$$-k_{bz} \cot\left(k_{bz}\frac{t}{2}\right) = \frac{\mu_b}{\mu_a}\nu \qquad \text{(odd TE modes)} \tag{3.6b}$$

Figure 3.3 shows the guided mode dispersion relations beween the in-plane wavevector k_x and the frequency ω for a uniform non-magnetic slab with dielectric constant $\epsilon_b = 7.52$, surround by air ($\epsilon_a = 1$). This dielectric constant was chosen so that the slab would have the same average refractive index in the infrared as the high-contrast silicon grating discussed in section 3.2.3.

As seen in the figure, all the guided modes, except the lowest order odd TM and even TE modes, have a low frequency cutoff. The cut-off frequency for a given mode corresponds to

$\nu = 0$ (no decay along the x axis). That is, $\cot(k_{bz}t/2) = 0$ or $\tan(k_{bz}t/2) = 0$, depending on the mode polarization and parity. The cutoff frequencies are thus given by:

$$\omega_c^m = \frac{\pi m}{t\sqrt{\mu_b\epsilon_b - \mu_a\epsilon_a}} \qquad m = 0, 1, 2, \ldots \tag{3.7}$$

From eq. 3.2, each mode's cutoff occurs where the dispersion curve intersects the light line, $\omega = ck_x$. Continuing the dispersion curves past the light line would require an imaginary vaue for the decay constant ν, with propagating waves towards or away from the slab. Indeed, the region shaded in gray in figure 3.3, called the light cone, represents a continuum of radiative modes, corresponding to all the possible configurations of incident plane waves. In a uniform slab, the guided modes have no overlap with this continuum. They cannot exchange energy with incident light.

3.2.2 Leaky modes in a periodic dielectric slab

Patterning the slab can allow incident light to resonantly couple with the guided modes. To see how this can occur, consider the nearly-uniform slab shown in figure 3.4a. Compared to the uniform slab of figure 3.2, a periodic modulation, with period Λ, has been added to the refractive index. Considering the odd TM modes and invoking the 1d form of the Floquet/Bloch theorem [93], the periodicity of the medium lets us write the magnetic field as:

$$H_y(x, z; k_x) = u_k(x, z)e^{ik_x x} \tag{3.8}$$

where u_k has the same periodicity as the slab: $u_k(x+\Lambda, z) = u_k(x, z)$. Similar expressions apply for the other field components and for the electric field. A consequence of eq. 3.8 is that values of the in-plane wavevector k_x differing only by a reciprocal lattice vector $\boldsymbol{G} = \hat{\boldsymbol{x}}2\pi m/\Lambda$ are not unique:

$$\begin{aligned} u_k(x, z)e^{i(k_x+2\pi m/\Lambda)x} =& u_k(x, z)e^{i2\pi mx/\Lambda}e^{ik_x x} \\ =& u_{mk}(x, z)e^{ik_x x} \end{aligned} \tag{3.9}$$

and u_{mk} also has the same periodicity as the slab. Thus, the dispersion relations for the guided modes can be represented in a reduced zone scheme by folding the dispersion curves into the first Brillouin zone, defined by $|k_x| \leq \pi/\Lambda$. If the slab's permittivity modulation is small, so that the dispersion curves found for the uniform slab are still approximately valid, then the result is shown in figure 3.4b. Each guided mode of the uniform slab has become several bands within the first Brillouin zone, characterized by the functions $u_{mk}(x, z)$, with

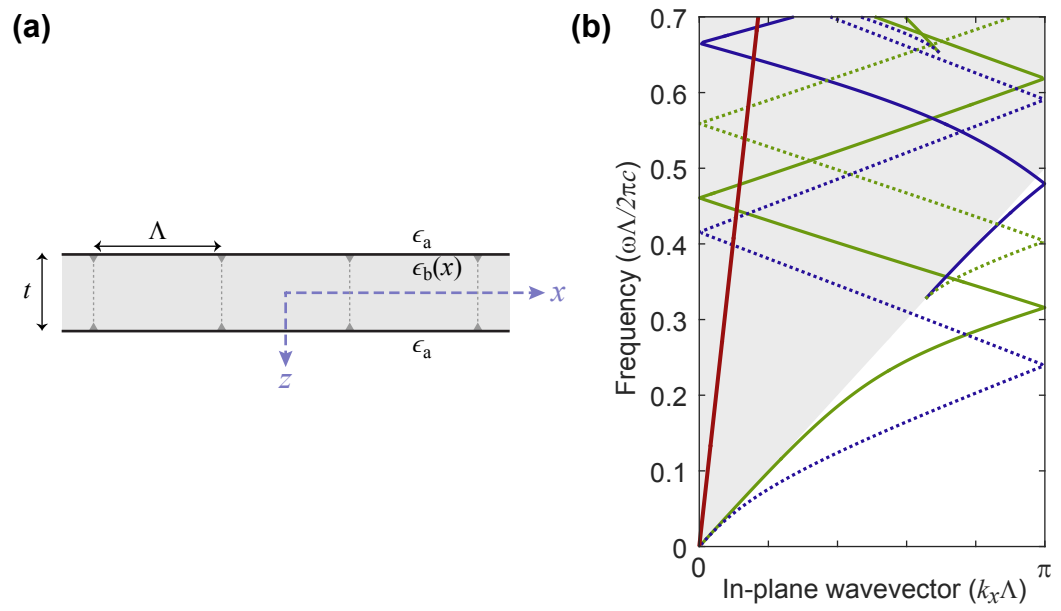

Figure 3.4: (a) Geometry of a nearly-uniform periodic dielectric slab, with thickness t and period Λ. (b) Dispersion relations of guided and leaky modes within the first Brillouin zone in a slab of permittivity $\epsilon_b = 7.52$ and thickness $t = 0.6\Lambda$ surrounded by vacuum. The frequency ω and in-plane wavevector k_x are normalized to the period Λ. Modes are classified by polarization (TM solid lines and TE dotted lines) and parity with respect to reflection of the in-plane electric field across the $z = 0$ plane ($\hat{\sigma_z}$). Even ($\sigma_z = 1$) modes are blue and odd ($\sigma_z = -1$) modes are green. The light cone is shown in light gray. A red line shows the dispersion relation of a plane wave at an incidence angle of 7°.

$m = 0, 1, 2, \ldots$.

Crucially, many of the guided modes now overlap the radiative continuum marked by the gray light cone in figure 3.4b, and could resonantly couple to incident light if the right conditions are met. Consider the diffraction of one of these modes, with wavevector k_x, into a radiative mode. From phase-matching considerations, the diffracted wave will have a wavevector given by:

$$\boldsymbol{k} = k_x\hat{\boldsymbol{x}} + \boldsymbol{G} + k_z\hat{\boldsymbol{z}} \tag{3.10}$$

where $\boldsymbol{G}$ is a reciprocal lattice vector of the grating, and k_z is determined by the region A dispersion relation,

$$k_z^2 = \frac{\omega^2}{c_a^2} - |k_x + G|^2 \tag{3.11}$$

($c_a = 1/\sqrt{\epsilon_a\mu_a}$ is the speed of light in regions A and C). For a subwavelength grating with $\omega < 2\pi c_a/\Lambda$, then for modes at the Γ point ($k_x = 0$), G must be zero to give real values of k_z, and so there is only one radiative mode into which the guided mode can couple: the normally incident wave with wavevector $\boldsymbol{k} = \hat{\boldsymbol{z}}\omega/c_a$. Similar arguments apply for other

values of k_x, with guided modes in a subwavelength grating coupling only to zero-order radiative modes with the same transverse wavevector, although the condition for being a subwavelength grating will vary somewhat with k_x.

Thus, the coupling strength between a guided mode and the radiative continuum will be given by an overlap integral over the unit cell between the u_{mk} functions corresponding to the various field components and the associated fields in the radiative mode with the same transverse wavevector. In general, coupling strength will be higher with large periodic modulations in the permittivity and with high index contrast with the surrounding medium. However, there can be modes for which the radiative coupling is zero, due to a symmetry mismatch with the radiative fields. Paddon and Young [74] identified such symmetry-protected modes with infinite lifetimes at the Γ point in a slab with a square lattice, and Ochiai and Sakoda [75] found similar modes in a hexagonal lattice. We will return to this point, in the context of our 1d high contrast grating, in section 3.3.

Finally, there is a connection between the resonant guided modes that arise in a periodic dielectric slab and the Wood anomaly [41] observed in metallic gratings with p-polarized incident light (magnetic field parallel to the grating grooves).[2] The Wood anomaly was finally explained by Fano [42] as caused by a resonance related to the "leaky waves supportable by the grating" (later identified as surface plasmon polaritons). Although the physical nature of the guided modes differs, the mechanism of coupling to incident light via the slab's periodic patterning, and the resulting effect on the spectral response, are the same. The "leaky" coinage has also proved quite popular and is commonly used in the literature to refer to resonant guided modes.

3.2.3 Numeric calculation of modes in a high contrast grating

Now, we return our attention to the high contrast slab, shown in figures 3.1 and 3.5. Here, the periodic modulation is extremely strong, with the permittivity varying from ϵ_g to ϵ_s over a single period. Consequently, the folded dispersion relations of a uniform slab cannot be expected to give accurate results for the mode frequencies. To provide a quantitative comparison with our experiment, and to facilitate the group theory analysis of section 3.3, we calculated the guided mode fields and dispersion relations for the grating using finite element methods. Our method, described in more detail in appendix B, calculates the

[2] Wood's paper is also notable for including one of the greatest methods statements in the history of science: "The study of this grating has been limited to the two or three days immediately preceding the closing of the laboratory for the summer, consequently I have been unable to give a very exhaustive account of its behaviour under other conditions, or secure any very satisfactory photographs of the peculiar spectra. The few photographs which I have taken and which are reproduced, were made on some old orthochromatic plates, without any especial appliances..."

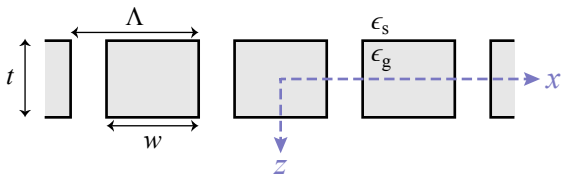

Figure 3.5: Geometry of a high-contrast periodic dielectric slab, with thickness t and period Λ. Each period consists of a dielectric region of width w and permittivity ϵ_g, followed by a gap with the same permittivity as the surrounding material ϵ_s.

complex propagation constant using a weak formulation of Helmholtz' equation expressed as a quadratic eigenvalue problem [94, 95].

Figure 3.6 shows the resulting dispersion relations for TM polarized guided modes and the associated field profiles for several resonances for a grating with: $\frac{t}{\Lambda} = 0.6$, $FF = 0.72$, $\epsilon_g = 11.7$, and $\epsilon_s = 1$. The dispersion relations show the guided modes, with solid bands representing modes that were calculated using the modal analysis. The dashed bands, in contrast, were estimated from scattering analysis due to their imaginary propagation constants being larger than the Brillouin zone, which makes them difficult to accurately calculate. Because of the grating periodicity in one direction, the dispersion relations are represented in a reduced zone scheme. As seen in the figure, the index contrast between the grating and surrounding material lifts the degeneracies at the zone boundaries ($k_x = \frac{\pi}{2}$) and zone center ($\boldsymbol{k} = 0$). The modes at zone center ($\boldsymbol{k} = 0$) are labeled with their irreducible representations in the D_{2h} point group of the slab, determined by using a reduction procedure [73] and by applying the symmetry operations of the point group to the the simulated mode field profiles. Looking at the E_x field profile for the lowest two zone center modes, TM_1^- and TM_1^+, it is clear that these modes have very different symmetry and are expected to have very different coupling to normally incident light. TM_1^+ presents a nearly uniform tangential electric field at each surface, matching well to an incident plane wave. TM_1^-, on the other hand, will not couple to a normally incident plane wave at all. These arguments will be formalized in the next section.

Figure 3.7 shows the calculated dispersion relations and field profiles for TE polarized guided modes. As for the TM case, the modes are labeled at zone center with their irreducible representations in the D_{2h} point group.

3.3 Group theory analysis

The high-contrast suspended grating belongs to the D_{2h} point group, requiring the grating's supported modes at the Γ-point ($\boldsymbol{k} = 0$) to have the same symmetry as the point

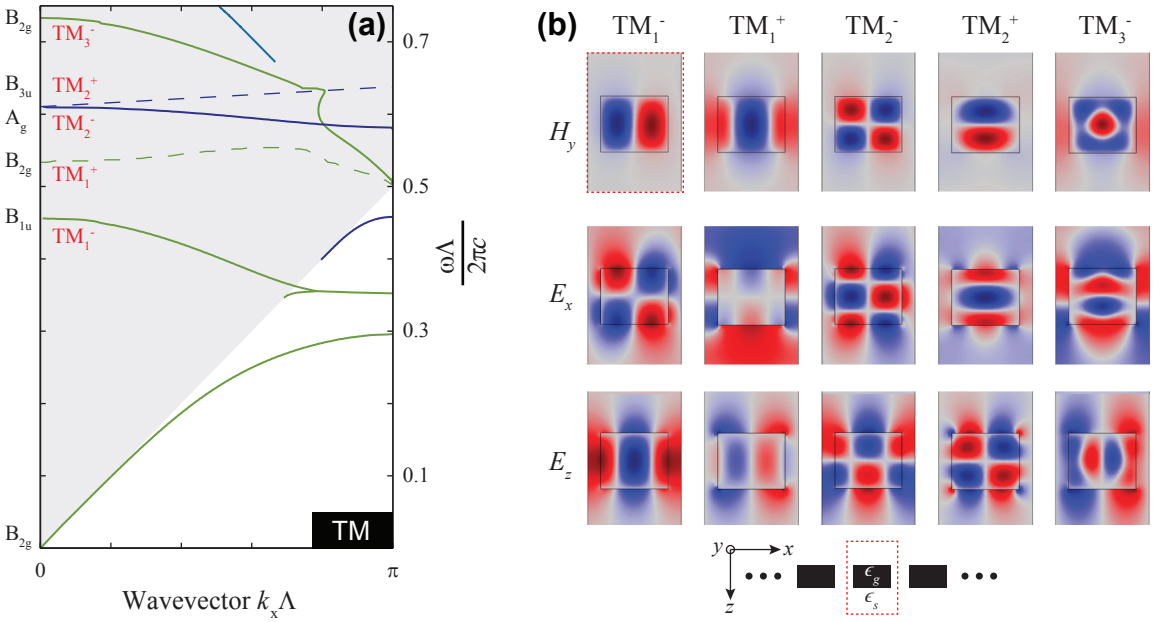

Figure 3.6: TM dispersion relations and field profiles for a grating with $\frac{t}{\Lambda} = 0.6$, $FF = 0.72$, $\epsilon_g = 11.7$, and $\epsilon_s = 1$. a) The dispersion relations include even (blue) and odd (green) bands with respect to reflection across $y = 0$. Solid bands were calculated using a finite element modal analysis and dashed bands are estimated from scattering analysis. The modes at $k_x = 0$ are labeled with their Γ-point (D_{2h} symmetry) irreducible representations and band definitions. The light cone is shown in light gray. b) TM mode field profiles at $k_x = 0$ with a black line indicating the boundary between high and low permittivities. Below: grating simulation element, and directions defined.

group's irreducible representations [73]. Table 3.1 shows the character table of the D_{2h} point group, along with some guided modes of the grating, from the modal analysis summarized in figures 3.6 and 3.7, that belong to each irreducible representation at the Γ-point. These modes, with the exception of the zero-frequency mode, lie within the light cone as a consequence of the photonic crystal's slab design. Hence, phase matching is possible between these modes and incident light. The lowest order TM leaky mode, TM_1^-, belongs to the B_{1u} irreducible representation. This mode is anti-symmetric upon rotation about the y-axis ($\hat{C}_{2y}$) and reflection across the xy-plane ($\hat{\sigma}_z$), and symmetric upon reflection across the yz-plane ($\hat{\sigma}_x$), remembering the magnetic field is a pseudo-vector. We will show that at normal incidence a TM polarized plane wave cannot excite modes of this symmetry.

A normally incident TM polarized plane wave, $|k_z| > 0$, shown as Point I in Figure 3.1b, belongs to the reduced symmetry of the C_{2v}^z point group, where the superscript z indicates the symmetric rotation axis. The symmetry operations of this group ($\hat{E}$, $\hat{C}_{2z}$, $\hat{\sigma}_y$, and $\hat{\sigma}_x$) are summarized with its irreducible representations in Table 3.2a, along with the grating modes belonging to each representation. A wave with this polarization can

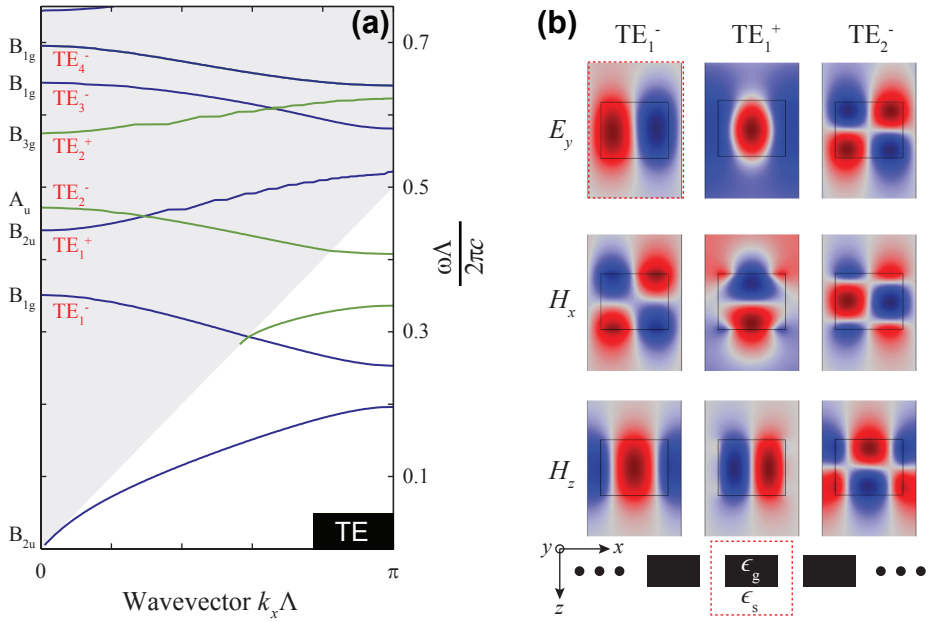

Figure 3.7: TE dispersion relations and select field profiles for a grating with $\frac{t}{\Lambda} = 0.6$, $FF = 0.72$, $\epsilon_g = 11.7$, and $\epsilon_s = 1$. a) The dispersion relations include even (blue) and odd (green) bands with respect to reflection across $y = 0$. The modes at $k_x = 0$ are labeled with their Γ-point (D_{2h} symmetry) irreducible representations and band definitions. The light cone is shown in light gray. b) TE mode field profiles at $k_x = 0$ with a black line indicating the boundary between high and low permittivities. Below: grating simulation element, and directions defined.

couple to TM (but not TE) guided modes in the grating. For this coupling to occur, the phase matching condition must be met and the overlap integral between the incident field and the supported mode must be non-zero; this requires the mode and incident wave to belong to the same irreducible representation. The compatibility relations between Point I and the Γ-point, determined by comparing the character tables for the relevant symmetry operations, give their mutual irreducible representations. These relations, summarized in Table 3.2b, show that each mode at Point I (C_{2v} point group) maps onto two modes at the Γ-point (D_{2h} point group). The incident TM plane wave of Point I belongs to the B_1 irreducible representation, which matches the symmetry of the B_{2g} and B_{3u} Γ-point irreducible representations at Point I. This plane wave, thus, can couple to modes that belong to these two irreducible representations at the Γ-point while the other modes are inaccessible or symmetry-protected, as seen in Table 3.2a; explicitly, modes TM_1^+, TM_2^+, and TM_3^- of Figure 3.6 are all accessible at normal incidence, while modes TM_1^- and TM_2^- are symmetry-protected. This symmetry matching is illustrated by the x-component of the electric field intensity shown in Figure 3.6b where modes TM_1^+, TM_2^+, and TM_3^- share plane wave symmetry in the x-direction while modes TM_1^- and TM_2^- are anti-symmetric in

Table 3.1: D_{2h} character table corresponding to the Γ-point of the grating's reciprocal lattice as well as the analyzed grating modes associated with each irreducible representation.

D_{2h}	E	C_{2z}	C_{2y}	C_{2x}	i	σ_z	σ_y	σ_x	TM Modes	TE Modes
A_g	1	1	1	1	1	1	1	1	TM_2^-	
B_{1g}	1	1	-1	-1	1	1	-1	-1		$\text{TE}_1^-, \text{TE}_3^-, \text{TE}_4^-$
B_{2g}	1	-1	1	-1	1	-1	1	-1	$\text{TM}_1^+, \text{TM}_3^-$	
B_{3g}	1	-1	-1	1	1	-1	-1	1		TE_2^+
A_u	1	1	1	1	-1	-1	-1	-1		TE_2^-
B_{1u}	1	1	-1	-1	-1	-1	1	1	TM_1^-	
B_{2u}	1	-1	1	-1	-1	1	-1	1		TE_1^+
B_{3u}	1	-1	-1	1	-1	1	1	-1	TM_2^+	

Table 3.2: a) C_{2v}^z character table and b) the compatibility relations between Point I and the Γ-point

C_{2v}^z	E	C_{2z}	σ_y	σ_x	TM Modes	TE Modes
A_1	1	1	1	1	$\text{TM}_1^-, \text{TM}_2^-$	
A_2	1	1	-1	-1		$\text{TE}_1^-, \text{TE}_2^-, \text{TE}_3^-, \text{TE}_4^-$
B_1	1	-1	1	-1	$\text{TM}_1^+, \text{TM}_2^+, \text{TM}_3^-$	
B_2	1	-1	-1	1		$\text{TE}_1^+, \text{TE}_2^+$

(a)

Point I	Γ
A_1	A_g , B_{1u}
A_2	B_{1g} , A_u
B_1	B_{2g} , B_{3u}
B_2	B_{3g} , B_{2u}

(b)

comparison.

To access the symmetry-protected modes, the incident wave vector can be moved off the k_z axis to Point II, which is maintained in the k_xk_z-plane. Point II has the further reduced symmetry of the C_s^{xz} point group, with symmetry only upon reflection across the xz-plane, $\hat{\sigma}_y$. The C_s^{xz} character table and the compatibility relations between Point II (C_s^{xz} point group) and the Γ-point (D_{2h} point group) are given in Tables 3.3a and 3.3b, along with the associated symmetries of the guided modes. This reduced symmetry relaxes the selection rules, illustrated by the mapping of four Γ-point irreducible representations onto each irreducible representation at Point II. The incident plane wave belongs to the A' irreducible representation. All the TM modes considered at Point II share this irreducible representation. Consequently, the modes that are symmetry-protected at normal incidence can now couple to this off-normal incidence plane wave.

If instead we consider a plane wave with wave vector at Point III of Figure 3.1b, we maintain symmetry across the yz-plane, $\hat{\sigma}_x$, and introduce a z-component of the magnetic

Table 3.3: a) C_s^{xz} character table and b) the compatibility relations between Point II and the Γ-point

C_s^{xz}	E	σ_y	TM Modes	TE Modes
A'	1	1	TM_1^-, TM_1^+, TM_2^-, TM_2^+, TM_3^-	
A''	1	-1		TE_1^-, TE_1^+, TE_2^-, TE_2^+, TE_3^-, TE_4^-

(a)

Point II	Γ
A'	A_g , B_{2g} , B_{1u} , B_{3u}
A''	A_u , B_{1g} , B_{3g} , B_{2u}

(b)

Table 3.4: a) C_s^{yz} character table and b) the compatibility relations between Point III and the Γ-point

C_s^{yz}	E	σ_x	TM Modes	TE Modes
A'	1	1	TM_2^-, TM_1^-	TE_1^+, TE_2^+
A''	1	-1	TM_1^+, TM_2^+, TM_3^-	TE_1^-, TE_2^-, TE_3^-, TE_4^-

(a)

Point III	Γ
A'	A_g , B_{3g} , B_{1u} , B_{2u}
A''	A_u , B_{1g} , B_{2g} , B_{3u}

(b)

field (H_z) to the plane wave. In addition to exciting TM modes, this wave can also couple to TE guided modes, provided they have the appropriate symmetry. The grating's TE dispersion relations are shown in Figure 3.7 with field profiles of select modes illustrated. The C_s^{yz} character table and the compatibility relations between Point III (C_s^{yz} point group) and the Γ-point (D_{2h} point group) are shown in Tables 3.4a and 3.4b. At Point III the incident plane wave belongs to the A'' irreducible representation of the C_s^{yz} point group, which shares the symmetry of several guided modes at Point III. Thus, coupling to TE_1^-, TE_2^-, TE_3^-, and TE_4^- is allowed while modes TE_1^+ and TE_2^+ remain symmetry-protected due to their anti-symmetry in H_y for reflections across the yz-plane. To couple to these additional modes, the x-symmetry must also be broken, which could be achieved by introducing an additional k_x component to the wave vector. A summary of the permissible mode coupling for incident plane waves with wave vectors at Points I, II, and III is given in Table 3.5.

3.4 Transmission calculations

We have exploited this selective mode coupling to realize transmission filters using a dielectric grating. The operating principle, as discussed earlier, involves coupling the incident light to two grating modes that overlap in frequency and have different coupling strengths.

Table 3.5: Summary of the allowable mode coupling for a TM polarized plane wave with various incident wave vectors. 'X' indicates relatively strong coupling, while 'o' indicates relatively weak coupling. (Note that coupling to mode TM_3^- is allowed by symmetry even at normal incidence, but is relatively weak as described in the text.)

Modes	TM_1^-	TM_1^+	TM_2^-	TM_2^+	TM_3^-	TE_1^-	TE_1^+	TE_2^-	TE_2^+	TE_3^-	TE_4^-
Point I		X		X	o						
Point II	o	X	o	X	o						
Point III		X		X	o	o		o		o	o

The strongly coupled mode produces a broad reflectance resonance, and Fano interference with the weakly coupled mode produces a narrow transmission peak within this high reflectance background. Previous proposals achieved this in various ways, including using different diffractive orders [51], using asymmetric grating structures [81], or combining a grating with additional resonant structures [37, 50, 82, 83]. In contrast to these methods, we exploit symmetry-protected modes of a single diffraction order to achieve the required coupling strength disparity.

Figure 3.8 shows the transmittance profiles in the k_x and k_y directions, or moving towards Points II and III, respectively, for the transmission filter design discussed below. The imaginary part of the propagation constant, determined from the modal analysis, represents the coupling strength to the radiation field; a large (small) value results in fast (slow) decay and consequently a broadband (narrowband) response. The width of a given resonance can be expressed by its quality factor, $Q = \omega/\delta\omega$, and is related to the energy decay within the mode given by $U(t) = U(t_0)\exp\left[-\omega(t-t_0)/Q\right]$ [73]. We iteratively optimized the grating dimensions to maximize the coupling strength to accessible TM modes at normal incidence, Point I, and consequently achieve a very low-Q response. See [89] for details of this optimization process. The structure consequently exhibits broadband reflectance greater than 95% for $0.357 < \omega\Lambda/2\pi c < 0.625$. The optimized structure dimensions are identical to those used for the dispersion relations of Figures 3.6 and 3.7: $t/\Lambda = 0.6$ and $FF = 0.72$. To facilitate the experimental demonstration discussed in the next section, we also included a substrate separated from the grating by an air layer of thickness $h/\Lambda = 0.8$, which is far enough to inhibit energy leakages from the grating. A permittivity of $\epsilon_g = 11.7$ was used for the grating and substrate, consistent with silicon at infrared frequencies [96]. At normal incidence the low transmittance background is demonstrated as a result of the optimized coupling to the TM_1^+ and TM_2^+ modes. From the group theoretical analysis we also expect coupling to mode TM_3^-. The transmission band associated with this mode exhibits a narrow transmission band response that is a result of a small overlap integral be-

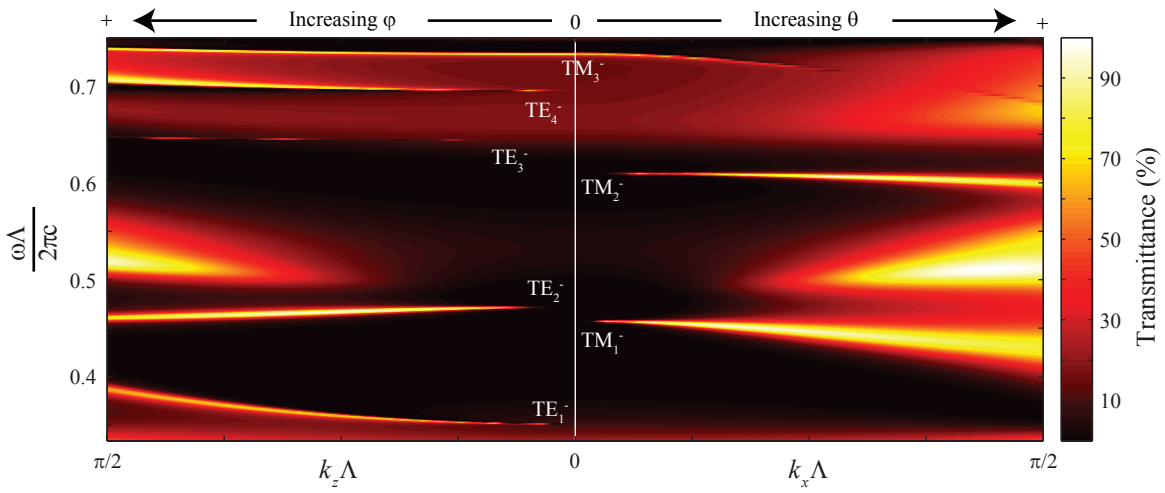

Figure 3.8: Simulated grating transmittance profile at normal and off-normal incidence. $k_x = 0$, $|k_x| > 0$, and $|k_y| > 0$ correspond to Points I, II, and III, respectively. The top scale shows increasing θ and φ directions corresponding to $|k_x| > 0$, and $|k_y| > 0$, respectively. Transmission bands are labeled with the mode associated with the resonance.

tween the incident plane wave and mode. This small overlap integral can be inferred from the multiple nodes in the field profiles compared to an incident plane wave with wavelength greater than the grating thickness.

Away from normal incidence, $|k_x| > 0$ or $|k_y| > 0$, the relaxed selection rules enable coupling to the symmetry-protected modes. The broadband low-transmittance is maintained near $k_x = k_y = 0$ since the overlap integrals with the modes responsible for the response remain nearly constant. Within this broadband background, narrow transmission bands emerge as a result of weak coupling to the symmetry-protected modes. These transmission bands are labeled with the modes responsible for the resonant response. A perturbation to normal incidence will leave the mode profiles nearly identical to the zone center ($k_x = k_y = 0$) modes, ensuring the overlap integral remains small and the associated coupling is weak. Thus, resonant high-Q transmission peaks are observed near normal incidence, and the peaks widen as $|k_x|$ or $|k_y|$ increases. Interestingly, the overlap integrals for the two sets of modes, TM and TE, result from different mechanisms. For the TM cases, the off-normal incidence simply results in non-zero overlap integrals for every field component. The TE peaks result from a small polarization overlap between the incident field and slab modes due to magnetic field-depolarization when k_y is introduced.

The agreement between the simulated transmittance and the modal analyses is strong. The transmittance bands for $|k_x| > 0$ align exceptionally well with the dispersion relations of Figure 3.6, with deviations only observed for the estimated TM_1^+ and TM_2^+ bands. The

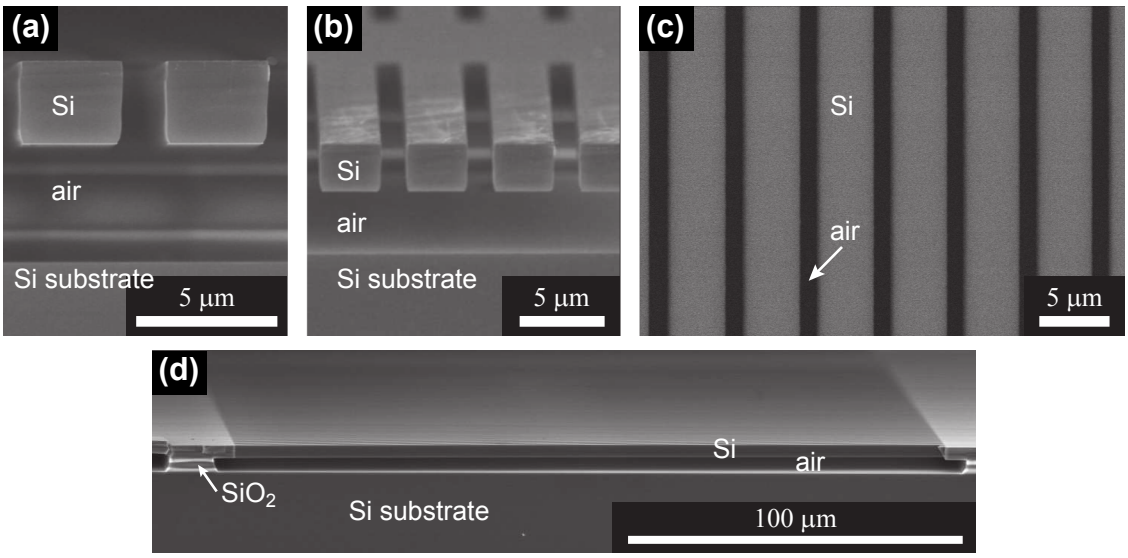

Figure 3.9: SEM micrographs of representative suspended silicon grating in (a) cross-sectional view, (b) oblique view, (c) plan view, and (d) side view. *©2014 J. M. Foley. Used with permission.*

transmittance bands associated with the TE modes are also in excellent agreement with the zone center ($\boldsymbol{k} = 0$) frequencies of the TE dispersion relations. Furthermore, the TM_3^- coupling responsible for the transmittance band at $\frac{\omega\Lambda}{2\pi c} = 0.72$ persists as $|k_y|$ is increased, explicitly showing how the TM mode coupling is maintained while TE mode coupling is introduced. Notably, one would expect the transmission bands for $|k_y| > 0$ to increase in frequency with increasing $|k_y|$ due to the lack of periodicity in the y-direction, however, both TE_2^- and TE_4^- transmission bands initially decrease in frequency away from normal incidence. We attribute this decrease to avoidance crossings between these modes and the TM_1^+ and TM_3^- modes, which have the same symmetry within the C_s^{yz} point group and are slightly higher in frequency.

3.5 Experiment

3.5.1 Sample fabrication

J. Foley fabricated suspended silicon gratings matching the high contrast structure analyzed in section 3.2.3. The dimensions were scaled to provide greater than 90% reflectance at normal incidence in the long wavelength infrared frequency range between 20 and 40 THz (8-15 μm): $\Lambda = 4.9$ μm, $t = 2.85$ μm, $h = 4.05$ μm and $FF = 0.72$. This frequency range enables structure dimensions amenable to photolithographic processing and has technological importance for infrared imaging applications including surveillance [97] and remote

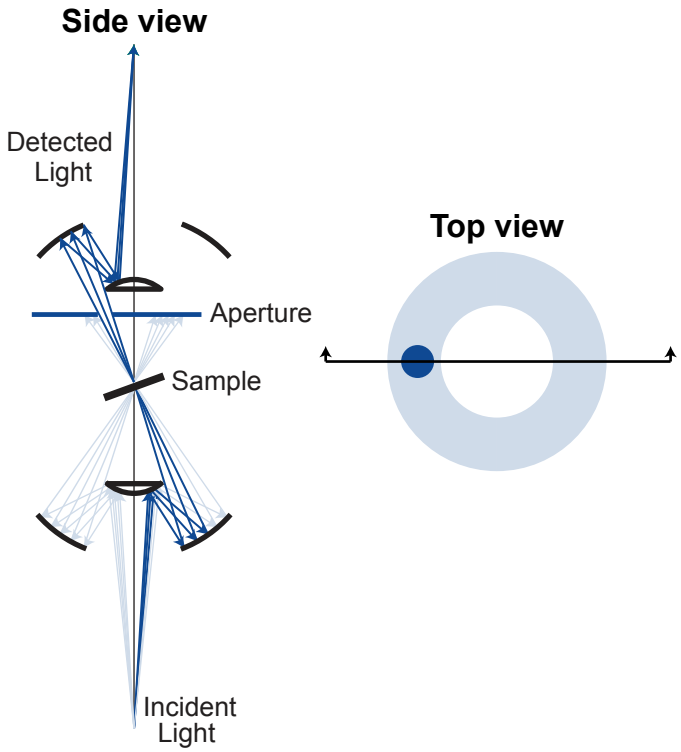

Figure 3.10: Transmittance measurement configuration. *©2014 J. M. Foley. Used with permission.*

sensing [98]. Fabrication began with a commercially available silicon-on-insulator wafer with 4 ± 0.5 μm and 4 ± 0.2 μm silicon and silicon-dioxide layer thicknesses, respectively. The grating geometry was defined using standard photolithography and reactive ion etching, while subsequent hydrofluoric acid etching suspended the 250×500 μm silicon grating slab. Figure 3.9, from [89], shows scanning electron micrographs of a representative suspended grating. As seen in the micrographs, the gratings exhibit negligible bowing and surface roughness relative to the incident wavelength. See [21] for additional fabrication details.

3.5.2 Measurement setup

Grating characterization was performed using a Perkin Elmer Spectrum GX Fourier Transform Infrared (FTIR) spectrometer with an AutoImage microscope attachment. A potassium bromide (KBr) beamsplitter was used for the mid-infrared characterization, and an internal aperture was used to specify the sample area to be characterized. A wire-grid polarizer, with manual orientation specification ($\pm 5^\circ$), was placed in the detected light's path. The system uses a liquid nitrogen cooled mercury cadmium telluride (MCT) detector.

4 cm^{-1} resolution was used for all measurements, with a mirror scan velocity of 2 cm/s. This corresponds to a resolution of 40 nm at an operating wavelength of 10 μm. Consequently, for resonant phenomena, the highest measurable quality factor ($Q = \omega/\delta\omega$) is 125.

The commercial FTIR uses Cassegrain objectives to focus and collect light. These high numerical aperture lenses (NA = 0.6) provide incident light between 16° and 36°. Figure 3.10, from [89], shows a schematic of the incident and detected light configurations for the transmittance measurements. To limit the incident wavevectors to particular values near normal incidence, we used a custom sample holder and an aperture placed above the sample.

The custom sample holder has a 20° tilt relative to the horizontal stage that enables normal incidence characterization. An optical iris suspended above the sample was used as an aperture to constrain light reaching the detector. The size of the aperture and height above the sample was dictated by the signal strength. With the aperture adjusted to obtain a measurable signal, the range of collected angles was $\theta \pm 3^\circ$, resulting in an effective numerical aperture of NA $\simeq 0.05$. The aperture's location, and thus the measured incident angle, was manipulated using an xyz-translation stage with micrometer adjustment.

Strictly speaking, the aperture should have been placed between the source and the sample when constraining the incident light angle; that is, underneath the sample. However, the geometric constraints of the commercial FTIR prevented this. Filtering the transmitted light above the sample is acceptable in this case because the grating period is subwavelength over the measured frequency range, so only the zero-th diffraction order produces propagating waves.

3.5.3 Results

Figure 3.11 shows the experimental and simulated transmittance for a grating with dimensions $\Lambda = 4.9\,\mu$m, $t = 2.85\,\mu$m, $h = 4.05\,\mu$m and $FF = 0.72$ and incident light configurations analyzed: Angle I, Angle II, and Angle III, as well as a fourth angle, Angle IV (θ, $\varphi > 0^\circ$). In contrast to the preceding analyses that defined the incident field using the in-plane wavevector, the experimental demonstration had the incident field defined by θ and φ. As a consequence, the plot labels of Figure 3.11 do not represent a single point in k-space, but instead they represent a range of incident wavevectors confined to the $k_x k_z$- and $k_y k_z$- planes for Angles II and III, respectively.

In the absence of nonradiative losses, the quality factors of the peaks associated with modes TM_1^- and TE_2^- are expected to increase infinitely as the incident light approaches

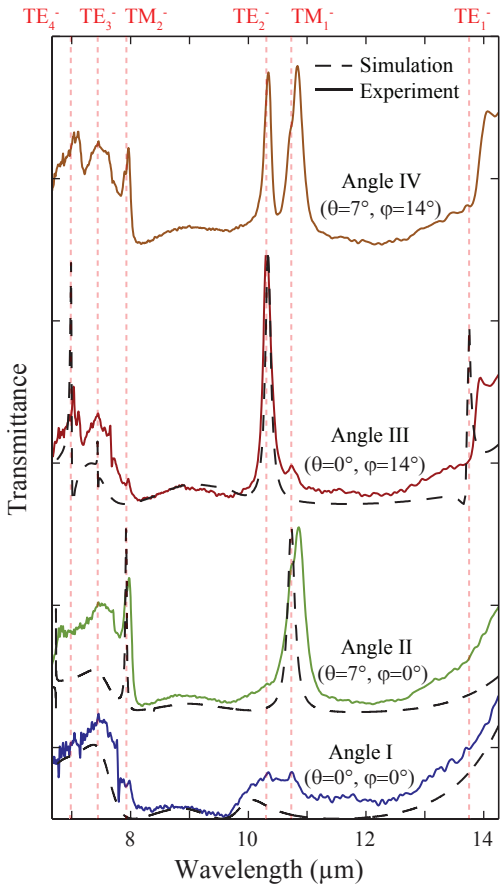

Figure 3.11: Experimental and associated simulated transmittance of a grating with various incident wave configurations. The as-built dimensions were $\Lambda = 4.9\ \mu$m, $t = 2.85\ \mu$m, $h = 4.05\ \mu$m and $FF = 0.72$. Broadband reflectance, TM selective filtering, TE selective filtering and mixed TE and TM filtering associated with the incident wave vector at various points in the Brillouin zone: Point I ($\theta = \varphi = 0°$, Point II ($\theta = 7°$, $\varphi = 0°$), Point III ($\theta = 0°$, $\varphi = 14°$), and Point IV ($\theta = 7°$, $\varphi = 14°$), respectively.

normal incidence. However, when the radiative coupling becomes less than the nonradiative losses, the peak height begins to decrease without appreciable further reductions in the peak width. The incidence angles reported in figure 3.11 are those for which the nonradiative and radiative losses are of the same order of magnitude, as discussed further below.

At normal incidence, Angle I ($\theta = \varphi = 0°$), the low-transmittance background is demonstrated to be below 7% between 8 and 13 μm, which agrees well with the simulated transmittance. The corresponding simulated response has been reduced to 70% of its calculated value to account for the reflection loss at the substrate's exit interface, which was not included in the simulation due to computational demands.

The experimental response at Angle II ($\theta = 7°$, $\varphi = 0°$) is similarly shown to agree well with its as-built simulation. In this case the transmittance has been normalized to the peak transmittance of the experimental results (26%) to accentuate the qualitative agreement between the datasets. The experimental response exhibits transmission peaks associated with both the TM_1^- and TM_2^- modes, with moderate broadening and phase shifts compared to the simulation that will be explained below.

Similarly, moving to Angle III ($\theta = 0°$, $\varphi = 14°$) demonstrates selective coupling to TE modes as we expect. Peaks corresponding to modes TE_1^- and TE_2^- are clearly visible, and signatures of modes TE_3^- and TE_4^- are observable, with the normalized simulated response (36.5%) agreeing well with the data. For both TM and TE demonstrations, the transmission band frequencies are within 1% of those determined from the modal analysis, within the experimental error of measuring the grating dimensions.

To confirm the resonant response results from two separate mode sets, we took data at the low symmetry Angle IV ($\theta = 7°$, $\varphi = 14°$), which has non-zero k_x and k_y simultaneously. The corresponding spectrum exhibits transmission bands associated with both TM and TE modes, confirming our mode attributions at Angles II and III and the independence of the TM and TE mode sets. At the further reduced symmetry of Angle IV we would also expect resonant transmission bands from modes TE_1^+ and TE_2^+ as mentioned in the group theoretical analysis of TE mode coupling. Unfortunately, due to the small overlap integrals in both the k_x and k_y directions, the resulting Qs were too high to be resolved experimentally.

There is strong agreement between the experimental and simulated structure response. However, several of the expected peaks are not well defined and the experimental quality factors are lower than those simulated. The maximum demonstrated quality factors for the two dominant transmission bands centered in the opaque background, associated with coupling to TM_1^- and TE_2^- modes, were $Q_{exp}(\theta = 7°) = 33$, and $Q_{exp}(\varphi = 14°) = 64$, respectively. These are much smaller than their expected quality factors due to resonance

broadening, $Q_r(\theta = 7^\circ) = 113$, and $Q_r(\varphi = 14^\circ) = 107$, respectively. The reduction in the quality factor can be attributed to the angular extent allowed by the aperture, non-radiative losses that can dominate the response at lower angles, and the finite grating size.

The $\pm 3^\circ$ angular uncertainty allowed by the iris setup, discussed above, is expected to significantly affect the resonant response. A range of angles probes a range of different k_x or k_y values, which due to the slope of the transmission bands of Figure 3.8 is expected to result in a broader observed peak. This angular dependence is evident in the experimental data, where the transmission peak corresponding to the TE_2^- mode is narrower and more symmetrical than the peak corresponding to the TM_1^- mode. The highest possible measured quality factors allowed by the iris' angular extent are $Q(\theta = 7 \pm 3^\circ) \simeq 110$, and $Q(\varphi = 14 \pm 3^\circ) \simeq 175$, for TM and TE modes respectively.

Even with better angular control of the incident light, material absorption and inhomogeneous broadening due to disorder scattering are still expected to put an upper bound on the achievable Q as $\theta, \varphi \to 0^\circ$. Using optical properties from the literature for silicon in this frequency range [96], the maximum quality factor due to non-radiative losses is on the order $Q_{nr} \sim 10^4$. This estimate serves as an upper bound, and does not include additional absorption losses due to dopants or impurities introduced during the fabrication process, nor does it include scattering losses due to manufacturing imperfections. Using the relation $1/Q_{tot} = 1/Q_r + 1/Q_{nr}$, we estimate the non-radiative quality factor in our samples to be $Q_{nr} \simeq 100$.

Although the structures are fairly tolerant of fabrication imperfections, deviations in the symmetry of the structure are expected to affect the response on resonance. Optimizing the fabrication further to reduce surface roughness and improve sidewall profiles may increase the transmittance and Q.

Finally, it is known that the grating size affects the attainable quality factor and peak transmittance on resonance [99, 100]. Since our grating was limited to approximately 100 periods, this could limit our peak transmittance and Q. Despite the experimental limitations that make resolving the higher Q resonances more challenging, we were able to observe signatures from all but the two highest-Q expected resonances.

3.6 Conclusions

We have demonstrated selective coupling to symmetry-protected guided modes of a dielectric grating to realize transmission filtering capabilities. Using a group theoretical analysis, we determined the selection rules that govern plane wave coupling to the grating's supported modes. Using these selection rules, we provided a low-transmittance background

by maximizing the coupling strength to modes accessible at normal incidence. Introducing a perturbation to normal incidence in the k_x ($\theta > 0°$) or k_y ($\varphi > 0°$) directions, weak coupling to TM and TE symmetry protected modes, respectively, was shown to result in high-Q transmission peaks within the low-transmittance background. We simulated and experimentally verified the grating's transmission filtering capabilities at various incidence angles, which were shown to agree well with each other and the modal analysis. Although we have chosen to relax the symmetry by introducing off-normal incident light, similar response is possible at normal incidence if instead the symmetry of the grating itself is broken. This could be achieved by changing the period and fill factor across the extent of the grating or by etching the grating at an angle to break the symmetry across the yz-plane, $\hat{\sigma}_x$ [81, 101].

We note that other types of infinite-Q modes have been observed above the light line in photonic crystal slabs, that are not due to symmetry protection and occur away from normal incidence [48]. It may be possible to exploit such modes to create similar filters at arbitrary incidence angles.

These transmission filters have potential to be used in a wide array of applications. While our demonstration was performed in the LWIR, the operating principle is scalable to any wavelength range, if similarly lossless materials are available. In the LWIR, these filters may enable improved hyperspectral imaging capabilities for remote sensing and surveillance applications [97, 98]. Hyperspectral imaging records the electromagnetic spectrum for every point in a viewing plane, providing enhanced discrimination between objects. These gratings have potential to be integrated at the pixel or sub pixel level, and only require a single dielectric layer, which may lead to improved and more cost-effective imaging capabilities. The frequencies of the transmission peaks can be tuned during manufacture by changing the grating period without altering the thickness or material properties [20, 21], making arrays of such grating pixels feasible and simple to manufacture with conventional integrated circuit techniques.

Finally, we note that selective emitters/absorbers are expected to increase the efficiency of thermo-photovoltaics [102, 103]. Because these one-dimensional gratings have a high density of states, compared to two-dimensional structures, they may be especially suited for such systems.

CHAPTER 4

Resonances in Finite Periodic Structures

[1] In this chapter, we will discuss another method of confining electromagnetic fields in a finite sized photonic crystal, to form a mirrorless resonant cavity. [2]

A hole, impurity, or other defect in an infinite photonic crystal can act as a resonant cavity, with resonant frequencies within the forbidden gaps of the crystal [14, 36, 106]. The surrounding crystal is essentially a mirror that serves to confine the light.

Less obviously, a defect-free but finite photonic crystal surrounded by free space (see figure 4.1) can also support resonant modes, as observed by Xu *et al.* [107] in a numerical study of a finite square lattice of dielectric rods. In this case, the resonant frequencies occur just *outside* the forbidden gaps, within the allowed bands of the crystal. The resonant states extend throughout the crystal, with high field amplitudes near the center and low amplitudes at the edges, analogous to surface-avoiding phononic modes observed in multilayer condensed matter systems [108, 109]. More precisely, the resonant fields observed by Xu *et al.* could be divided using the envelope function (effective-mass) approximation [110–112] into a rapidly-varying part determined by the underlying crystal structure and an envelope function corresponding to the modes of a conventional mirrored cavity. With their small field amplitudes at the edges of the crystal, the resonant modes exhibited low radiative losses, yielding sharp spectral features. However, given the lack of any actual mirrors, it was not clear *why* the envelope function should have nearly-Dirichlet boundary conditions, or which geometries would show similar behavior.

Merlin and Young [22] recently proved using perturbation of boundary conditions [113] that the surface avoiding modes observed by Xu *et al.* are in fact general features of finite

[1] Portions of this chapter were originally published in [22] (©2014 Optical Society of America). Reused here with permission.

[2] Other types of mirrorless resonant cavities are well-known. Examples include dielectric systems that rely on total internal reflection to confine fields close to the boundary (*e.g.*, whispering gallery modes [104]), systems with modes that lie outside the light cone (such as surface plasmons in metals), highly disordered materials (Anderson localization [105]), and the systems discussed in chapter 3 with modes that are confined by their symmetry [74, 75].

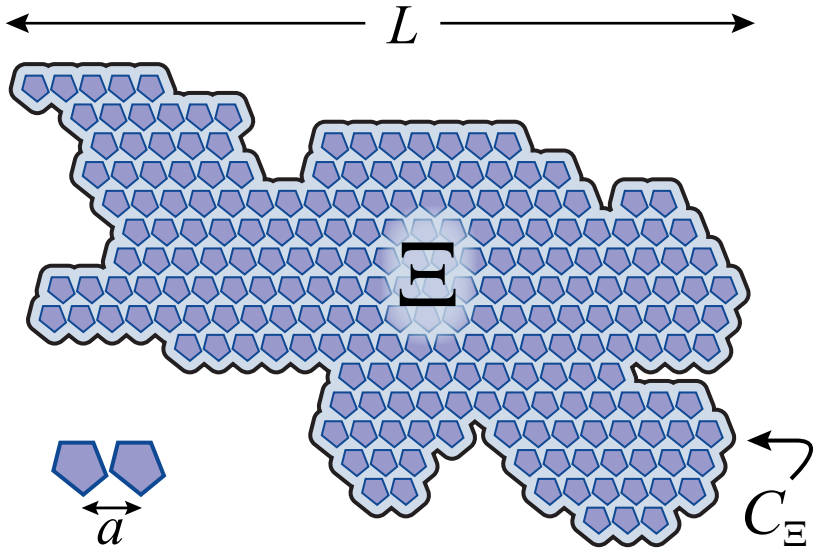

Figure 4.1: Schematic diagram showing a finite photonic crystal and the length scales, L and a, of the problem. C_Ξ is a mathematical curve that tightly encloses the crystal, and Ξ is the interior region it describes.

photonic crystals, regardless of dimensionality (1d, 2d, or 3d) or the shape of the boundary. The finite crystal acts as a mirrorless resonant cavity with surface avoiding modes if the crystal size L is large compared to the period a, and the underlying crystal supports modes with quadratic dispersion $(\omega - \omega_0) \sim (q - q_0)^2$, where q is the crystal wavevector. This dispersion relation occurs in photonic crystals near the edges of allowed bands. In the absence of all but radiative losses, the quality factor Q_r, defined as the ratio between the frequency ω and the width $\delta\omega$ of a particular mode, and the finesse $F = \Delta\omega/\delta\omega$, where $\Delta\omega$ is the separation between adjacent modes, are given by $Q_r \sim (L/a)^3$ and $F \sim L/a$. In section 4.1, we will present a number of examples illustrating these general features.

The high-Q modes discussed here should not be confused with the resonant guided modes supported by periodically patterned dielectric slabs [15, 71] that were discussed in chapter 3. These modes occur in one- or two-dimensional photonic crystal slabs with thickness comparable to the wavelength λ, which are assumed to have an infinite number of in-plane periods. Consequently, the quality factors with a lossless medium are dominated by out-of-plane radiative losses. If the number of periods is finite (but still large), then the quality factor scales according to $Q \sim L/a$, where a is the period, due to relaxation of the phase-matching condition for coupling to radiative modes [99, 100, 114]. In contrast, surface avoiding modes concern radiation from the edge of the periodic region without regard for out-of-plane losses. The quality factor due to edge losses for surface avoiding modes scales according to $Q \sim (L/a)^3$. In section 4.2, we will present an experimental

demonstration of a finite periodic slab, which combes both the in-plane surface avoiding mode confinement effect with the symmetry-based out-of-plane confinement discussed in chapter 3.

4.1 Examples

4.1.1 A 1d photonic crystal

One-dimensional photonic crystals provide the simplest example of mirrorless resonant cavity behavior. Figure 4.2 shows the calculated transmission coefficient T for a periodic multilayer structure of period a and total length Na (see section 1.2.4), with resonant modes producing hsarp transmission peaks. The frequency range shown is that of the second, 'optical,' band of the photonic crystal (in the first, 'acoustic,' band, $\omega \to 0$ for $q \to 0$). The surface-avoiding, cavity modes occur near the edges of the allowed band, where the q-dependence of ω is quadratic. Figure 4.2(b) shows the intensity for the first three lowest-lying modes. Their envelopes are in a one-to-one correspondence with the intensity profiles of a mirrored resonant cavity (as well as with the quantum eigenfunctions of a particle in an infinitely deep potential well [115]), which can be ordered according to the number of zeros of the Dirichlet eigenfunctions. The results in figure 4.2(c) show that the distance in frequency between two arbitrary peaks and their width scale, respectively, like N^{-2} and N^{-3}. Also note that the number of peaks for which $T = 1$ equals $N - 1$ [115].

4.1.2 A 2d photonic crystal

Figure 4.3 shows a two dimensional triangular lattice of dielectric rods. The dielectric constants of the air ($\epsilon_1 = 1$) and rods ($\epsilon_2 = 15$) and the ratio of the rod radii to the lattice space ($r/a = 0.2$) were chosen so that, according to calculations using the MIT Photonic Bands software [116], the photonic crystal exhibits two forbidden gaps in the TM band structure (electric field parallel to the rods). The lower frequency gap is defined by band edges lying outside the light cone, at the K- and M-points of the Brillouin zone. The gap extends from $\omega \simeq 0.248 \times (2\pi c/a)$ (K-point) to $\omega \simeq 0.416 \times (2\pi c/a)$ (M-point). The second gap has band edges within the light cone, both at the Γ-point, at frequencies $\omega \simeq 0.509 \times (2\pi c/a)$ and $\omega \simeq 0.564 \times (2\pi c/a)$.

Figure 4.4 shows finite element simulation results confirming the presence of surface avoiding modes for a finite crystal with the underlying triangular lattice of figure 4.3 and a hexagonal boundary. The dielectric constant for the rods was set to have a small imaginary

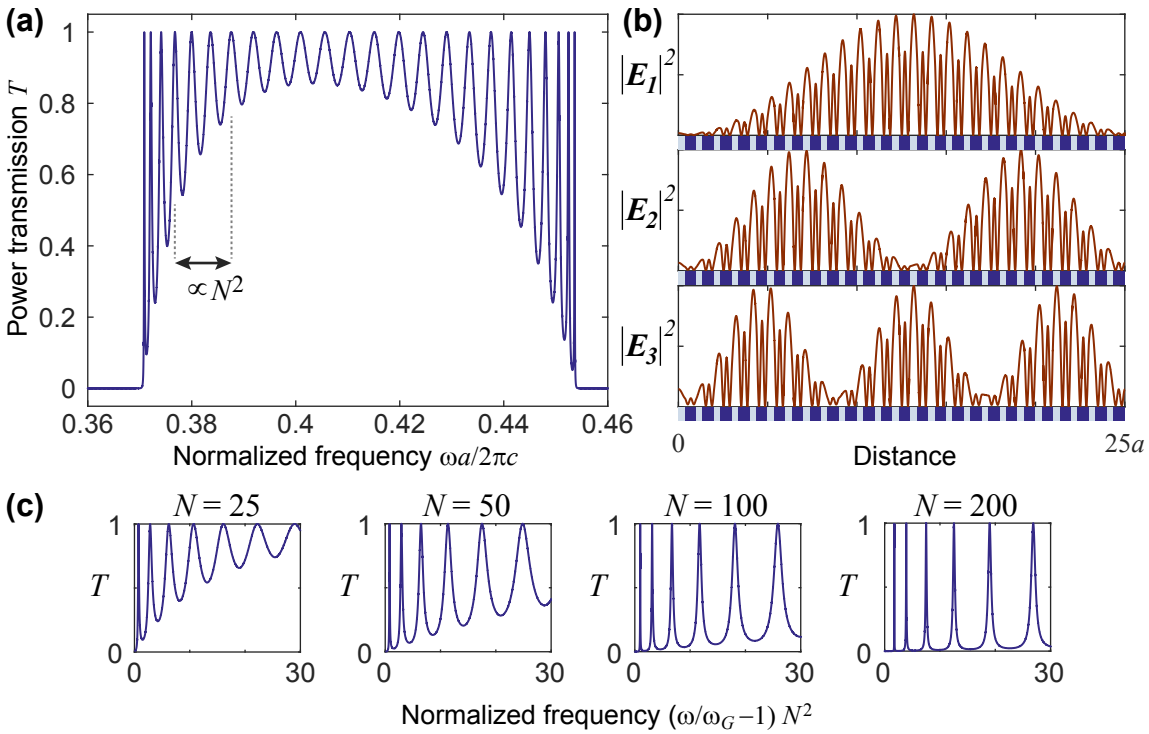

Figure 4.2: (a) Transmission spectrum at normal incidence through a Si/SiO_2 dielectric stack (see figure 1.5a) comprising $N = 25$ identical bilayers of length a with $d_1 = 0.37a$ and $d_2 = 0.63a$, and refractive indices $n_1 = 1.5$ and $n_2 = 3.9$. Frequency is in normalized units, $\omega a/2\pi c$. (b) The square of the field for the first three modes above the band edge at $\omega_G \simeq 0.37 \cdot 2\pi c/a$. (c) Transmission spectra for different numbers of periods N, showing scaling behavior.

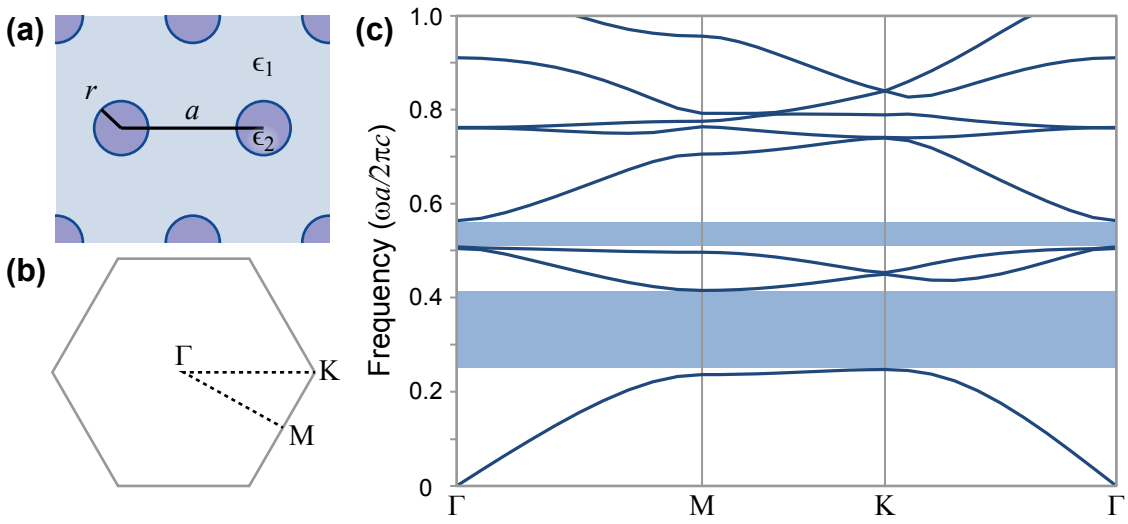

Figure 4.3: (a) Schematic diagram of a triangular lattice of dielectric circular rods with radius r, lattice spacing a, and permittivity ϵ_2, surrounded by a medium with permittivity ϵ_1. (b) Brillouin zone of the triangular lattice, showing high symmetry points. (c) Photonic band diagram for TM modes (electric field parallel to the rods) in the triangular lattice with $\epsilon_1 = 1$, $\epsilon_2 = 15$, and $r/a = 0.2$. Forbidden bands are highlighted in blue.

part ($\epsilon_2 = 15 \times (1 + 0.0001i)$); consequently, resonant modes with high fields in the rods produce peaks in the calculated absorption spectrum when excited by point current sources. As for the one-dimensional photonic crystal, the surface avoiding modes manifest themselves as narrow peaks that occur just below and just above the edges of the allowed bands.

Contour plots of the field magnitude are shown for several of the modes nearest to the band edges. As expected from the results of ref. [22], the corresponding envelope functions are in close correspondence to Dirichlet modes of a similarly shaped mirrored cavity. The envelopes of the modes also resemble those of Fabry-Pérot–type modes seen in uniform dielectric shapes. However, they differ from Fabry-Pérot–type modes in several important respects; namely, the field is rapidly varying on the length scale of a lattice constant, the resonance frequencies are near the band edges of the underlying lattice, and the Q of the peaks is much higher.

4.1.3 An open Fabry-Pérot cavity

In an early study of an open maser interferometer consisting of two flat parallel mirrors with finite widths, Fox and Li [70] noted the surprising result that relatively high-Q resonant modes exist in such a system with no side-wall boundaries, even with the high diffraction

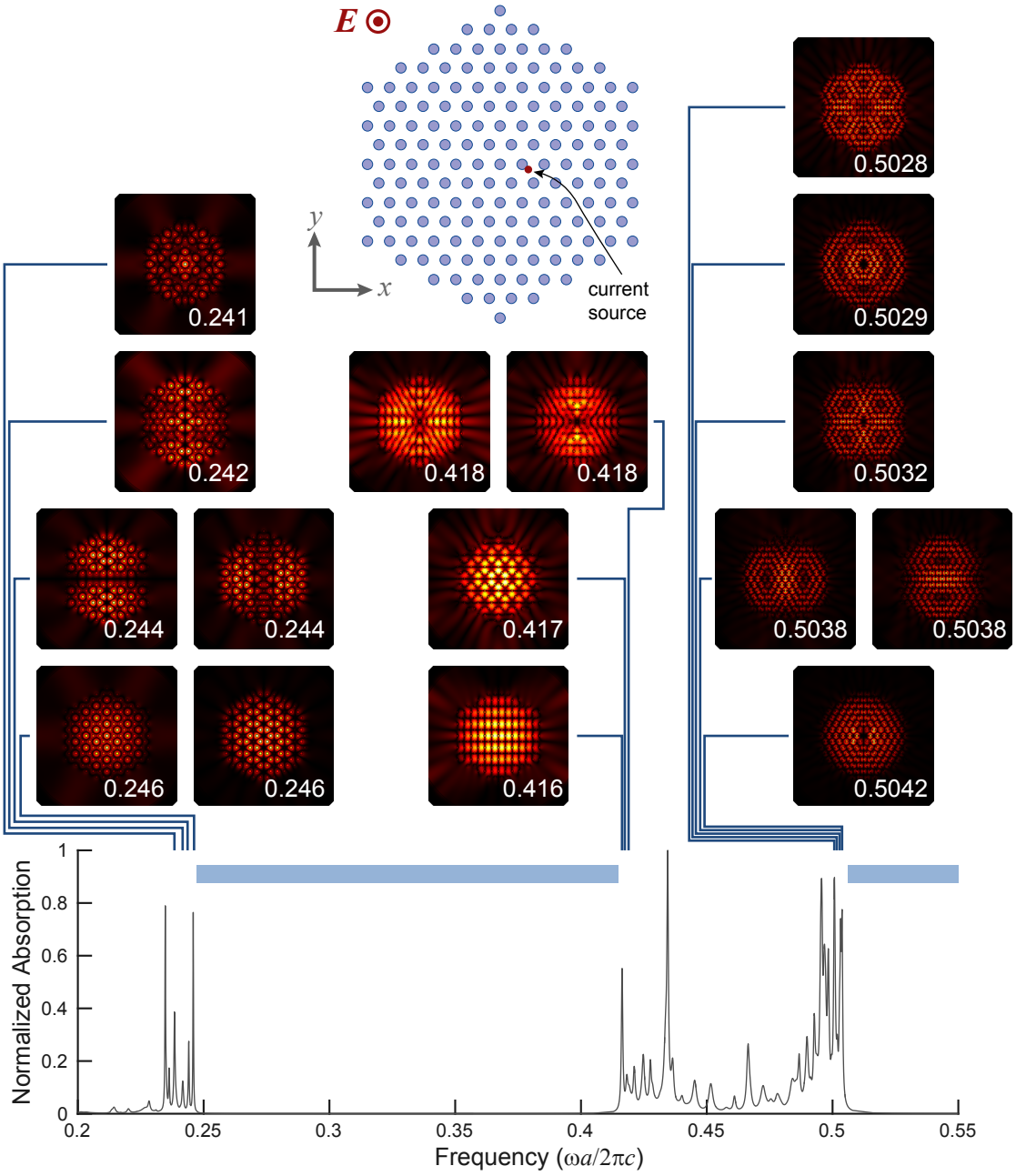

Figure 4.4: Absorption spectrum calculated using finite element method with a fixed excitation for a 2d finite photonic crystal comprising 157 circular rods in the triangular lattice of figure 4.3. The dielectric rods are slightly lossy, with $\epsilon_2 = 15(1 + 0.0001i)$. Absorption peaks near the band edges correspond to resonant TM modes. Contour plots of $|E_z|$ are shown for selected modes, labeled by their frequency in normalized units $(\omega a/2\pi c)$. Forbidden frequency bands are highlighted in blue. [Top inset]: schematic of the finite crystal with coordinate system and electric field polarization shown.

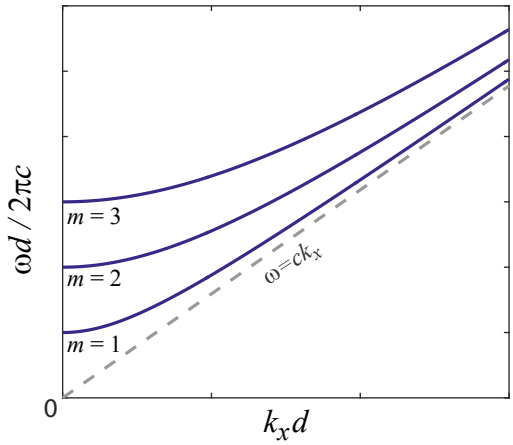

Figure 4.5: Dispersion relations $\omega(k_x)$ for a parallel-plate waveguide.

losses expected for plane waves propagating between the flat mirrors (these high diffraction losses are the reason most practical open cavities use concave mirrors). After many round trips, waves propagating between the mirrors at the Fabry-Pérot frequencies converge to steady state profiles that minimize diffraction losses, with high amplitudes near the center of the plates and low amplitude at the edges.

This behavior can be explained in terms of surface avoiding modes. Specifically, two flat mirrors separated by a distance d comprise a parallel plate waveguide, and each successive Fabry-Pérot frequency $\omega_{c,m} = m\pi c/d$ corresponds to the cutoff frequency of a TE waveguide mode, which has the dispersion relation (see figure 4.5) :

$$\omega_m^2 = c^2(k_x^2 + m^2\pi^2/d^2) \tag{4.1}$$

where k_x is the propagation constant parallel to the walls. Because the waveguide mode dispersion near the cutoff frequencies is quadratic in lowest order, the results of ref. [22] apply, and the open two-mirror system is expected to support high-Q surface avoiding modes with lateral profiles resembling Dirichlet modes, just as observed by Fox and Li. The modes are expected to exist just above the Fabry-Pérot frequencies and have quality factors that scale as $Q \sim L^3$, where L is the width of the mirrors.

4.2 Experiment - a finite periodic slab

This section describes an experiment confirming mirrorless resonant cavity operation at microwave frequencies (2-9 GHz) in a finite photonic crystal slab. Figure 4.6 shows the experimental slab design. The slab comprises 157 dielectric rods with the same triangular

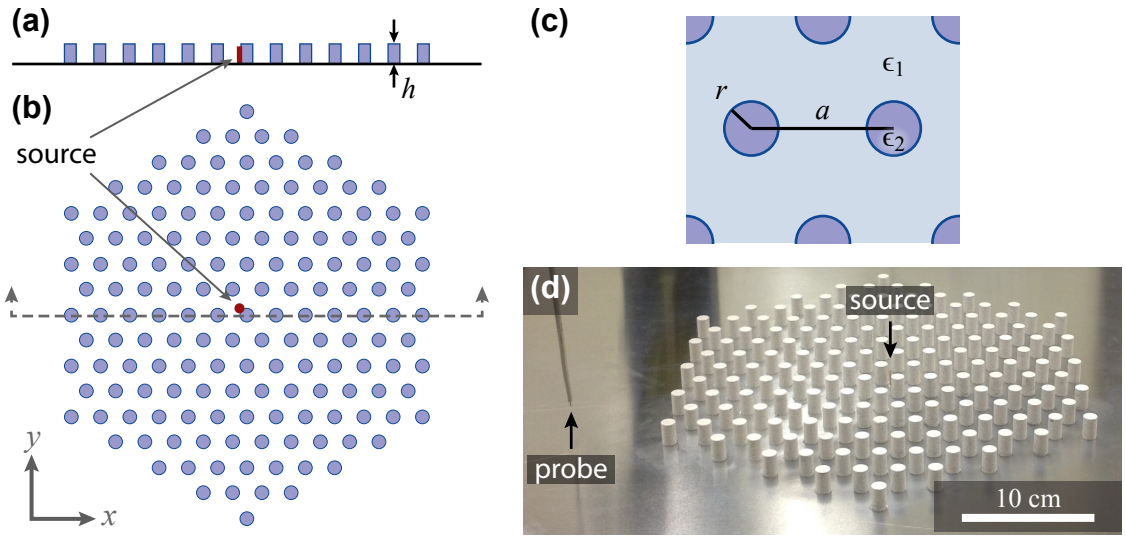

Figure 4.6: As-built finite crystal slab used in the experiment. (a) Cross-section schematic. (b) Plan-view schematic. (c) Definition of lattice parameters. (d) Photograph (oblique view) of the slab while installed in the measurement apparatus.

lattice parameters and hexagonal boundary as the 2d crystal studied in section 4.1.2. However, it differs from the 2d example in several important respects. Whereas the dielectric rods in section 4.1.2 were assumed to extend infinitely in the z direction, making a truly 2d problem, the rods in the experiment have finite height h, and are attached to a conducting ground plane below and nothing above. Thus, out-of-plane radiation losses are important considerations in the experiment. Second, the underlying band structure of the 'infinite' photonic crystal will be different for the experimental slab than for the 2d crystal. Whereas the band structure in figure 4.3 arises from a basis set of plane waves diffracting in the periodic lattice, the appropriate basis functions for the slab are the guided modes of a dielectric waveguide (see section 3.2). Specifically, noting the ground plane and using image theory, the predominant resonant states should resemble the lowest order TM odd modes of a dielectric slab with thickness $2h$ and a refractive index equal to the spacial average of the figure 4.6 lattice. As shown in section 3.2.3, the guided modes in a high contrast grating exhibit pseudo gaps, with the resonant modes showing approximately quadratic dispersion near high symmetry points in the Brillouin zone. Thus, surface avoiding modes are expected similar to the purely 2d case, albeit at slightly different frequencies.

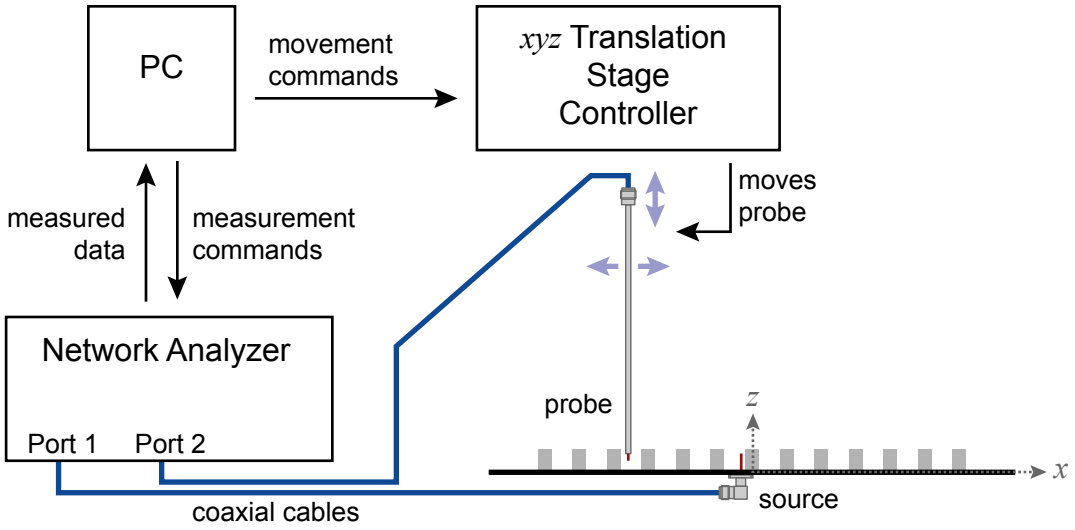

Figure 4.7: Block diagram of the experimental setup.

4.2.1 Fabrication

Figure 4.6(d) shows the assembled experimental slab. To give operation operation at microwave frequencies, the rods have diameters $2r = 3/8$ in (0.953 cm) and lattice spacing $a = 15/16$ in (2.38 cm), giving $r/a = 0.2$. The rod height is $h = 5/8$ in (1.59 cm). The rods are TiO_2 powder cured in a thermoplastic resin binder (Emerson and Cuming ECCO-STOCK HiK), with permittivity $\epsilon_2 = 15 \pm 0.45$ and dissipation factor $\delta < 0.002$. Using a positioning template, the rods were attached to a 38×38 inch alloy 6061 aluminum ground plane with nitrocellulose lacquer (Wet n Wild Wild Shine Nail Protector, Clear 401A). The overall width of the slab was approximately $L \simeq 13a = 16$ in (31 cm).

To excite the modes, an SMA coaxial panel post (Fairview Microwave SC3782) was attached below the ground plane, with the coaxial shield soldered to the ground plane and the 0.050 in center conductor extending vertically through the ground plane near the center rod. The connector's dielectric jacket was trimmed so that only the center conductor protruded through the ground plane.

4.2.2 Measurement methods

Figure 4.7 shows the block diagram of the experimental setup, designed to measure the electric field amplitude and phase at arbitrary positions near the slab [117]. A small probe, made from a semi-rigid coaxial cable with the center conductor protruding 2 mm beyond the shield, was oriented vertically and attached to a three-axis translation stage. Using a

network analyzer (Agilent E8361A) with the source connected to Port 1 and the probe connected to Port 2, the complex S-parameters were measured in the frequency range 2 - 9 GHz. Given the polarization of the probe, the S_{21} transmission parameter was then proportional to the z-component of the electric field at the position of the probe's exposed center conductor. An automated computer program interfaced to the translation stage controller was used to position the probe at the desired measurement points, as well as collect the S_{21} spectrum at each point.

The measurement surfaces were circles of radius 20 cm centered on the slab, at fixed heights above the ground plane. Within each measurement surface, the S_{21} spectrum was measured at 49,862 equally spaced points in the xy-plane (minus any points inside the rods). To detect the presence of resonant modes that have high field magnitudes near the slab, the square magnitude of the S_{21} measurement (proportional to $|E_z|^2$) was summed over all the points in the measurement surface. The result was a spectrum of $\sum |E_z|^2$ vs. frequency, with resonant conditions appearing as peaks. Each spectral measurement comprised 1,401 frequency points between 2 and 9 GHz, giving a frequency resolution of 5 MHz. Thus, the highest measurable quality factor was approximately 1000.

4.2.3 Results

Figure 4.8 shows the $\sum |E_z|^2$ spectra measured at the heights $z = 3$ mm, $z = 13$ mm, and $z = 18$ mm above the ground plane. The spectrum at each height is normalized to its greatest value. Notwithstanding the differences between a slab and a purely 2d crystal, the measured spectra are in qualitative agreement with the expected results for a 2d crystal (figure 4.4). In particular, two forbidden 'gaps' are evident between approximately 4.5 - 5.3 GHz and 6.7 - 7.5 GHz, respectively, with resonant peaks near the allowed band edges.

Near $z = 0$, the ground plane ensures that the electric field is predominantly vertical, but with the finite slab height, the field lines can be expected to diverge from vertical at greater heights. The various spectra in figure 4.8 give a sense of how quickly this folding over occurs for various resonant modes, with the modes at 5.45 GHz and 7.68 GHz departing from the 2d case more quickly than the lower frequency modes.

Figures 4.9 and 4.10 show the measured vertical electric field for selected frequencies corresponding to resonant modes. The field distributions and symmetries, particularly close to the ground plane, correspond qualitatively to the surface avoiding modes of the 2d crystal, figure 4.4. In particular, modes (i), (ii), and (iii) of figure 4.9 resemble the K-point modes below the first gap of the 2d crystal, while mode (iv) of figure 4.10 resembles the fundamental M-point mode above the first gap. Mode (v) of figure 4.10 corresponds to the

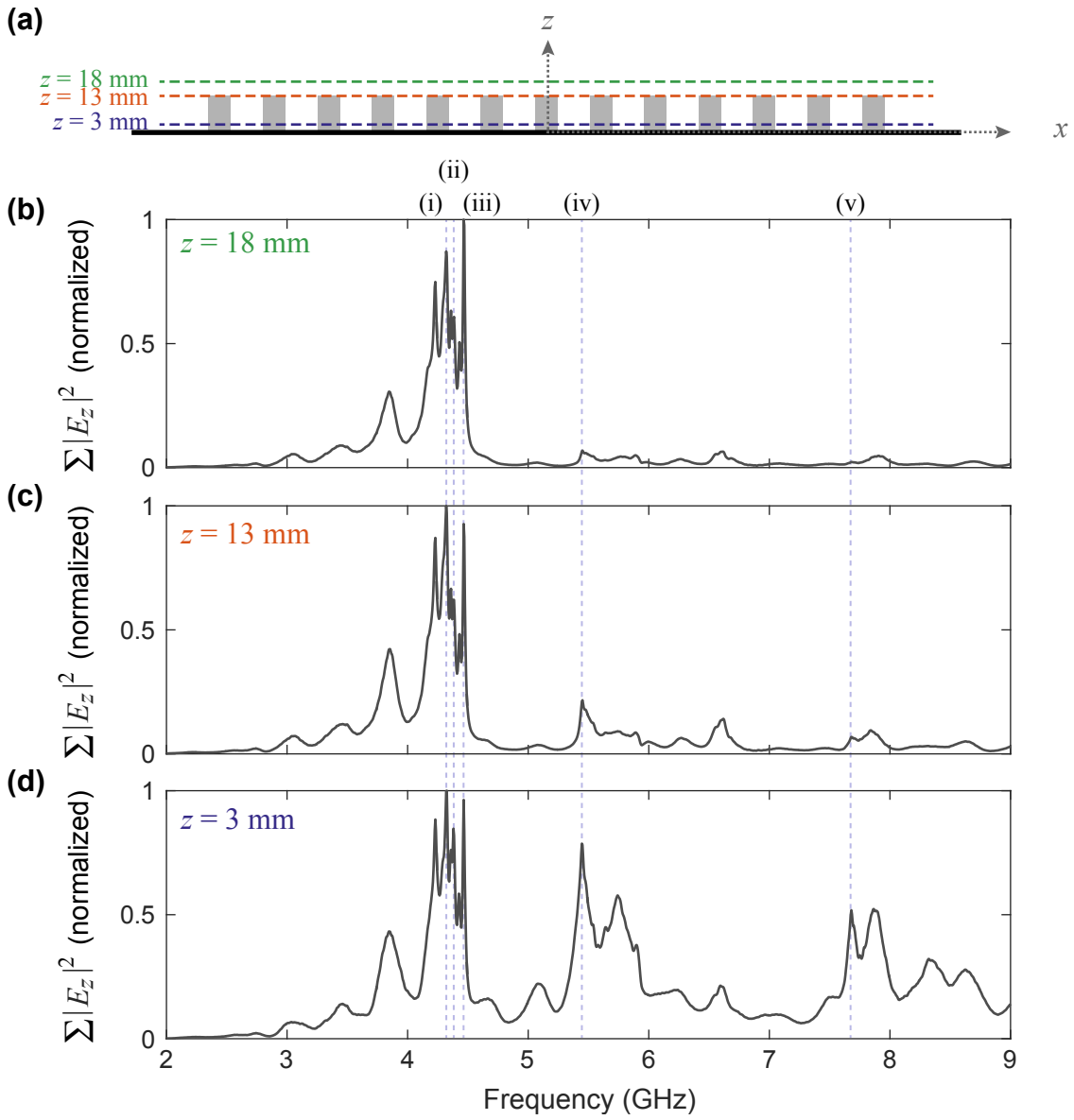

Figure 4.8: Sum of measured $|E_z|^2$ over all points within a circle of radius 20 cm centered on the finite crystal slab, at three different heights above the ground plane, normalized to the highest value at each height. (a) Schematic of slab cross-section showing the measurement planes. (b)-(d) Measured spectra for the planes $z = 3$ mm, $z = 13$ mm, and $z = 18$ mm, respectively. Roman numerals (i)-(v) indicate selected resonant modes for which field plots are shown in figures 4.9 and 4.10.

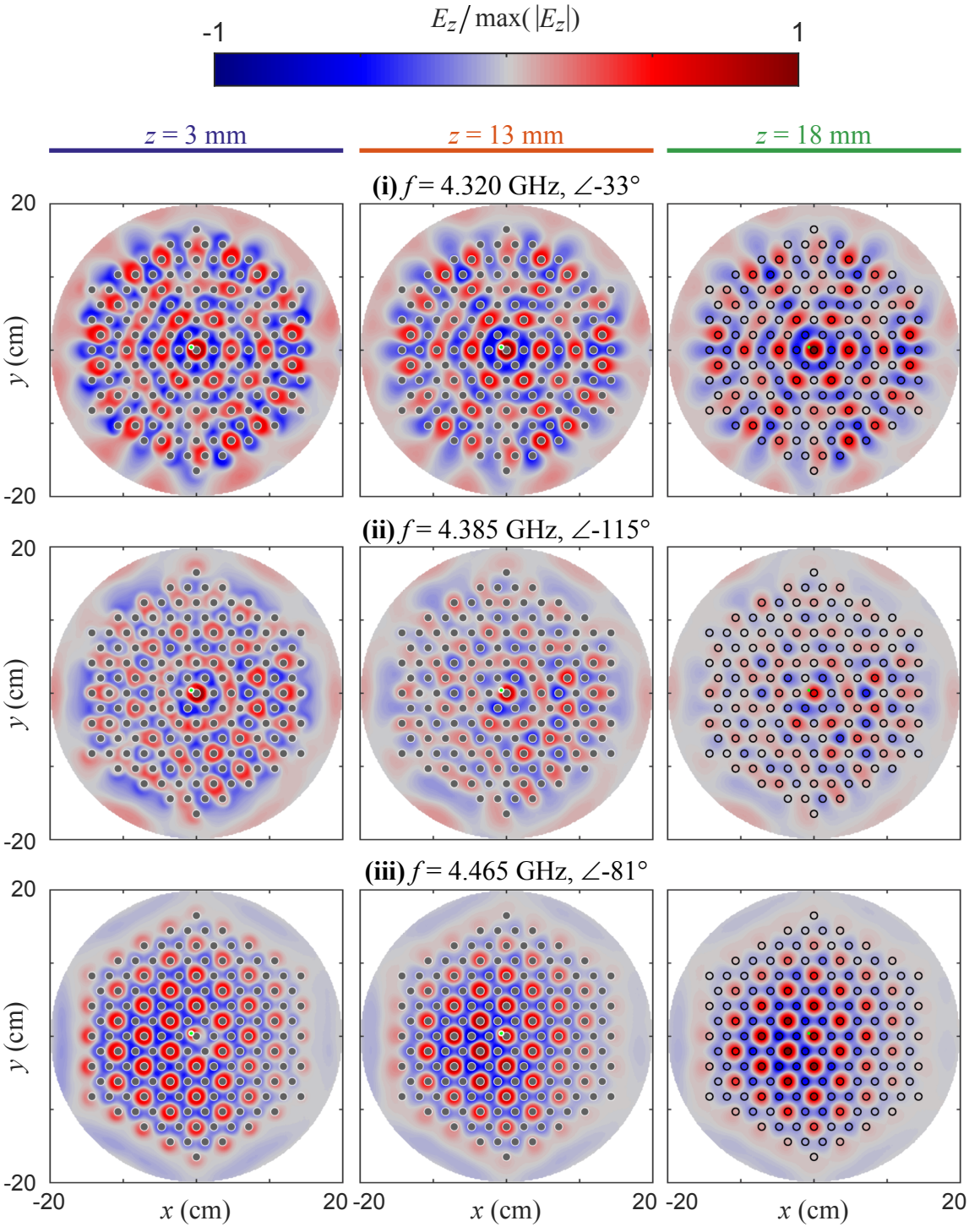

Figure 4.9: Contour plot of measured E_z in the finite crystal slab at three different heights ($z = 3$ mm, $z = 13$ mm, and $z = 18$ mm) above the ground plane for the modes at frequencies (i) 4.320 GHz, (ii) 4.385 GHz, and (iii) 4.465 GHz. The green dot indicates the source location.

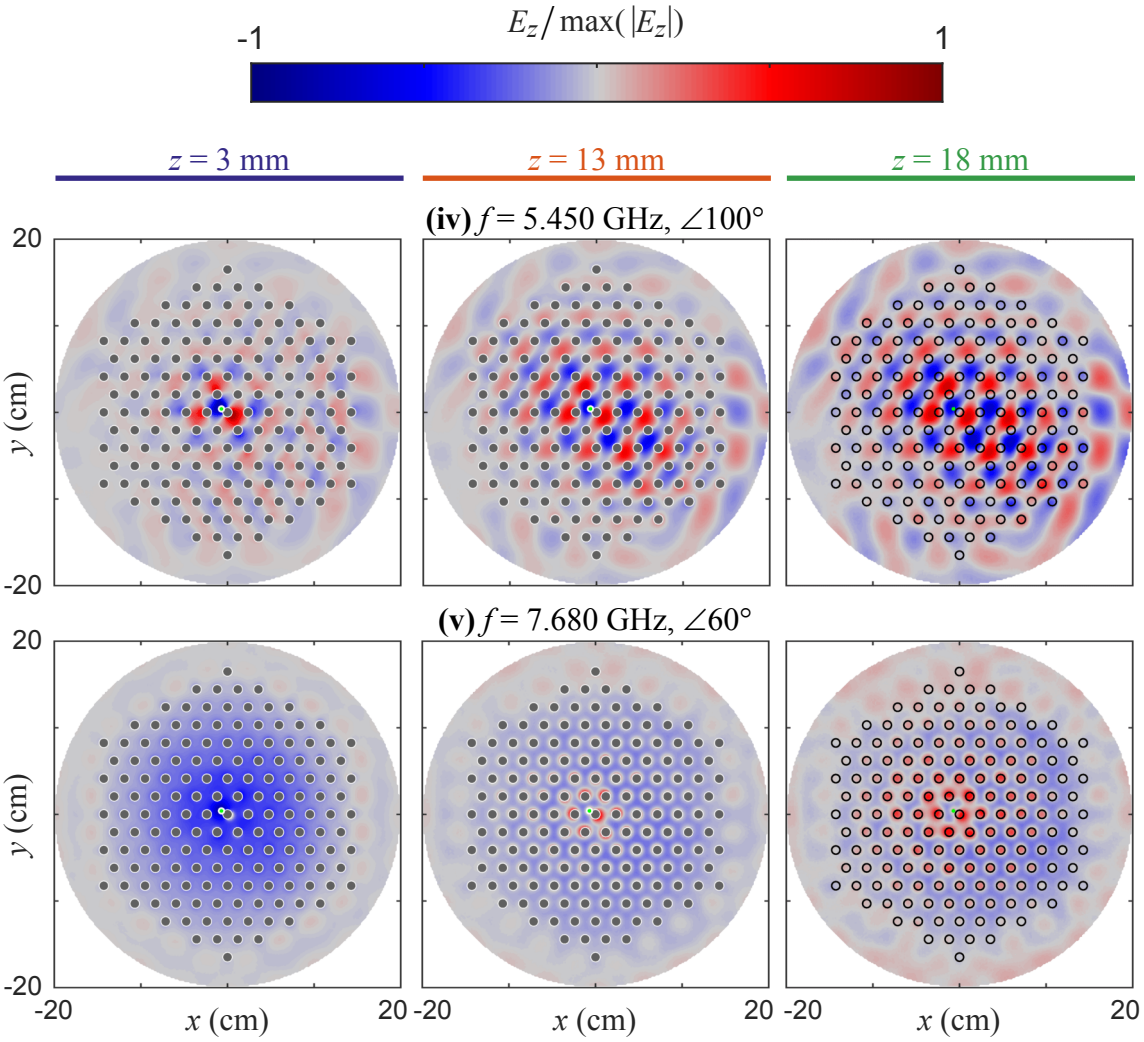

Figure 4.10: Contour plot of measured E_z in the finite crystal slab at three different heights ($z = 3$ mm, $z = 13$ mm, and $z = 18$ mm) above the ground plane for the modes at frequencies (iv) 5.450 GHz, and (v) 7.680 GHz. The green dot indicates the source location.

fundamental Γ-point mode above the second gap of the 2d crystal (not shown in figure 4.4). Thus, the field measurements confirm surface avoiding resonant mode behavior.

Mode (iii) has the sharpest measured peak, with a full width at half-maximum of 30 MHz, corresponding to $Q \simeq 150$.

4.2.4 Discussion and future work

As discussed previously, this experiment differs in important respects from the 2d crystal used in the theoretical analysis of ref. [22] and section 4.1.2. Most notably, the finite slab height, with no conducting plane on top, introduces the possibility for significant out-of-plane radiative losses. Thus, it is somewhat surprising that high-quality modes were observable in the experiment at all. The field profiles in figures 4.9 and 4.10 suggest that the modes observed in the experiment are prevented by their symmetry from coupling efficiently to radiative modes, similar to the guided modes studied in chapter 3. If this is the case, then finite periodic slabs such as the one studied here can serve as mirrorless resonant cavities due to the cooperation of two effects: suppression of in-plane radiative losses due to the formation of surface avoiding modes, and suppression of out-of-plane losses due to symmetry protection.

A rigorous analysis of out-of-plane losses in the finite periodic slab, along the lines of sections 3.2.3 and 3.3, is left for future work. Here, we will briefly discuss some of the considerations required in such an analysis.

In calculating the band structure of the infinite slab, the appropriate basis functions are the guided modes of a dielectric waveguide (see section 3.2), rather than the plane wave basis used for the 2d band structure. Specifically, noting the ground plane and using image theory, the predominant resonant states should resemble the lowest order TM odd modes of a dielectric slab with thickness $2h$ and a refractive index equal to the spacial average of the figure 4.6 lattice. For guided modes within the light cone, the out-of-plane losses will require using complex eigenvalues: either complex in-plane wavevectors with real frequency, or complex frequency with real wavevectors [118, 119]. Properly calculating the guided mode dispersion relations and field profiles in the presence of radiative losses can be computationally difficult; one approach is to follow the procedures in section 3.2.3 and appendix B, modified to use a 3d computational cell.

Second, unlike in the section 3.3 symmetry analysis on the infinite 1d grating, the finite periodic slab lacks translational symmetry in the x and y directions. Thus, k_x and k_y are not good quantum numbers for the symmetry analysis, and the modes need to be represented in the point group of the overall structure. This can be seen by looking at the field

profile of mode (iii) in figure 4.9: the rapidly varying part is a superposition of modes from the K-points of the infinite crystal (C_{3v} symmetry), but mode (iii) itself belongs to the A_1 representation of the C_{6v} point group. One consequence of this is that even though surface avoiding modes will arise regardless of the boundary shape [22], finite crystals with high symmetry boundaries, such as the hexagonal boundary used here, are more likely to suppress out-of-plane radiation.

CHAPTER 5

Conclusions and Potential Applications

The coupling process by which electromagnetic resonators exchange energy with their environments can have profound effects on the transmission and reflection properties of nearby interfaces, with rapid transitions from high transmittance to high reflectance over narrow frequency ranges, and has been exploited to design useful optical components such as spectral filters and dielectric mirrors. The resonators themselves can vary widely in form, with examples including lumped capacitive-inductive circuits, metallic cavities, and dielectric shapes such as whispering-gallery cavities, each with its own range of suitable applications, frequencies, and operating conditions. Identifying new forms of resonators, and understanding how to engineer the coupling of resonators to their environment, can help make optical components more compact, simpler to manufacture, more amenable to integration in systems, and feasible in a greater range of frequencies.

This dissertation presented three electromagnetic resonators, each based on a different method of confining electromagnetic fields near the region of interest.

Chapter 2 described a resonant structure based on two parallel conducting plates, each containing a subwavelength slit. Even without side walls to confine the field, the structure supports a localized, high-quality, TE-polarized resonant mode bound to the slits, with resonant frequencies slightly below the Fabry-Pérot frequencies $f_{c,m} = mc/2d$ (where d is the plate separation and $m = 1, 2, \dots$). As a result, the structure acts as a narrowband transmission filter for TE-polarized incident light, exhibiting perfect transmission at the resonant frequencies and nearly zero transmission otherwise.

Real metals have nonradiative losses that can limit the performance of resonators with conducting walls, particularly at high frequencies. Consequently, Chapter 3 described one way to make a transmission filter using dielectric materials. Because the underlying materials are transparent, such a filter requires at least two resonant modes, with similar frequencies but very different coupling strengths to the radiative fields: the strongly coupled mode produces high resonant reflectance over a broad frequency range, and Fano interference with the weakly coupled mode produces a narrow transmission peak within this high

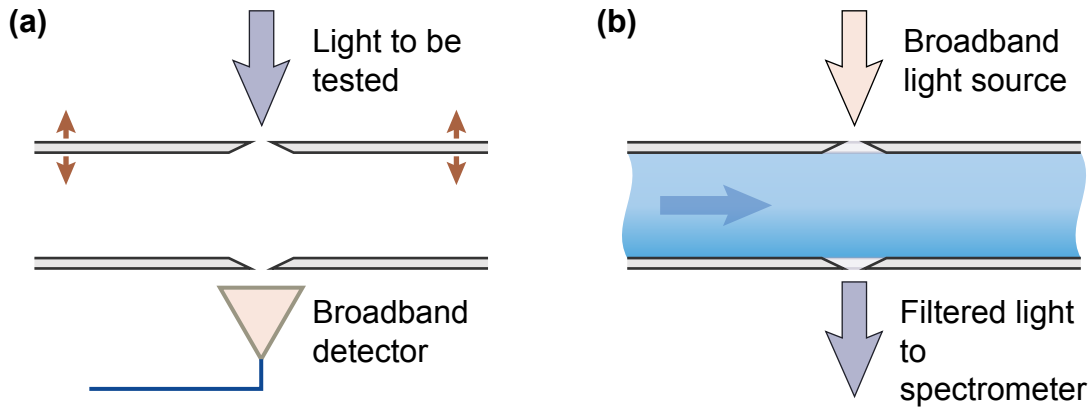

Figure 5.1: Some spectroscopic applications for the two-slit structure. (a) Precision spectrometer or transmission filter, with transmission frequency adjustable by changing the wall separation. (b) Permittivity measurement of fluids/gases. The transmitted frequency depends on the properties of the material between the walls.

reflectance background. We showed that these conditions can be met with a single-layer, high index contrast dielectric grating that supports extended resonant guided modes. In this case, the differing coupling strengths of the resonant grating-supported modes arise from their differing symmetries.

Finally, Chapter 4 demonstrated that that defect-free periodic structures of finite extent can support extended, surface-avoiding, high-quality factor resonant modes, even without mirror-like structures at the boundaries to confine electromagnetic energy.

The unique structural properties of these resonators suggest a number of possible applications, which are presented here in a somewhat speculative manner.

5.1 Spectroscopy applications of the two-slit structure

The Chapter 2 transmission filter, based on two parallel slits, resembles in some ways both a Fabry-Pérot etalon and a closed microwave cavity. The similarities and differences with these well-known structures suggest the spectroscopic applications depicted in figure 5.1.

Like with a Fabry-Pérot etalon, the resonant transmission frequencies for the two-slit structure are close to multiples of $f = c/(2nd)$, where d is the wall separation and n is the refractive index between the walls. As shown in figure 5.1(a), this property allows making a (polarization sensitive) spectrometer by adjusting the wall separation while monitoring the transmitted power. Such a spectrometer could be laterally compact compared to a Fabry-Pérot etalon, because both the relevant excitation and the resonant field are confined near the slits to a distance on the order of a wavelength (see section 2.2.3.1). In addition,

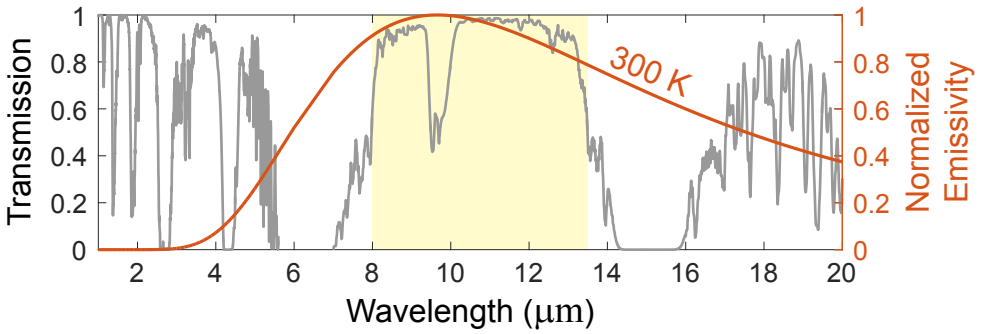

Figure 5.2: Infrared transmission through the atmosphere (gray line), calculated using [121] assuming water vapor partial pressure of 3.0 mm H_2O, courtesy Gemini Observatory. Blackbody emissivity at 300 K, from Plank's law (red line). The long-wavelength infrared window is indicated in yellow.

achieving a high-Q, narrowband response is simply a matter of decreasing the slit width, and is limited only by manufacturing tolerances and material absorption. Ref [68] showed that a compact spectrometer based on slotted plates with adjustable separation is feasible even at THz frequencies.

With a fixed wall separation, the resonant frequencies depend on the refractive index of the material between the walls. This principle has been used with traditional cavities to precisely measure the dielectric constants of various materials at microwave frequencies (*c.f.* [120]). Compared to these traditional cavities, the two-slotted structure has open boundaries at each end. As shown schematically in figure 5.1(b), this opens the possibility of monitoring a continuously flowing fluid, rather than needing to seal a fixed sample inside a closed cavity, and has possible applications such as non-invasive *in-situ* monitoring of chemical processes.

5.2 Long-wavelength infrared spectral filtering

The long-wavelength infrared (LWIR) regime spanning from approximately $8 - 14$ μm is of considerable practical importance, both because it is near the peak emissivity of a room-temperature (300 K) blackbody, and because it corresponds to a window of low absorption by water vapor and other atmospheric constituents, as shown in figure 5.2. Consequently, this wavelength range is attractive for aerial and satellite remote sensing and surveillance applications, allowing observation of objects of Earth's surface even through cloud cover [97].

At the same time, optical components that are well-developed for visible and near-IR frequencies can be unwieldy or difficult to manufacture for LWIR applications. For in-

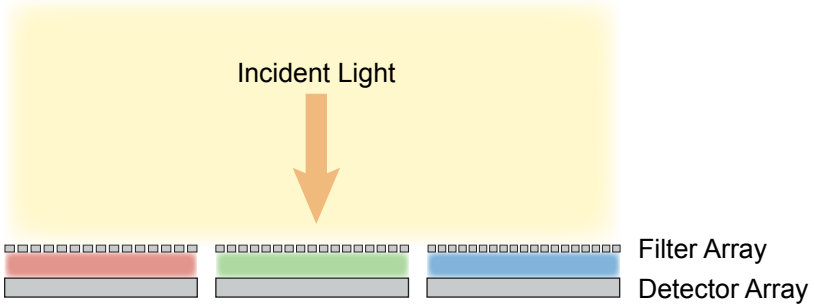

Figure 5.3: Schematic of grating-based transmission filters integrated in a focal plane array.

stance, a distributed Bragg reflector, used as a reflective surface in a Fabry-Pérot etalon, would require each sublayer to be around 1 μm thick; accurate and uniform deposition of many such layers, while avoiding non-uniformities such as curvature and surface roughness, would be problematic. In addition, many dielectric materials commonly used in the visible and near-IR (including SiO_2 and GaAs) exhibit high absorption in the LWIR due to infrared-active lattice vibrations [96].

For these reasons, resonant single-layer silicon structures, such as the high contrast grating described in Chapter 3, are especially well suited for prospective LWIR applications. In fact, the Chapter 3 grating was the first reported experimental demonstration of a single-layer transmission filter in the LWIR [20, 21], providing high transmission at the desired frequency with high reflectivity over the rest of the $8 - 14$ μm range.

The silicon grating structure allows for adjusting the transmission wavelength by changing the grating period and fill factor without changing the thickness. In addition, it is readily manufacturable using CMOS-compatible processes. Thus, it is suitable for integration in a variety of systems. Figure 5.3 shows one possible system: a focal plane array of LWIR detectors where a transmission filter is interposed in front of each detector element. This setup would be useful in hyperspectral imaging systems (*c.f.* [98]), with each spatial pixel comprising multiple sub-pixels to collect spectral data. This would allow distinguishing images of remote objects (grass, water, enemy tanks) that may have the same integrated infrared intensity but different spectral properties.

Finally, it has been suggested that selective infrared emitters/absorbers may improve the efficiency of thermal photo-voltaic (PV) devices [102, 103], which directly convert thermal radiation to electricity via the PV effect. In contrast to solar PVs, thermal PVs have the heat source much closer to the PV device and can achieve much higher power density. However, at achievable temperatures, much of the emitted radiation lies below the band gap of the PV

material and produces waste heat. Selective infrared filters placed between the heat source and PV device could improve performance by only transmitting the frequencies at which the PV device operates most efficiently, while reducing the PV device temperature.

5.3 Mirrorless cavity applications

In Chapter 4, we demonstrated that very simple periodic structures can confine extended cavity-like modes even without mirror-like reflecting boundaries. Achieving three-dimensional electromagnetic confinement in quasi-2d structures is highly desirable, with applications including surface-emitting lasers [122]. Consequently, much effort has been extended in devising structures to achieve both vertical and lateral confinement (*e.g.*, [37, 106, 123–125]). Recognizing that complicated structures are not always necessary may enable resonant cavity designs that are simpler and cheaper to manufacture a large scale (although at a likely cost of lower quality factors for a given volume).

Interestingly, many of the resonant surface avoiding modes identified in figures 4.9 and 4.10 have a significant portion of their field energy located in the air surrounding the dielectric rods. This suggests that a laser might be created by filling this empty space with a suitable gain medium. Alternatively, it may be possible to incorporate a gain medium into the pillars themselves in the form of quantum dots [126, 127]. The high quality factor of the fundamental surface avoiding modes (those nearest the band edges) relative to higher order modes suggests that single-mode lasing will be achievable in mirrorless finite periodic structures.

APPENDIX A

Generalized Network Parameters for the Two-Slit Transmission Problem

A.1 Calculation procedure

This appendix details the calculation of the TE generalized admittance matrix elements of eq. 2.8:

$$\begin{aligned} Y_{qq}^{p1} &= -\left\langle \boldsymbol{M_{q1}}, \boldsymbol{H_t^p}(\boldsymbol{M_{q1}}) \right\rangle_q \\ Y_{qr}^{b1} &= \left\langle \boldsymbol{M_{q1}}, \boldsymbol{H_t^p}(\boldsymbol{M_{r1}}) \right\rangle_q , \qquad q \neq r \end{aligned} \tag{A.1}$$

where the inner product over a slit is defined by eq. 2.5:

$$\left\langle \boldsymbol{A}, \boldsymbol{B} \right\rangle_q = \int_{s_q-\Delta_q}^{s_q+\Delta_q} \boldsymbol{A} \cdot \boldsymbol{B} \, \mathrm{d}x \, , \qquad q = 1, 2 \tag{A.2}$$

and the magnetic current in the slit is given by the lowest order TE mode of eq. 2.6:

$$\boldsymbol{M_{q1}} = \hat{\boldsymbol{x}} \sqrt{\Delta_q^2 - (x - s_q)^2} \tag{A.3}$$

First, the magnetic field due to a slit magnetic current of the form (A.3) is found for each of the three equivalence regions of figure 2.2a. This will involve the following 2d expression for the magnetic field due to a magnetic current sheet radiating in free space, assuming $e^{-i\omega t}$ time dependence [63]:

$$\boldsymbol{H} = \frac{-k}{4\eta} \int_s \boldsymbol{M} H_0^{(1)}(k\rho) \, \mathrm{d}s + \frac{1}{4\eta} \int_s (\nabla \cdot \boldsymbol{M}) \hat{\rho} H_1^{(1)}(k\rho) \, \mathrm{d}s \tag{A.4}$$

In eq. A.4, k is the wavevector magnitude, $\eta = \sqrt{\mu/\epsilon}$ is the impedance, $\hat{\rho}$ is the unit vector pointing from the source point to the observation point, and ρ is the distance between the

source and observation points. $H_0^{(1)}$ and $H_1^{(1)}$ are Hankel functions of zero and first order, respectively.

The magnetic field is then used in eq. A.1 to calculate each matrix element.

A.2 Derivation of generalized admittances

A.2.1 Region A

In region A with slit 1 shorted, the magnetic field due to $\boldsymbol{M_1}$ is the same as $2\boldsymbol{M_1}$ located at $z = 0$ and radiating in free space. Using $\boldsymbol{M_{11}} = \hat{\boldsymbol{x}}\sqrt{\Delta_1^2 - x^2}$,

$$\begin{aligned}\boldsymbol{H^a}(\boldsymbol{M_{11}}) =& \frac{-\hat{\boldsymbol{x}}k_a}{2\eta_a}\int_{-\Delta_1}^{\Delta_1}\sqrt{\Delta_1^2 - x'^2}H_0^{(1)}(k_a\sqrt{(x-x')^2+z^2})\,\mathrm{d}x' \\ &+ \frac{\hat{\boldsymbol{x}}}{2\eta_a}\int_{-\Delta_1}^{\Delta_1}\frac{-x'}{\sqrt{\Delta_1^2 - x'^2}}\frac{(x-x')}{\sqrt{(x-x')^2+z^2}}H_1^{(1)}(k_a\sqrt{(x-x')^2+z^2})\,\mathrm{d}x' \\ &+ \frac{\hat{\boldsymbol{z}}}{2\eta_a}\int_{-\Delta_1}^{\Delta_1}\frac{-x'}{\sqrt{\Delta_1^2 - x'^2}}\frac{z}{\sqrt{(x-x')^2+z^2}}H_1^{(1)}(k_a\sqrt{(x-x')^2+z^2})\,\mathrm{d}x'\end{aligned} \tag{A.5}$$

We then have,

$$\begin{aligned}Y_{11}^{a1} =& -\langle \boldsymbol{M_{11}}, \boldsymbol{H_t^a}(\boldsymbol{M_{11}})\rangle_1 = -\int_{-\Delta_1}^{\Delta_1}\boldsymbol{M_{11}}\cdot\boldsymbol{H_t^a}(\boldsymbol{M_{11}})\,\mathrm{d}x \\ =& \frac{k_a}{2\eta_a}\int_{-\Delta_1}^{\Delta_1}\int_{-\Delta_1}^{\Delta_1}\sqrt{\Delta_1^2 - x^2}\sqrt{\Delta_1^2 - x'^2}H_0^{(1)}(k_a|x-x'|)\,\mathrm{d}x'\,\mathrm{d}x \\ &+ \frac{1}{2\eta_a}\int_{-\Delta_1}^{\Delta_1}\int_{-\Delta_1}^{\Delta_1}\frac{\sqrt{\Delta_1^2 - x^2}}{\sqrt{\Delta_1^2 - x'^2}}\frac{x'(x-x')}{|x-x'|}H_1^{(1)}(k_a|x-x'|)\,\mathrm{d}x'\,\mathrm{d}x\end{aligned} \tag{A.6}$$

To simplify these integrals, we will consider small argument approximations for the Hankel functions. Since $x, x' \in \{-\Delta_1, \Delta_1\}$ and $k_a\Delta_1 \ll 1$ we can use the approximation [67]

$$H_0^{(1)}(k_a|x-x'|) \simeq 1 + i\frac{2}{\pi}\ln\left(\frac{\gamma k_a|x-x'|}{2}\right), \tag{A.7}$$

where $\gamma = 1.7810724...$ is the exponential of the Euler-Mascheroni constant. We can then use the fact that [66]

$$\int_{-\Delta}^{\Delta}\sqrt{\Delta^2 - x'^2}\ln\left(\frac{\gamma k_a|x-x'|}{2}\right)\mathrm{d}x' = \frac{\pi\Delta^2}{2}\ln\left(\frac{\alpha k_a\Delta}{2\pi}\right) + \frac{\pi x^2}{2}, \tag{A.8}$$

where $\alpha = 1.69691505...$, as well as the following integral relations [128]:

$$\begin{aligned}
\int_{-\Delta}^{\Delta} \sqrt{\Delta^2 - x^2}\, \mathrm{d}x &= \frac{\pi \Delta^2}{2} \\
\int_{-\Delta}^{\Delta} \frac{x^2}{\sqrt{\Delta^2 - x^2}}\, \mathrm{d}x &= \frac{\pi \Delta^2}{2} \\
\int_{-\Delta}^{\Delta} x\sqrt{\Delta^2 - x^2}\, \mathrm{d}x &= 0 \\
\int_{-\Delta}^{\Delta} x^2\sqrt{\Delta^2 - x^2}\, \mathrm{d}x &= \frac{\pi \Delta^4}{8}
\end{aligned} \tag{A.9}$$

Using these relations, the first integral in eq. (A.6) becomes:

$$\begin{aligned}
\frac{k_a}{2\eta_a} \int_{-\Delta_1}^{\Delta_1} \int_{-\Delta_1}^{\Delta_1} \sqrt{\Delta_1^2 - x^2}\sqrt{\Delta_1^2 - x'^2} H_0^{(1)}(k_a|x - x'|)\, \mathrm{d}x'\, \mathrm{d}x \simeq \\
\frac{\pi^2 k_a \Delta_1^4}{8\eta_a} + i\frac{\pi k_a \Delta_1^4}{4\eta_a}\left[\ln\left(\frac{\alpha k_a \Delta_1}{2\pi}\right) + \frac{1}{4}\right]
\end{aligned} \tag{A.10}$$

To simplify the second integral in eq. (A.6), we can use the small argument approximation [67]:

$$H_1^{(1)}(k_a|x - x'|) \simeq \frac{k_a|x - x'|}{2} - i\frac{2}{\pi}\frac{1}{k_a|x - x'|}, \tag{A.11}$$

So that the second integral becomes

$$\begin{aligned}
\frac{1}{2\eta_a} \int_{-\Delta_1}^{\Delta_1} \int_{-\Delta_1}^{\Delta_1} \frac{\sqrt{\Delta_1^2 - x^2}}{\sqrt{\Delta_1^2 - x'^2}} \frac{x'(x - x')}{|x - x'|} H_1^{(1)}(k_a|x - x'|)\, \mathrm{d}x'\, \mathrm{d}x \simeq \\
\frac{1}{2\eta_a} \int_{-\Delta_1}^{\Delta_1} \int_{-\Delta_1}^{\Delta_1} \frac{\sqrt{\Delta_1^2 - x^2}}{\sqrt{\Delta_1^2 - x'^2}} \left[\frac{k_a x'(x - x')}{2} - i\frac{2x'}{\pi k_a (x - x')}\right] \mathrm{d}x'\, \mathrm{d}x
\end{aligned} \tag{A.12}$$

The first term is easily evaluated using the relations in eq. (A.9). The second term has a singularity at $x = x'$, which we can deal with by adding a small imaginary part to x' and using the Sokhotski-Plemelj theorem [129] (p.v. denotes the Cauchy principal value):

$$\lim_{\epsilon \to 0^+} \frac{1}{x - (x' \pm i\epsilon)} = \text{p.v.}\frac{1}{x - x'} \pm i\pi\delta(x - x') \tag{A.13}$$

Giving for the second term in eq. (A.12),

$$\frac{-i}{\pi\eta k_a}\int_{-\Delta_1}^{\Delta_1}\left[\text{p.v.}\int_{-\Delta_1}^{\Delta_1} x\frac{x'}{x-x'}\frac{\sqrt{\Delta_1^2-x^2}}{\sqrt{\Delta_1^2-x'^2}}\,\mathrm{d}x - i\pi\int_{-\Delta_1}^{\Delta_1}\frac{\sqrt{\Delta_1^2-x^2}}{\sqrt{\Delta_1^2-x'^2}}x'\delta(x-x')\,\mathrm{d}x\right]\mathrm{d}x'$$
$$= \frac{-i}{\pi\eta k_a}\int_{-\Delta_1}^{\Delta_1}\left[\frac{-\pi x'^2}{\sqrt{\Delta_1^2-x'^2}} - i\pi x'\right]\mathrm{d}x' = \frac{i\pi\Delta_1^2}{2\eta k_a} \quad \text{(A.14)}$$

Thus,

$$\frac{1}{2\eta_a}\int_{-\Delta_1}^{\Delta_1}\int_{-\Delta_1}^{\Delta_1}\frac{\sqrt{\Delta_1^2-x^2}}{\sqrt{\Delta_1^2-x'^2}}\left[\frac{k_a x'(x-x')}{2} - i\frac{2x'}{\pi k_a(x-x')}\right]\mathrm{d}x'\,\mathrm{d}x$$
$$= \frac{-k_a\pi^2\Delta_1^4}{16\eta_a} + i\frac{\pi\Delta_1^2}{2\eta_a k_a} \quad \text{(A.15)}$$

Combining eqs. (A.10) and (A.15) gives Y_{11}^{a1} in the small argument approximation:

$$Y_{11}^{a1} \simeq \frac{\pi^2 k_a\Delta_1^4}{16\eta_a} + i\frac{\pi k_a\Delta_1^4}{4\eta_a}\left[\ln\left(\frac{\alpha k_a\Delta_1}{2\pi}\right)+\frac{1}{4}\right] + i\frac{\pi\Delta_1^2}{2\eta_a k_a} \quad \text{(A.16)}$$

A.2.2 Region B

After shorting slits 1 and 2, the magnetic field in region B due to $\boldsymbol{M_1}$ is the same as the radiation in free space from $2\boldsymbol{M_1}$ and its images at $z = 2nd$, with $n = 0, \pm1, \pm2, ...$:

$$\begin{aligned}\boldsymbol{H^b}(\boldsymbol{M_{11}}) =& \frac{-\hat{\boldsymbol{x}}k_b}{2\eta_b}\sum_{n=-\infty}^{\infty}\int_{-\Delta_1}^{\Delta_1}\sqrt{\Delta_1^2-x'^2}H_0^{(1)}(k_b\sqrt{(x-x')^2+(z-2nd)^2})\,\mathrm{d}x' \\ &+ \frac{\hat{\boldsymbol{x}}}{2\eta_b}\sum_{n=-\infty}^{\infty}\int_{-\Delta_1}^{\Delta_1}\frac{-x'}{\sqrt{\Delta_1^2-x'^2}}\frac{(x-x')}{\sqrt{(x-x')^2+(z-2nd)^2}} \\ &\qquad\times H_1^{(1)}(k_b\sqrt{(x-x')^2+(z-2nd)^2})\,\mathrm{d}x' \\ &+ \frac{\hat{\boldsymbol{z}}}{2\eta_b}\sum_{n=-\infty}^{\infty}\int_{-\Delta_1}^{\Delta_1}\frac{-x'}{\sqrt{\Delta_1^2-x'^2}}\frac{z-2nd}{\sqrt{(x-x')^2+(z-2nd)^2}} \\ &\qquad\times H_1^{(1)}(k_b\sqrt{(x-x')^2+(z-2nd)^2})\,\mathrm{d}x'\end{aligned} \quad \text{(A.17)}$$

$$
\begin{aligned}
Y_{11}^{b1} =& -\left\langle \boldsymbol{M_{11}}, \boldsymbol{H_t^b}(\boldsymbol{M_{11}}) \right\rangle_1 = -\int_{-\Delta_1}^{\Delta_1} \boldsymbol{M_{11}} \cdot \boldsymbol{H_t^b}(\boldsymbol{M_{11}})\,\mathrm{d}x \\
=& \frac{k_b}{2\eta_b} \sum_{n=-\infty}^{\infty} \int_{-\Delta_1}^{\Delta_1}\int_{-\Delta_1}^{\Delta_1} \sqrt{\Delta_1^2 - x^2}\sqrt{\Delta_1^2 - x'^2}\, s H_0^{(1)}(k_b\sqrt{(x-x')^2 + (2nd)^2})\,\mathrm{d}x'\,\mathrm{d}x \\
&+ \frac{1}{2\eta_b} \sum_{n=-\infty}^{\infty} \int_{-\Delta_1}^{\Delta_1}\int_{-\Delta_1}^{\Delta_1} \frac{\sqrt{\Delta_1^2 - x^2}}{\sqrt{\Delta_1^2 - x'^2}} \frac{x'(x-x')}{\sqrt{(x-x')^2 + (2nd)^2}} \\
&\qquad\qquad \times H_1^{(1)}(k_b\sqrt{(x-x')^2 + (2nd)^2})\,\mathrm{d}x'\,\mathrm{d}x
\end{aligned} \tag{A.18}
$$

To simplify these integrals, we will consider the following approximations. First, for $n = 0$, the small argument approximation can be used as it was for Y_{11}^a. Second, if $n^2 > (10\Delta_1/d)^2$, then $(2nd)^2 \gg (x-x')^2$ for $x, x' \in \{-\Delta_1, \Delta_1\}$. Thus $H_\nu^{(1)}(k_b\sqrt{(x-x')^2 + (2nd)^2}) \simeq H_\nu^{(1)}(k_b|2nd|)$, allowing the Hankel functions to be taken outside the integrals, along with the denominator of the second integral. Using these approximations in eq. (A.18) yields:

$$
\begin{aligned}
Y_{11}^{b1} \simeq& \frac{\pi^2 k_b \Delta_1^4}{16\eta_b} + i\frac{\pi k_b \Delta_1^4}{4\eta_b}\left[\ln\left(\frac{\alpha k_b \Delta_1}{2\pi}\right) + \frac{1}{4}\right] + i\frac{\pi\Delta_1^2}{2\eta_b k_b} \\
&+ \frac{k_b}{\eta_b} \sum_{n=1}^{N_1} \int_{-\Delta_1}^{\Delta_1}\int_{-\Delta_1}^{\Delta_1} \sqrt{\Delta_1^2 - x^2}\sqrt{\Delta_1^2 - x'^2}\, H_0^{(1)}(k_b\sqrt{(x-x')^2 + (2nd)^2})\,\mathrm{d}x'\,\mathrm{d}x \\
&+ \frac{1}{\eta_b} \sum_{n=1}^{N_1} \int_{-\Delta_1}^{\Delta_1}\int_{-\Delta_1}^{\Delta_1} \frac{\sqrt{\Delta_1^2 - x^2}}{\sqrt{\Delta_1^2 - x'^2}} \frac{x'(x-x')}{\sqrt{(x-x')^2 + (2nd)^2}} \\
&\qquad\qquad \times H_1^{(1)}(k_b\sqrt{(x-x')^2 + (2nd)^2})\,\mathrm{d}x'\,\mathrm{d}x \\
&+ \sum_{n=N_1+1}^{\infty} \left[\frac{\pi^2\Delta_1^4 k_b}{4\eta_b}\left(H_0^{(1)}(2k_b nd) - \frac{H_1^{(1)}(2k_b nd)}{2k_b nd}\right)\right]
\end{aligned} \tag{A.19}
$$

Here, N_1 is the largest integer n such that $n^2 \le (10\Delta_1/d)^2$.

The magnetic field in region B due to $\boldsymbol{M_2}$ is the same as the radiation in free space

from $2\boldsymbol{M_2}$ and its images at $z = (2n-1)d$, with $n = 0, \pm1, \pm2, ...$:

$$\begin{aligned}\boldsymbol{H^b}(\boldsymbol{M_{21}}) =& \frac{-\hat{\boldsymbol{x}}k_b}{2\eta_b}\sum_{n=-\infty}^{\infty}\int_{s_2-\Delta_2}^{s_2+\Delta_2}\sqrt{\Delta_2^2-(x'-s_2)^2}H_0^{(1)}(k_b\sqrt{(x-x')^2+[z-(2n-1)d]^2})\,\mathrm{d}x' \\ &+\frac{\hat{\boldsymbol{x}}}{2\eta_b}\sum_{n=-\infty}^{\infty}\int_{s_2-\Delta_2}^{s_2+\Delta_2}\frac{-(x'-s_2)}{\sqrt{\Delta_2^2-(x'-s_2)^2}}\frac{(x-x')}{\sqrt{(x-x')^2+[z-(2n-1)d]^2}} \\ &\qquad\times H_1^{(1)}(k_b\sqrt{(x-x')^2+[z-(2n-1)d]^2})\,\mathrm{d}x' \\ &+\frac{\hat{\boldsymbol{z}}}{2\eta_b}\sum_{n=-\infty}^{\infty}\int_{s_2-\Delta_2}^{s_2+\Delta_2}\frac{-(x'-s_2)}{\sqrt{\Delta_2^2-(x'-s_2)^2}}\frac{z-(2n-1)d}{\sqrt{(x-x')^2+z^2}} \\ &\qquad\times H_1^{(1)}(k_b\sqrt{(x-x')^2+(z-2nd)^2})\,\mathrm{d}x'\end{aligned} \tag{A.20}$$

$$\begin{aligned}Y_{12}^{b1} =& \left\langle \boldsymbol{M_{11}}, \boldsymbol{H_t^b}(\boldsymbol{M_{21}})\right\rangle_1 = \int_{-\Delta_1}^{\Delta_1}\boldsymbol{M_{11}}\cdot\boldsymbol{H_t^b}(\boldsymbol{M_{21}})\,\mathrm{d}x \\ =& -\frac{k_b}{2\eta_b}\sum_{n=-\infty}^{\infty}\int_{-\Delta_1}^{\Delta_1}\int_{s_2-\Delta_2}^{s_2+\Delta_2}\sqrt{\Delta_1^2-x^2}\sqrt{\Delta_2^2-(x'-s_2)^2} \\ &\qquad\times H_0^{(1)}(k_b\sqrt{(x-x')^2+[(2n-1)d]^2})\,\mathrm{d}x'\,\mathrm{d}x \\ &-\frac{1}{2\eta_b}\sum_{n=-\infty}^{\infty}\int_{-\Delta_1}^{\Delta_1}\int_{s_2-\Delta_2}^{s_2+\Delta_2}\frac{\sqrt{\Delta_1^2-x^2}}{\sqrt{\Delta_2^2-(x'-s_2)^2}}\frac{(x'-s_2)(x-x')}{\sqrt{(x-x')^2+[(2n-1)d]^2}} \\ &\qquad\times H_1^{(1)}(k_b\sqrt{(x-x')^2+[(2n-1)d]^2})\,\mathrm{d}x'\,\mathrm{d}x\end{aligned} \tag{A.21}$$

If $(2n-1)^2 > (10(\Delta_1+\Delta_2)/d)^2$, then $\sqrt{(x-x')^2+[(2n-1)d]^2} \simeq \sqrt{s_2^2+[(2n-1)d]^2}$ for $x \in \{-\Delta_1, \Delta_1\}$ and $x' \in \{s_2-\Delta_2, s_2+\Delta_2\}$, allowing us to take these expressions

outside the integrals. Thus eq. (A.21) can be approximated as:

$$
\begin{aligned}
Y_{12}^{b1} \simeq & -\frac{k_b}{2\eta_b}\sum_{n=1}^{N_{12}}\int_{-\Delta_1}^{\Delta_1}\int_{s_2-\Delta_2}^{s_2+\Delta_2}\sqrt{\Delta_1^2-x^2}\sqrt{\Delta_2^2-(x'-s_2)^2} \\
& \qquad \times H_0^{(1)}(k_b\sqrt{(x-x')^2+[(2n-1)d]^2})\,\mathrm{d}x'\,\mathrm{d}x \\
& -\frac{1}{2\eta_b}\sum_{n=1}^{N_{12}}\int_{-\Delta_1}^{\Delta_1}\int_{s_2-\Delta_2}^{s_2+\Delta_2}\frac{\sqrt{\Delta_1^2-x^2}}{\sqrt{\Delta_2^2-(x'-s_2)^2}}\frac{(x'-s_2)(x-x')}{\sqrt{(x-x')^2+[(2n-1)d]^2}} \\
& \qquad \times H_1^{(1)}(k_b\sqrt{(x-x')^2+[(2n-1)d]^2})\,\mathrm{d}x'\,\mathrm{d}x \\
& +\sum_{n=N_{12}+1}^{\infty}\left[\frac{\pi^2\Delta_1^2\Delta_2^2k_b}{4\eta_b}\left(-H_0^{(1)}(k_b\sqrt{s_2^2+[(2n-1)d]^2})+\frac{H_1^{(1)}(k_b\sqrt{s_2^2+[(2n-1)d]^2})}{k_b\sqrt{s_2^2+[(2n-1)d]^2}}\right)\right]
\end{aligned}
\tag{A.22}
$$

Here, N_{12} is the largest integer n such that $(2n-1)^2 \leq (10(\Delta_1+\Delta_2)/d)^2$.

By reciprocity, we have $Y_{21}^{b1} = Y_{12}^{b1}$. Finally, Y_{22}^{b1} can be obtained using similar procedures to those above, giving:

$$
\begin{aligned}
Y_{22}^{b1} \simeq & \frac{\pi^2k_b\Delta_2^4}{16\eta_b}+i\frac{\pi k_b\Delta_2^4}{4\eta_b}\left[\ln\left(\frac{\alpha k_b\Delta_2}{2\pi}\right)+\frac{1}{4}\right]+i\frac{\pi\Delta_2^2}{2\eta_bk_b} \\
& +\frac{k_b}{\eta_b}\sum_{n=1}^{N_2}\int_{-\Delta_2}^{\Delta_2}\int_{-\Delta_1}^{\Delta_2}\sqrt{\Delta_2^2-x^2}\sqrt{\Delta_2^2-x'^2}H_0^{(1)}(k_b\sqrt{(x-x')^2+(2nd)^2})\,\mathrm{d}x'\,\mathrm{d}x \\
& +\frac{1}{\eta_b}\sum_{n=1}^{N_2}\int_{-\Delta_2}^{\Delta_2}\int_{-\Delta_2}^{\Delta_2}\frac{\sqrt{\Delta_2^2-x^2}}{\sqrt{\Delta_2^2-x'^2}}\frac{x'(x-x')}{\sqrt{(x-x')^2+(2nd)^2}}H_1^{(1)}(k_b\sqrt{(x-x')^2+(2nd)^2})\,\mathrm{d}x'\,\mathrm{d}x \\
& +\sum_{n=N_2+1}^{\infty}\left[\frac{\pi^2\Delta_2^4k_b}{4\eta_b}\left(H_0^{(1)}(2k_bnd)-\frac{H_1^{(1)}(2k_bnd)}{2k_bnd}\right)\right]
\end{aligned}
\tag{A.23}
$$

where N_2 is the largest integer n such that $n^2 \leq (10\Delta_2/d)^2$.

A.2.3 Region C

Y_{22}^{c1} can be obtained using a similar procedure to that for Y_{11}^{a1} (eq. A.16), giving

$$
Y_{22}^{c1} \simeq \frac{\pi^2k_c\Delta_2^4}{16\eta_c}+i\frac{\pi k_c\Delta_2^4}{4\eta_c}\left[\ln\left(\frac{\alpha k_c\Delta_2}{2\pi}\right)+\frac{1}{4}\right]+i\frac{\pi\Delta_2^2}{2\eta_ck_c} \tag{A.24}
$$

A.3 Computation of the Infinite Sums

The expressions for the generalized admittances in Region B—eqs. A.19, A.22, and A.23—contain infinite sums involving Hankel functions of the first and second kinds. These sums converge quite slowly, particularly near the singularities at the waveguide cut-off frequencies, $k_b = m\pi/d$, with $m = 1, 2, ...$ Computing these sums numerically can therefore be time-intensive and is susceptible to accumulated numerical round-off errors affecting the final computed transmissivity. Fortunately, we can dramatically improve the numerical performance by recasting the infinite sums in terms of polylogarithm functions, as described below.

Consider the last term in eq. A.19, containing the infinite sum:

$$S = \sum_{n=N_1+1}^{\infty} \left[H_0^{(1)}(nz) - \frac{H_1^{(1)}(nz)}{nz} \right] \tag{A.25}$$

For simplicity, we've made the substitution $z = 2k_b d$ and omitted the leading constants. For some N_{max}, we can replace the terms with $n > N_{max}$ with their asymptotic forms [67]:

$$\begin{aligned} H_0^{(1)}(nz) \simeq & \sqrt{\frac{2}{\pi nz}} \exp\left[i\left(nz - \frac{\pi}{4} \right) \right] \\ H_1^{(1)}(nz) \simeq & \sqrt{\frac{2}{\pi nz}} \exp\left[i\left(nz - \frac{3\pi}{4} \right) \right] \end{aligned} \tag{A.26}$$

Now the sum can be rewritten as:

$$\begin{aligned} S \simeq & \sum_{n=N_1+1}^{N_{max}} \left[H_0^{(1)}(nz) - \frac{H_1^{(1)}(nz)}{nz} \right] \\ & - \sum_{n=1}^{N_{max}} \sqrt{\frac{2}{\pi}} \left[\exp\left(\frac{-i\pi}{4} \right) \frac{\exp(inz)}{\sqrt{nz}} - \exp\left(\frac{-i3\pi}{4} \right) \frac{\exp(inz)}{(nz)^{3/2}} \right] \\ & + \sum_{n=1}^{\infty} \sqrt{\frac{2}{\pi}} \exp\left(\frac{-i\pi}{4} \right) \frac{\exp(inz)}{\sqrt{nz}} \\ & - \sum_{n=1}^{\infty} \sqrt{\frac{2}{\pi}} \exp\left(\frac{-i3\pi}{4} \right) \frac{\exp(inz)}{(nz)^{3/2}} \end{aligned} \tag{A.27}$$

The first two terms here are just finite sums that can be computed numerically, and the last

two terms can be written in terms of the polylogarithm function:

$$\mathrm{Li}_\nu(z) = \sum_{k=1}^{\infty} \frac{z^k}{k^\nu} \tag{A.28}$$

Thus, eq. A.27 becomes:

$$\begin{aligned} S \simeq & \sum_{n=N_1+1}^{N_{max}} \left[H_0^{(1)}(nz) - \frac{H_1^{(1)}(nz)}{nz} \right] \\ & - \sum_{n=1}^{N_{max}} \sqrt{\frac{2}{\pi}} \left[\exp\left(\frac{-i\pi}{4}\right) \frac{\exp(inz)}{\sqrt{nz}} - \exp\left(\frac{-i3\pi}{4}\right) \frac{\exp(inz)}{(nz)^{3/2}} \right] \\ & + \sqrt{\frac{2}{\pi}} \left[\frac{\mathrm{Li}_{1/2}(e^{iz})}{\sqrt{z}} - \frac{\mathrm{Li}_{3/2}(e^{iz})}{z^{3/2}} \right] \end{aligned} \tag{A.29}$$

where, again, $z = 2k_b d$. The computations in this dissertation used $N_{max} = 200$. So what is needed are polylogarithms of half-integer order with arguments on the complex unit circle. These functions are available in computer math tools such as Wolfram Mathematica. For this dissertation, the polylogarithms were precomputed and tabulated using Mathematica.

APPENDIX B

Eigenvalue Method for the Periodic Slab Modal Analysis

This appendix describes our method for finding the dispersion relations and field profiles of the guided resonant modes in the high-contrast dielectric grating structure discussed in section 3.2.3. Figure B.1 shows the geometry being considered.

Many techniques are available for finding the modes of photonic crystals. In addition to finite difference time domain (FDTD) or finite element method (FEM) solvers that directly solve Maxwell's equations with carefully chosen sources to excite the modes, efficient eigenmode solvers are also available, including the MIT Photonic Bands software, which expands the fields as definite-frequency states in a trunctated plane wave basis [116, 130, 131]. However, complications arise in the case of photonic crystal slabs such as the grating in figure B.1, because within the light cone the guided modes are no longer true eigenmodes of the slab with definite frequency, but rather resonant states that extend infinitely (if weakly) away from the slab and exchange energy with the radiative continuum. When using the generally available solvers, it can be difficult to distinguish the states that arise from guided modes from the states of the radiative continuum, so frequently the solvers are used only for results outside the light cone [72]. This issue becomes more acute with high-contrast, one-dimensional slabs such as the one considered here.

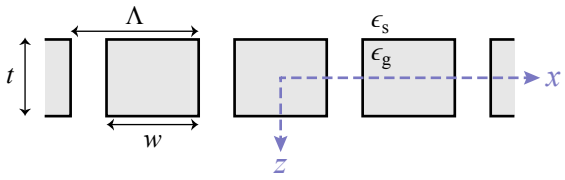

Figure B.1: Geometry of a high-contrast periodic dielectric slab, with thickness t and period Λ. Each period consists of a dielectric region of width w and permittivity ϵ_g, followed by a gap with the same permittivity as the surrounding material ϵ_s.

Because our interest is in the leaky resonant states within the light cone, we adapted a FEM approach developed by Davanco, Fietz, Urzhumov, and Shvets for finding complex-wavevector modes in 2d [94] and 3d [132] dispersive crystals, such as plasmonic crystals. Parisi *et al.* have also used the method to analyze plasmonic gratings and slabs [95]. The general approach is to cast the Helmholtz equation as a quadratic eigenvalue equation for (complex-valued) $\boldsymbol{k}$, which can be solved using the finite element method at a given frequency ω.

For TM polarization, the equation to solve is:

$$\nabla \times \frac{1}{\epsilon} \nabla \times \boldsymbol{H} - \omega^2 \mu \boldsymbol{H} = 0 \tag{B.1}$$

which can be written in the weak form:

$$\int_\Omega \boldsymbol{v} \cdot \left[\nabla \times \frac{1}{\epsilon} \nabla \times \boldsymbol{H} - \omega^2 \mu \boldsymbol{H} \right] d^3 r = 0 \tag{B.2}$$

where $\boldsymbol{v}$ is a test function. We consider the periodic 2d case with propagation along the slab ($\boldsymbol{k} = k_x \hat{\boldsymbol{x}}$) and rewrite $\boldsymbol{H} = H_y \hat{\boldsymbol{y}}$ as:

$$H_y(x, z; k_x) = e^{-ik_x x} u(x, z) \tag{B.3}$$

Here, $u(x, z)$ is a periodic function in the x direction with period Λ. Note that, in contrast to the rest of this dissertation, we are using the $e^{i\omega t}$ time-dependence convention for consistency with the COMSOL Multiphysics FEM solver. Eq. B.2 becomes:

$$\int_\Omega d^2 r \left[k_x^2 \frac{uv}{\epsilon_{zz}} + \frac{ik_x}{\epsilon_{zz}} \left(\frac{\partial u}{\partial x} v - u \frac{\partial v}{\partial x} \right) + \frac{\partial u}{\partial z} \frac{\partial v}{\partial z} \frac{1}{\epsilon_{xx}} + \frac{\partial u}{\partial x} \frac{\partial v}{\partial x} \frac{1}{\epsilon_{zz}} - \left(\frac{\omega}{c} \right)^2 uv \mu_{zz} \right] = 0 \tag{B.4}$$

where v is a test function, and ϵ_{ii} (μ_{ii}) are components of the permittivity (permeability) tensor (assumed here to be diagonal). Given ω, eq. B.4 is a quadratic eigenvalue equation for (complex-valued) k_x. The real part of k_x gives the familiar in-plane wavevector within the first Brillouin zone, while the imaginary part gives the decay due to coupling to the radiative continuum. With a solution $(u(x, z), k_x)$, the fields can be reconstructed using the

following equations:

$$\begin{aligned} H_y =& u e^{-ik_x x} \\ E_x =& \frac{ic}{\omega\epsilon}\frac{\partial u}{\partial z} e^{-ik_x x} \\ E_z =& -\left[\frac{ic}{\omega\epsilon}\frac{\partial u}{\partial z} + \frac{ck_x}{\omega\epsilon} u\right] e^{-ik_x x} \end{aligned} \tag{B.5}$$

We implemented this eigenvalue equation using the commercial FEM solver, COMSOL Multiphysics 3.5. Figure B.2a shows the simulated unit cell. The boundaries at $x = \pm\Lambda/2$ are subject to Floquet periodicity conditions, with $u(\Lambda/2, z) = u(-\Lambda/2, z)\exp(-k_x\Lambda)$. At the ends of the cell in the $\pm z$ directions, perfectly matched layers (PML) are used to simulate radiative boundaries by absorbing incident plane waves. The PML are implemented as graded anisotropic absorbers [133], with the permittivity and permeability tensors defined as:

$$\bar{\bar{\epsilon}}\,(\bar{\bar{\mu}}) = \begin{pmatrix} \epsilon_{xx}\,(\mu_{xx}) & 0 \\ 0 & \epsilon_{zz}\,(\mu_{zz}) \end{pmatrix} = \begin{pmatrix} \alpha - i\beta & 0 \\ 0 & (\alpha - i\beta)^{-1} \end{pmatrix} \tag{B.6}$$

where α is the real part of the adjacent permittivity (permeability) and:

$$\beta = \bar{\sigma}\frac{|(z \pm |z_0|)|^2}{t_{\text{PML}}^n} \tag{B.7}$$

Equation B.7 contains a number of adjustable parameters. The following values gave good results for this geometry: $\bar{\sigma} = 1.5$, $n = 2$, $z_0 = t_{\text{air}}/2 = 26\Lambda$ (the start coordinate of the PML), $t_{\text{PML}} = 5\Lambda$ (the length of the PML).

The solver generally finds many solutions to eq. B.4, many of which correspond to guided resonant states and look like the example in figure B.2b. However, there are also many spurious solutions, as in B.2c, for which the electromagnetic energy is concentrated in the PML layers or in the air layer beween the slab and PMLs. To help distinguish the desired solutions from the spurious solutions, we calculated a metric related to the concentration of energy near the dielectric slab:

$$S = \left(\int_\Omega |u|^2 z^2 d^2 r\right) \Big/ \left(\int_\Omega |u|^2 d^2 r\right) \tag{B.8}$$

Solutions with smaller values of S are more likely to be the guided modes we are looking for. Figure B.3 shows a sample TM dispersion diagram obtained by running the eigenmode solver at several frequencies and highlighting the solutions with relatively small S values.

TE solutions can be found by similar means using duality relations, making the replace-

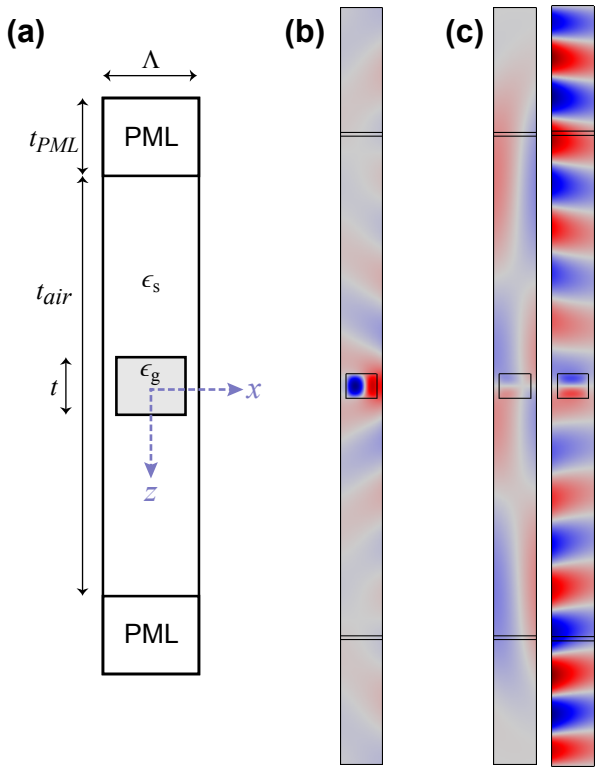

Figure B.2: (a) Schematic of simulated unit cell. (b) Representative TM solution showing H_y for a resonant guided mode. (c) Examples of spurious solutions that do not represent resonant guided modes.

ments $\boldsymbol{E} \rightarrow \boldsymbol{H}$, $\boldsymbol{H} \rightarrow -\boldsymbol{E}$, $\mu \rightarrow \epsilon$, and $\epsilon \rightarrow \mu$.

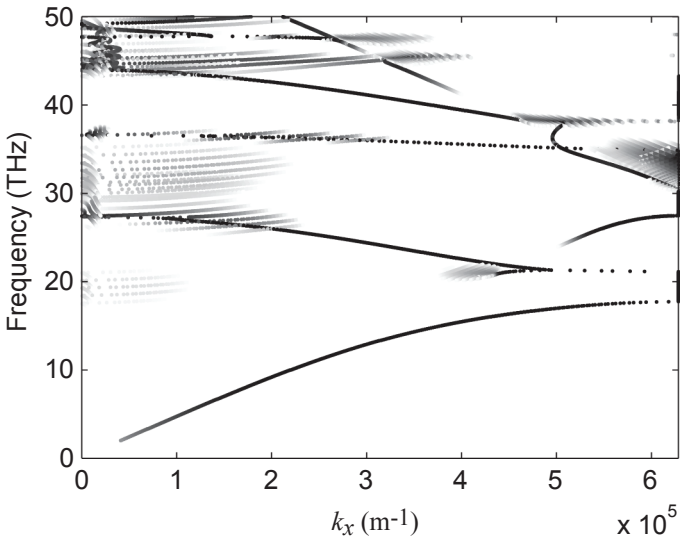

Figure B.3: Plot of frequency and real part of in-plane wavevector for TM solutions found using the FEM eigenvalue solver. Solution points are colored according to the metric S, with darker points having smaller S (more energy in vicinity of the slab).

BIBLIOGRAPHY

[1] J. D. Jackson. *Classical Electrodynamics*. Wiley, 3rd edition, August 1998.

[2] N. Tesla. System of transmission of electrical energy. US patent no 649,576, March 1900.

[3] A. Kurs, A. Karalis, R. Moffatt, J. D. Joannopoulos, Peter Fisher, and M. Soljačić. Wireless power transfer via strongly coupled magnetic resonances. *Science*, 317(5834):83–86, July 2007. PMID: 17556549. doi:10.1126/science.1143254.

[4] J. D. Heebl, E. M. Thomas, R. P. Penno, and A. Grbic. Comprehensive analysis and measurement of frequency-tuned and impedance-tuned wireless non-radiative power-transfer systems. *IEEE Antennas Propag. Mag.*, 56(5):131–148, October 2014. doi:10.1109/MAP.2014.6971924.

[5] S. B. Cohn. Direct-coupled-resonator filters. *Proc. IRE*, 45(2):187–196, 1957. doi:10.1109/JRPROC.1957.278389.

[6] B. Munk. *Frequency selective surfaces: theory and design*. John Wiley, New York, 2000.

[7] T. W. Ebbesen, H. J. Lezec, H. F. Ghaemi, T. Thio, and P. A. Wolff. Extraordinary optical transmission through sub-wavelength hole arrays. *Nature*, 391(6668):667–669, February 1998. doi:10.1038/35570.

[8] J. V. Coe, J. M. Heer, S. Teeters-Kennedy, H. Tian, and K. R. Rodriguez. Extraordinary transmission of metal films with arrays of subwavelength holes. *Annual Review of Physical Chemistry*, 59(1):179–202, 2008. PMID: 17988200. doi:10.1146/annurev.physchem.59.032607.093703.

[9] F. J. García-Vidal, L. Martín-Moreno, T. W. Ebbesen, and L. Kuipers. Light passing through subwavelength apertures. *Rev. Mod. Phys.*, 82(1):729–787, March 2010. doi:10.1103/RevModPhys.82.729.

[10] A. K. Azad, J. F. O'Hara, R. Singh, Hou-Tong Chen, and A. J. Taylor. A review of terahertz plasmonics in subwavelength holes on conducting films. *IEEE J. Selected Topics Quantum Electron.*, 19(1):8400416, January 2013. doi:10.1109/JSTQE.2012.2208181.

[11] J. A. Porto, F. J. García-Vidal, and J. B. Pendry. Transmission resonances on metallic gratings with very narrow slits. *Phys. Rev. Lett.*, 83(14):2845–2848, October 1999. doi:10.1103/PhysRevLett.83.2845.

[12] Y.-K. R. Wu, A. E. Hollowell, C. Zhang, and L. J. Guo. Angle-insensitive structural colours based on metallic nanocavities and coloured pixels beyond the diffraction limit. *Scientific Reports*, 3, February 2013. doi:10.1038/srep01194.

[13] J. Zhou and L. J. Guo. Transition from a spectrum filter to a polarizer in a metallic nano-slit array. *Scientific Reports*, 4, January 2014. doi:10.1038/srep03614.

[14] J. D. Joannopoulos, S. G. Johnson, J. N. Winn, and R. D. Meade. *Photonic Crystals: Molding the Flow of Light (Second Edition)*. Princeton University Press, October 2011. URL: http://press.princeton.edu/titles/8696.html.

[15] R. Magnusson and S. S. Wang. New principle for optical filters. *Appl. Phys. Lett.*, 61(9):1022–1024, August 1992. doi:doi:10.1063/1.107703.

[16] C. F. R. Mateus, M.C.Y. Huang, Y. Deng, A. R. Neureuther, and C.J. Chang-Hasnain. Ultrabroadband mirror using low-index cladded subwavelength grating. *IEEE Photonics Tech. Lett.*, 16(2):518–520, February 2004. doi:10.1109/LPT.2003.821258.

[17] W. Cai and V. Shalaev. *Optical Metamaterials - Fundamentals and Applications*. Springer Science, New York, NY, 2010. doi:10.1007/978-1-4419-1151-3.

[18] R. Merlin. Pinholes meet Fabry-Pérot: perfect and imperfect transmission of waves through small apertures. *Phys. Rev. X*, 2(3):031015, September 2012. doi:10.1103/PhysRevX.2.031015.

[19] S. M. Young, C. Pfeiffer, A. Grbic, and R. Merlin. Enhanced resonant transmission of electromagnetic radiation through a pair of subwavelength slits. *Appl. Phys. Lett.*, 103(4):041104, July 2013. doi:doi:10.1063/1.4816506.

[20] J. M. Foley, S. M. Young, and J. D. Phillips. Narrowband mid-infrared transmission filtering of a single layer dielectric grating. *Appl. Phys. Lett.*, 103(7):071107, August 2013. doi:doi:10.1063/1.4818735.

[21] J. M. Foley, S. M. Young, and J. D. Phillips. Symmetry-protected mode coupling near normal incidence for narrow-band transmission filtering in a dielectric grating. *Phys. Rev. B*, 89(16):165111, April 2014. doi:10.1103/PhysRevB.89.165111.

[22] R. Merlin and S. M. Young. Photonic crystals as topological high-Q resonators. *Opt. Express*, 22(15):18579–18587, July 2014. doi:10.1364/OE.22.018579.

[23] M. Born and E. Wolf. *Principles of optics: electromagnetic theory of propagation, interference and diffraction of light*. Cambridge University Press, Cambridge, New York, 7th expanded edition, 1999.

[24] A. Zangwill. *Modern Electrodynamics*. Cambridge University Press, 1st edition, 2012.

[25] H. A. Bethe. Theory of diffraction by small holes. *Phys. Rev.*, 66(7-8):163–182, October 1944. doi:10.1103/PhysRev.66.163.

[26] C. J. Bouwkamp. Diffraction theory. *Rep. Prog. in Phys.*, 17(1):35–100, January 1954. doi:10.1088/0034-4885/17/1/302.

[27] R. F. Harrington and D. Auckland. Electromagnetic transmission through narrow slots in thick conducting screens. *IEEE Trans. Antennas Propag.*, 28(5):616–622, September 1980. doi:10.1109/TAP.1980.1142382.

[28] Y. Leviatan, R. F. Harrington, and J. Mautz. Electromagnetic transmission through apertures in a cavity in a thick conductor. *IEEE Trans. Antennas Propag.*, 30(6):1153–1165, November 1982. doi:10.1109/TAP.1982.1142926.

[29] Y. Leviatan. Electromagnetic coupling between two half-space regions separated by two slot-perforated parallel conducting screens. *IEEE Trans. Microwave Theory Tech.*, 36(1):44–52, January 1988. doi:10.1109/22.3480.

[30] F. Yang and J. R. Sambles. Resonant transmission of microwaves through a narrow metallic slit. *Phys. Rev. Lett.*, 89(6):063901, July 2002. doi:10.1103/PhysRevLett.89.063901.

[31] E. Abbe. Beiträge zur theorie des mikroskops und der mikroskopischen wahrnehmung. *Arch. Mikrosk. Anat.*, 9(1):413–418, December 1873. doi:10.1007/BF02956173.

[32] C. J. Bouwkamp. Diffraction theory. *Philips Res. Rep.*, 5:321, 1950.

[33] A. Roberts. Electromagnetic theory of diffraction by a circular aperture in a thick, perfectly conducting screen. *J. Opt. Soc. Am. A*, 4(10):1970, October 1987. doi:10.1364/JOSAA.4.001970.

[34] G. B. Airy. On the phænomena of Newton's rings when formed between two transparent substances of different refractive powers. *Phil. Mag.*, 2(7):20–30, January 1833. doi:10.1080/14786443308647959.

[35] D.G. Deppe, D.L. Huffaker, Tchang-Hun Oh, H. Deng, and Q. Deng. Low-threshold vertical-cavity surface-emitting lasers based on oxide-confinement and high contrast distributed Bragg reflectors. *IEEE J. Selected Topics Quantum Electron.*, 3(3):893–904, June 1997. doi:10.1109/2944.640643.

[36] D. Sanvitto, A. Daraei, A. Tahraoui, M. Hopkinson, P. W. Fry, D. M. Whittaker, and M. S. Skolnick. Observation of ultrahigh quality factor in a semiconductor microcavity. *Applied Physics Letters*, 86(19):191109, May 2005. doi:10.1063/1.1925774.

[37] M. C. Y. Huang, Y. Zhou, and C. J. Chang-Hasnain. A surface-emitting laser incorporating a high-index-contrast subwavelength grating. *Nature Photonics*, 1(2):119–122, February 2007. doi:10.1038/nphoton.2006.80.

[38] E. Yablonovitch. Inhibited spontaneous emission in solid-state physics and electronics. *Phys. Rev. Lett.*, 58:2059, May 1987. doi:10.1103/PhysRevLett.58.2059.

[39] S. John. Strong localization of photons in certain disordered dielectric superlattices. *Phys. Rev. Lett.*, 58:2486, June 1987. doi:10.1103/PhysRevLett.58.2486.

[40] U. Fano. Effects of configuration interaction on intensities and phase shifts. *Phys. Rev.*, 124(6):1866–1878, December 1961. doi:10.1103/PhysRev.124.1866.

[41] R. W. Wood. On a remarkable case of uneven distribution of light in a diffraction grating spectrum. *Philos. Mag.*, 4(21):396–402, September 1902. doi:10.1080/14786440209462857.

[42] U. Fano. The theory of anomalous diffraction gratings and of quasi-stationary waves on metallic surfaces (Sommerfeld's waves). *J. Opt. Soc. Am.*, 31(3):213, March 1941. doi:10.1364/JOSA.31.000213.

[43] S. Fan and J. D. Joannopoulos. Analysis of guided resonances in photonic crystal slabs. *Phys. Rev. B*, 65(23):235112, 2002. doi:10.1103/PhysRevB.65.235112.

[44] F. Pardo, P. Bouchon, R. Haïdar, and J.-L. Pelouard. Light funneling mechanism explained by magnetoelectric interference. *Phys. Rev. Lett.*, 107(9):093902, 2011. doi:10.1103/PhysRevLett.107.093902.

[45] A. S. Barker and J. J. Hopfield. Coupled-optical-phonon-mode theory of the infrared dispersion in $BaTiO_3$, $SrTiO_3$, and $KTaO_3$. *Phys. Rev.*, 135(6A):A1732–A1737, September 1964. doi:10.1103/PhysRev.135.A1732.

[46] H. A. Haus. *Waves and fields in optoelectronics*. Prentice-Hall series in solid state physical electronics. Prentice-Hall, Englewood Cliffs, NJ, 1984.

[47] S. Fan, W. Suh, and J. D. Joannopoulos. Temporal coupled-mode theory for the Fano resonance in optical resonators. *J. Opt. Soc. Am. A*, 20(3):569–572, March 2003. doi:10.1364/JOSAA.20.000569.

[48] C. W. Hsu, B. Zhen, J. Lee, S-L. Chua, S. G. Johnson, J. D. Joannopoulos, and M. Soljačić. Observation of trapped light within the radiation continuum. *Nature*, 499(7457):188–191, July 2013. doi:10.1038/nature12289.

[49] R. Magnusson and S. S. Wang. Transmission bandpass guided-mode resonance filters. *Appl. Opt.*, 34(35):8106–8109, December 1995. doi:10.1364/AO.34.008106.

[50] S. Tibuleac and R. Magnusson. Narrow-linewidth bandpass filters with diffractive thin-film layers. *Opt. Lett.*, 26(9):584–586, May 2001. doi:10.1364/OL.26.000584.

[51] Y. Ding and R. Magnusson. Doubly resonant single-layer bandpass optical filters. *Opt. Lett.*, 29(10):1135–1137, 2004. doi:10.1364/OL.29.001135.

[52] R. Magnusson, D. Wawro, S. Zimmerman, Y. Ding, M. Shokooh-Saremi, K. J. Lee, D. Ussery, S. Kim, and S. H. Song. Leaky-mode resonance photonics: Technology for biosensors, optical components, MEMS, and plasmonics. *Proc. of SPIE*, 7604:76040M, February 2010. doi:10.1117/12.842436.

[53] S. Astilean, Ph. Lalanne, and M. Palamaru. Light transmission through metallic channels much smaller than the wavelength. *Opt. Commun.*, 175:265–273, March 2000. doi:10.1016/S0030-4018(00)00462-4.

[54] L. Martín-Moreno, F. J. García-Vidal, H. J. Lezec, K. M. Pellerin, T. Thio, J. B. Pendry, and T. W. Ebbesen. Theory of extraordinary optical transmission through subwavelength hole arrays. *Phys. Rev. Lett.*, 86(6):1114–1117, February 2001. doi:10.1103/PhysRevLett.86.1114.

[55] H. J. Lezec, A. Degiron, E. Devaux, R. A. Linke, L. Martín-Moreno, F. J. García-Vidal, and T. W. Ebbesen. Beaming light from a subwavelength aperture. *Science*, 297(5582):820–822, August 2002. doi:10.1126/science.1071895.

[56] F. J. García-Vidal, H. J. Lezec, T. W. Ebbesen, and L. Martín-Moreno. Multiple paths to enhance optical transmission through a single subwavelength slit. *Phys. Rev. Lett.*, 90(21):213901, May 2003. doi:10.1103/PhysRevLett.90.213901.

[57] R. F. Harrington. Resonant behavior of a small aperture backed by a conducting body. *IEEE Trans. Antennas Propag.*, 30(2):205–212, March 1982. doi:10.1109/TAP.1982.1142761.

[58] X. Shi, L. Hesselink, and R. L. Thornton. Ultrahigh light transmission through a C-shaped nanoaperture. *Opt. Lett.*, 28(15):1320–1322, August 2003. doi:10.1364/OL.28.001320.

[59] Y. S. Guo, J. Zhou, C. W. Lan, H. Y. Wu, and K. Bi. Mie-resonance-coupled total broadband transmission through a single subwavelength aperture. *Appl. Phys. Lett.*, 104(20):204103, May 2014. doi:10.1063/1.4879636.

[60] A. El-Haji, K.Y. Kabalan, and S. Khoury. Electromagnetic coupling between two half-space regions separated by multiple slot-perforated parallel conducting screens. *IEEE Trans. Electromagnetic Compatibility*, 37(1):105–109, February 1995. doi:10.1109/15.350249.

[61] M. Chuang and F. Chu. Comment on "electromagnetic coupling between two half-space regions separated by multiple slot-perforate parallel conducting screens". *IEEE Trans. Electromagnetic Compatibility*, 38(1):109–110, February 1996. doi:10.1109/15.485705.

[62] J. W. Lee and H. J. Eom. TM scattering from slits in thick parallel conducting screens. *IEEE Trans. Antenna Propag.*, 46(7):1117–1119, July 1998. doi:10.1109/8.704818.

[63] R. F. Harrington. *Time-Harmonic Electromagnetic Fields*. McGraw-Hill, 1961.

[64] R. F. Harrington and J. R. Mautz. A generalized network formulation for aperture problems. *IEEE Trans. Antennas Propag.*, 24(6):870–873, November 1976. doi:10.1109/TAP.1976.1141420.

[65] K. Y. Kabalan, R. F. Harrington, J. R. Mautz, and H. A. Auda. Characteristic modes for a slot in a conducting plane, TM case. *IEEE Trans. Antennas Propag.*, 35(3):331–335, March 1987. doi:10.1109/TAP.1987.1144083.

[66] C. Butler and D. Wilton. General analysis of narrow strips and slots. *IEEE Trans. Antennas Propag.*, 28(1):42–48, January 1980. doi:10.1109/TAP.1980.1142291.

[67] M. Abramowitz and I. A. Stegun. *Handbook of Mathematical Functions: with Formulas, Graphs, and Mathematical Tables*. U.S. Dept. of Commerce, National Bureau of Standards, Washington, D.C., 1972.

[68] M. Henstridge, J. Zhou, L. Jay Guo, and R. Merlin. A tunable narrowband terahertz filter based on resonances of a slotted waveguide structure. *To be published*, 2016.

[69] E. Maxwell. Conductivity of metallic surfaces at microwave frequencies. *J. of Appl. Phys.*, 18(7):629–638, July 1947. doi:doi:10.1063/1.1697818.

[70] A. G. Fox and T. Li. Resonant modes in a maser interferometer. *Bell Syst. Tech. J.*, 40(2):453–488, March 1961. URL: http://www3.alcatel-lucent.com/bstj/vol40-1961/articles/bstj40-2-453.pdf.

[71] S. S. Wang and R. Magnusson. Theory and applications of guided-mode resonance filters. *Appl. Opt.*, 32(14):2606, May 1993. doi:10.1364/AO.32.002606.

[72] S. G. Johnson, S. Fan, P. R. Villeneuve, J. D. Joannopoulos, and L. A. Kolodziejski. Guided modes in photonic crystal slabs. *Phys. Rev. B*, 60(8):5751–5758, August 1999. doi:10.1103/PhysRevB.60.5751.

[73] K. Sakoda. *Optical Properties of Photonic Crystals*. Number 80 in Springer Series in Optical Sciences. Springer-Verlag Berlin Heidelberg, 2001.

[74] P. Paddon and J. F. Young. Two-dimensional vector-coupled-mode theory for textured planar waveguides. *Phys. Rev. B*, 61(3):2090–2101, January 2000. doi:10.1103/PhysRevB.61.2090.

[75] T. Ochiai and K. Sakoda. Dispersion relation and optical transmittance of a hexagonal photonic crystal slab. *Phys. Rev. B*, 63(12):125107, March 2001. doi:10.1103/PhysRevB.63.125107.

[76] J. Lee, B. Zhen, S-L. Chua, W. Qiu, J. D. Joannopoulos, M. Soljačić, and O. Shapira. Observation and differentiation of unique high-Q optical resonances near zero wave vector in macroscopic photonic crystal slabs. *Phys. Rev. Lett.*, 109(6):067401, August 2012. doi:10.1103/PhysRevLett.109.067401.

[77] B. Zhen, S-L Chua, J. Lee, A. W. Rodriguez, X. Liang, S. G. Johnson, J. D. Joannopoulos, M. Soljačić, and O. Shapira. Enabling enhanced emission and low-threshold lasing of organic molecules using special Fano resonances of macroscopic photonic crystals. *Proc. Nat. Acad. Sci.*, 110(34):13711–13716, August 2013. doi:10.1073/pnas.1311866110.

[78] R. Magnusson, S.S. Wang, T.D. Black, and A. Sohn. Resonance properties of dielectric waveguide gratings: Theory and experiments at 4-18 GHz. *IEEE Trans. Antennas Propag.*, 42(4):567–569, April 1994. doi:10.1109/8.286232.

[79] Y. Kanamori, T. Kitani, and K. Hane. Guided-Mode resonant grating filter fabricated on Silicon-on-Insulator substrate. *Jpn. J. Appl. Phys.*, 45(3A):1883–1885, March 2006. doi:10.1143/JJAP.45.1883.

[80] J. Ye, N. Matsuyama, Y. Kanamori, and K. Hane. Silicon suspended resonant grating filters fabricated from a Silicon-on-Insulator wafer. *IEEE Photonics Tech. Lett.*, 20(10):851–853, May 2008. doi:10.1109/LPT.2008.921840.

[81] Y. Ding and R. Magnusson. Use of nondegenerate resonant leaky modes to fashion diverse optical spectra. *Opt. Express*, 12(9):1885, 2004. doi:10.1364/OPEX.12.001885.

[82] S. Boutami, B. Benbakir, X. Letartre, J. L. Leclercq, P. Regreny, and P. Viktorovitch. Ultimate vertical Fabry-Pérot cavity based on single-layer photonic crystal mirrors. *Opt. Express*, 15(19):12443–12449, September 2007. doi:10.1364/OE.15.012443.

[83] L. Pilozzi, D. Schiumarini, N. Tomassini, and A. D'Andrea. Giant reflection band and anomalous negative transmission in a resonant dielectric grating slab: Application to a planar cavity. *Phys. Rev. B*, 86(4):045301, July 2012. doi:10.1103/PhysRevB.86.045301.

[84] S. Tibuleac and R. Magnusson. Reflection and transmission guided-mode resonance filters. *J. Opt. Soc. Am. A*, 14(7):1617–1626, July 1997. doi:10.1364/JOSAA.14.001617.

[85] S. Tibuleac, P. P. Young, R. Magnusson, and T. R. Holzheimer. Experimental verification of waveguide-mode resonant transmission filters. *IEEE Microwave and Guided Wave Letters*, 9(1):19–21, 1999. doi:10.1109/75.752111.

[86] Y. Kanamori, M. Shimono, and K. Hane. Fabrication of transmission color filters using silicon subwavelength gratings on quartz substrates. *IEEE Photonics Tech. Lett.*, 18(20):2126–2128, October 2006. doi:10.1109/LPT.2006.883208.

[87] I. R. McKerracher, L. Fu, H. H. Tan, and C. Jagadish. Integration of bandpass guided-mode resonance filters with mid-wavelength infrared photodetectors. *J. Phys. D: Appl. Phys.*, 46(9):095104, March 2013. doi:10.1088/0022-3727/46/9/095104.

[88] M. S. Amin, J. W. Yoon, and R. Magnusson. Optical transmission filters with coexisting guided-mode resonance and Rayleigh anomaly. *Appl. Phys. Lett.*, 103(13):131106, September 2013. doi:10.1063/1.4823532.

[89] Justin M. Foley. *Subwavelength Dielectric Grating-based Broadband Reflectors and Narrowband Transmission Filters.* PhD thesis, University of Michigan, 2014. URL: http://deepblue.lib.umich.edu/handle/2027.42/107193.

[90] L. Chen, M. C. Huang, C. F. Mateus, Chang-Hasnain C. J., and Y. Suzuki. Fabrication and design of an integrable subwavelength ultrabroadband dielectric mirror. *Appl. Phys. Lett.*, 88(3):031102, January 2006. doi:10.1063/1.2164920.

[91] D. Fattal, J. Li, Z. Peng, M. Fiorentino, and R. G. Beausoleil. Flat dielectric grating reflectors with focusing abilities. *Nature Photonics*, 4(7):466–470, July 2010. doi:10.1038/nphoton.2010.116.

[92] F. Lu, F. G. Sedgwick, V. Karagodsky, C. Chase, and C. J. Chang-Hasnain. Planar high-numerical-aperture low-loss focusing reflectors and lenses using subwavelength high contrast gratings. *Opt. Express*, 18(12):12606, June 2010. doi:10.1364/OE.18.012606.

[93] N. W. Ashcroft and N. D. Mermin. *Solid state physics*. Number xxi, 826 p. Holt, Rinehart, and Winston, New York, 1976.

[94] M. Davanco, Y. Urzhumov, and G. Shvets. The complex Bloch bands of a 2D plasmonic crystal displaying isotropic negative refraction. *Opt. Express*, 15(15):9681–9691, July 2007. doi:10.1364/OE.15.009681.

[95] G. Parisi, P. Zilio, and F. Romanato. Complex Bloch-modes calculation of plasmonic crystal slabs by means of finite elements method. *Opt. Express*, 20(15):16690–16703, July 2012. doi:10.1364/OE.20.016690.

[96] E. D. Palik. *Handbook of Optical Constants of Solids*. Academic Press handbook series. Academic Press, Orlando, 1985.

[97] M. Vollmer and K-P. Möllmann. *Infrared Thermal Imaging: Fundamentals, Research and Applications*. Wiley-VCH, Weinheim, 2010.

[98] M. T. Eismann. *Hyperspectral Remote Sensing*. SPIE Press monograph. SPIE, Bellingham, Wash. USA, 2012. URL: http://app.knovel.com/web/toc.v/cid:kpHRS00001/viewerType:toc.

[99] D. K. Jacob, S. C. Dunn, and M. G. Moharam. Design considerations for narrowband dielectric resonant grating reflection filters of finite length. *J. Opt. Soc. Am. A*, 17(7):1241–1249, July 2000. doi:10.1364/JOSAA.17.001241.

[100] J. O. Grepstad, M. M. Greve, B. Holst, I-R. Johansen, O. Solgaard, and A. Sudbø. Finite-size limitations on quality factor of guided resonance modes in 2D photonic crystals. *Opt. Express*, 21(20):23640–23654, October 2013. doi:10.1364/OE.21.023640.

[101] J. M. Foley and J. D. Phillips. Normal incidence narrowband transmission filtering capabilities using symmetry-protected modes of a subwavelength, dielectric grating. *Opt. Lett.*, 40(11):2637, June 2015. doi:10.1364/OL.40.002637.

[102] Y. X. Yeng, W. R. Chan, V. Rinnerbauer, J. D. Joannopoulos, M. Soljačić, and I. Celanovic. Performance analysis of experimentally viable photonic crystal enhanced thermophotovoltaic systems. *Opt. Express*, 21(S6):A1035–A1051, November 2013. doi:10.1364/OE.21.0A1035.

[103] V. Rinnerbauer, Y. X. Yeng, W. R. Chan, J. J. Senkevich, J. D. Joannopoulos, M. Soljačić, and I. Celanovic. High-temperature stability and selective thermal emission of polycrystalline tantalum photonic crystals. *Opt. Express*, 21(9):11482–11491, May 2013. doi:10.1364/OE.21.011482.

[104] A. B. Matsko and V. S. Ilchencko. Optical resonators with whispering-gallery modes–part i: Basics. *IEEE J. Selected Topics in Quant. Electron.*, 12(1):3–14, February 2006. doi:10.1109/JSTQE.2005.862952.

[105] A. Lagendijk, B. van Tiggelen, and D. S. Wiersma. Fifty years of anderson localization. *Physics Today*, 62(8):24–29, August 2009. doi:10.1063/1.3206091.

[106] Y. Akahane, T. Asano, B. Song, and S. Noda. High-Q photonic nanocavity in a two-dimensional photonic crystal. *Nature*, 425(6961):944–947, October 2003. doi:10.1038/nature02063.

[107] T. Xu, S. Yang, S. V. Nair, and H. E. Ruda. Confined modes in finite-size photonic crystals. *Phys. Rev. B*, 72(4):045126, July 2005. doi:10.1103/PhysRevB.72.045126.

[108] R. Merlin. Raman scattering by surface-avoiding acoustic phonons in semi-infinite superlattices. *Philos. Mag. Part B*, 70(3):761–766, 1994. doi:10.1080/01418639408240248.

[109] M Trigo, T. A. Eckhause, M. Reason, R. S. Goldman, and R. Merlin. Observation of surface-avoiding waves: a new class of extended states in periodic media. *Phys. Rev. Lett.*, 97:124301, September 2006. doi:10.1103/PhysRevLett.97.124301.

[110] M. Charbonneau-Lefort, E. Istrate, M. Allard, J. Poon, and E. H. Sargent. Photonic crystal heterostructures: Waveguiding phenomena and methods of solution in an envelope function picture. *Phys. Rev. B*, 65(12):125318, March 2002. doi:10.1103/PhysRevB.65.125318.

[111] E. Istrate, A. A. Green, and E. H. Sargent. Behavior of light at photonic crystal interfaces. *Phys. Rev. B*, 71(19):195122, May 2005. doi:10.1103/PhysRevB.71.195122.

[112] E. Istrate and E. H. Sargent. Photonic crystal heterostructures and interfaces. *Rev. Mod. Phys.*, 78(2):455–481, May 2006. doi:10.1103/RevModPhys.78.455.

[113] H. Feshbach. On the perturbation of boundary conditions. *Phys. Rev.*, 65(11-12):307–318, June 1944. doi:10.1103/PhysRev.65.307.

[114] S. T. Thurman and G. M. Morris. Controlling the spectral response in guided-mode resonance filter design. *Appl. Opt.*, 42(16):3225–3233, June 2003. doi:10.1364/AO.42.003225.

[115] D. W. L. Sprung, H. Wu, and J. Martorell. Scattering by a finite periodic potential. *Am. J. Phys.*, 61(12):1118, 1993. doi:10.1119/1.17306.

[116] S. G. Johnson and J. D. Joannopoulos. Block-iterative frequency-domain methods for Maxwell's equations in a planewave basis. *Opt. Express*, 8(3):173–190, January 2001. doi:10.1364/OE.8.000173.

[117] S. M. Rudolph and A. Grbic. Super-resolution focusing using volumetric, broadband NRI media. *IEEE Trans. Antennas Propag.*, 56(9):2963–2969, September 2008. doi:10.1109/TAP.2008.928773.

[118] K. C. Huang, E. Lidorikis, X. Jiang, J. D. Joannopoulos, K. A. Nelson, P. Bienstman, and S. Fan. Nature of lossy Bloch states in polaritonic photonic crystals. *Phys. Rev. B*, 69(19):195111, May 2004. doi:10.1103/PhysRevB.69.195111.

[119] Y. Ding and R. Magnusson. Band gaps and leaky-wave effects in resonant photonic-crystal waveguides. *Opt. Expr.*, 15(2):680, January 2007. doi:10.1364/OE.15.000680.

[120] L. Essen and K. D. Froome. The refractive indices and dielectric constants of air and its principal constituents at 24,000 Mc/s. *Proc. Phys. Soc. B*, 64(10):862–875, October 1951. doi:10.1088/0370-1301/64/10/303.

[121] S. D. Lord. A new software tool for computing Earth's atmospheric transmission of near- and far-infrared radiation. *NASA Tech. Memo. 103957*, December 1992. URL: http://ntrs.nasa.gov/archive/nasa/casi.ntrs.nasa.gov/19930010877.pdf.

[122] K. Iga. Surface-emitting laser–its birth and generation of new optoelectronics field. *IEEE J. Sel. Top. Quant. Electron.*, 6(6):1201–1215, November 2000. doi:10.1109/2944.902168.

[123] M. Imada, S. Noda, A. Chutinan, T. Tokuda, M. Murata, and G. Sasaki. Coherent two-dimensional lasing action in surface-emitting laser with triangular-lattice photonic crystal structure. *Appl. Phys. Lett.*, 75(3):316–318, July 1999. doi:10.1063/1.124361.

[124] T. Xu, M. S. Wheeler, S. V. Nair, H. E. Ruda, M. Mojahedi, and J. S. Aitchison. Highly confined mode above the light line in a two-dimensional photonic crystal slab. *App. Phys. Lett.*, 93(24):241105, December 2008. doi:10.1063/1.3046124.

[125] P. Viktorovitch, B. Ben Bakir, S. Boutami, J. L. Leclercq, X. Letartre, P. Rojo-Romeo, C. Seassal, M. Zussy, L. Di Cioccio, and J.Marc Fedeli. 3D harnessing of light with 2.5D photonic crystals. *Laser & Photonics Reviews*, 4(3):401–413, 2010. doi:10.1002/lpor.200910009.

[126] W. Guo, A. Banerjee, P. Bhattacharya, and B. S. Ooi. InGaN/GaN disk-in-nanowire white light emitting diodes on (001) silicon. *Applied Physics Letters*, 98(19):193102, May 2011. doi:10.1063/1.3588201.

[127] L. Zhang, C.-H. Teng, T. A. Hill, L.-K. Lee, P.-C. Ku, and H. Deng. Single photon emission from site-controlled InGaN/GaN quantum dots. *App. Phys. Lett.*, 103(19):192114, November 2013. doi:10.1063/1.4830000.

[128] I. S. Gradshteyn and I. M. Ryzhik. *Table of Integrals, Series, and Products*. Elsevier Academic Press, 7 edition, 2007.

[129] Philippe Blanchard and Erwin Brüning. *Mathematical Methods in Physics*. Number 69 in Progress in Mathematical Physics. Springer International Publishing, Switzerland, 2nd edition edition, 2015. URL: http://link.springer.com.proxy.lib.umich.edu/book/10.1007%2F978-3-319-14045-2.

[130] R. D. Meade, A. M. Rappe, K. D. Brommer, J. D. Joannopoulos, and O. L. Alerhand. Accurate theoretical analysis of photonic band-gap materials. *Phys. Rev. B*, 48(11):8434–8437, September 1993. doi:10.1103/PhysRevB.48.8434.

[131] R. D. Meade, A. M. Rappe, K. D. Brommer, J. D. Joannopoulos, and O. L. Alherhand. Erratum: Accurate theoretical analysis of photonic band-gap materials [Phys. Rev. B 48, 8434 (1993)]. *Phys. Rev. B*, 55(23):15942–15942, June 1997. doi:10.1103/PhysRevB.55.15942.

[132] C. Fietz, Y. Urzhumov, and G. Shvets. Complex k band diagrams of 3D metamaterial/photonic crystals. *Opt. Express*, 19(20):19027–19041, September 2011. doi:10.1364/OE.19.019027.

[133] Z. S. Sacks, D. M. Kingsland, R. Lee, and J. Lee. A perfectly matched anisotropic absorber for use as an absorbing boundary condition. *IEEE Trans. Antennas Propag.*, 43(12):1460–1463, 1995. doi:10.1109/8.477075.